The University Of Sheffield.

Improvement of crankshaft oil hole quality through surface integrity studies

Peter Neal

A thesis submitted in partial fulfilment of the requirements for the degree of

Doctor of Engineering

The University of Sheffield

Faculty of Engineering

Department of Materials Science and Engineering

Submission Date

Autumn 2023

Acknowledgements

I would first like to thank everyone that I met during my research journey, you all helped me become a better researcher and a better person. I am sincerely grateful to my supervisory team, Prof. Russell Goodall, Dr. Pete Crawforth, and Dave Thompson for their continued guidance and personal support throughout the project. I hope to have the opportunity to collaborate again in the future. Thank you to Ricardo plc. for supporting this project; it was a privilege to work so closely with the automotive industry. I would also like to acknowledge the IDC Machining Science, both the staff members and my fellow students, for their support and encouragement over the years. The University of Sheffield and, in particular, the AMRC where I spent most of my time, has been a fantastic place to work. It has been a privilege to have the opportunity to work with various colleagues across numerous sites. The numerous machine operators and laboratory technicians, whose support and expertise were pivotal to the project, have my deepest gratitude.

Thank you to family and friends who have shown unwavering support through good times and bad, and to my parents Ray and Elaine for never doubting that I would make it to the finish line. Finally and most importantly, thank you to my caring and encouraging wife Imogen, it is not an easy task to support a PhD student and I would not have been able to get there without you.

Abstract

With increasingly strict emission regulations, engine manufacturers are being forced to increase peak cylinder pressures and reduce the size of crankshaft bearings to increase specific power output and efficiency. This places greater stress on the drilled crankshaft oil hole and increases the probability of fatigue failure. The goal of this research is to gain an improved understanding of the surface integrity of drilled holes, to enable manufacturers to select better machining strategies, and to have greater confidence when applying safety factors to designs. Current research surrounding the surface integrity of drilled oil holes is limited due to the infrequent use of drilled holes in heavily loaded components in other applications and the prior dominance of failure at other locations within the crankshaft. This thesis addresses this problem by applying state-of-the-art surface and materials analysis techniques to characterise the evolution of hole quality under varied drilling conditions. Through the exploitation of X-ray diffraction and electron backscatter diffraction techniques, large microstructural changes within hole surfaces are identified without significant sample preparation. Using this new analysis method, a new thermally activated microstructural recovery phenomenon is identified after burnishing that has significant implications for industrial implementation. Thermomechanical testing of 4140 Steel reveals a strong link between deformation temperature and microstructural evolution. In light of this, the surface integrity of holes drilled with two lubrication strategies with different cooling capacities is analysed. The results demonstrate that, although there may be sustainability benefits, the increased cutting temperatures associated with alternative lubrication strategies may restrict hole quality. The results of this project will allow engine manufacturers to design the crankshaft with a better understanding of the expected robustness and fatigue life of the oil hole and make more informed decisions when selecting drilling strategies for industrial manufacturing.

Contents

Nomenclature

HV	Vickers Hardness
C	Carbon
Si	Silicon
Mn	Manganese
P	Potassium
S	Sulfur
Cr	Chromium
Mo	Molybdenum
E	Youngs Modulus
UTS	Ultimate Tensile Strength
σ_{y}	Yield Stress
HB	Brinell Hardness
HRC	Rockwell Hardness
α	Rake Angle
F_{a},F_{r}, F_{d}, F_{c}	Machining forces in the axial, radial, direct feed and chip directions
t	Uncut chip thickness
σ	Stress
R_{a}, R_{z}, R_{v}	Mean, peak-to-valley height and valley depth roughness
S_{a}	Surface area roughness
d_{o}	Lattice spacing
V_{b}	Flank Wear
d_{i}	Indent diameter
V_{c}	Cutting Speed
f_{n}	Feed Rate
μ	Co-efficient of friction
XRD	X-Ray Diffraction
BN	Barkhausen Noise
EBSD	Electron Back Scatter Diffraction
FWHM	Full-Width at Half Maximum
FTTU	Fast Thermal Treatment Unit
b	Barreling Co-efficient
m	Friction Factor
$\bar{R}$	Average Radius
δR	Difference between maximum and minimum radius
δH	Change in height
ΣR	Sum of maximum and minimum radius
H_1	Deformed height

List of Figures

Chapter 1

Introduction

1.1 Motivation

The International Energy Agency (IEA) aims to reduce global average emissions by 50% by 2030 [1]. With this in mind, and with the goal of reaching net zero emissions by 2050, governments around the world have begun to tighten legislation surrounding vehicles. It is undisputed that stricter vehicle emissions standards have been a key part of curtailing CO_2 emissions and reducing air pollution in cities across the globe. Emissions legislation has led to drastic changes in the automotive landscape over recent years and instilled an unrelenting drive to produce greener and cleaner vehicles.

Manufacturers have chosen to tackle this drive toward stricter emissions targets with two strategies: exploration of battery-electric powertrain technologies, including pure battery-electric and hybrid-electric, and optimisation of the conventional fossil-fuel-based internal combustion engine (ICE). The combination of hybrid-electric and downsized ICE has allowed manufacturers to meet the tightening regulations in previous years, whilst retaining their ICE platforms. It is, however, clear that passenger vehicles have begun a rapid transition toward battery technologies, with BEVs (Battery-Electric Vehicles) representing a 16.9% share of new vehicles in the UK in May 2023 [2]. Some manufacturers have even chosen to end all development of internal combustion engine (ICE) technologies. But passenger vehicles do not represent the entire ICE market. On and off-highway heavy-duty engines make up a significant portion of the transport market. Off-highway includes construction vehicles, industrial generators, marine engines, etc. On-highway heavy duty includes vehicles such as trucks, buses, coaches, and tractors. On-highway heavy-duty vehicles are responsible for more than 25% of greenhouse gas emissions from road transport and more than 6% of total greenhouse gas emissions within the European Union. The transition to battery-electric technologies is more challenging for heavy-duty vehicles, which require long-range capacity and minimal downtime for charging. Additionally, heavy-duty vehicles that typically operate

continuously at consistent speeds do not benefit as greatly from regenerative braking and associated technologies.

In light of this, heavy-duty engine manufacturers have been forced to explore novel technologies for the purpose of curtailing conventional ICE tailpipe emissions. Enhanced technologies, revised fuels, and reduced vehicle/engine size can be considered effective techniques to improve engine fuel economy and reduce emissions. Extensive research is being conducted in the areas of alternative low-emission fuels and low-temperature combustion, but engine downsizing remains one of the most applicable ways for the automotive industry to meet this goal. Engine downsizing is a technology that increases engine thermal efficiency by forcing an engine to operate in more efficient high-load regimes, rather than operating in low-load regimes where pump losses significantly reduce engine thermal efficiencies. Incorporating a more compact displacement engine allows operators to benefit from a lower fuel consumption and reduced greenhouse gas emissions. Additionally, an elevated power density enhances the overall efficiency of these smaller engines. But this also places greater stress on the main loaded components of the ICE.

Higher power density and fewer cylinders place particularly high demands on the crankshaft. This is often accompanied by a reduction in the size of the crankshaft bearing to maximise the benefits to fuel efficiency and compactness. High combustion loads applied to smaller bearings generate greater stresses within the journal bearing and encourage increased contact between the running surfaces of the journal and plane engine bearings. This promotes a higher risk of failure in service due to inadequate material strength during overloading and excessive wear of contact surfaces leading to seizure. Fortunately, the yield strength and wear behaviour are well understood and can be predicted with computational modelling and experimental testing. These failure modes can be mitigated by employing an appropriate plane engine bearing design. Unfortunately, cyclic stresses even below the yield stress of the material can lead to the initiation and propagation of microcracks, which can result in fracture and failure of the component in service. This failure mode is termed fatigue. Fatigue is much harder to predict and has a multitude of contributing factors, ranging from the variables of the manufacturing process to the operating conditions of the engine. For this reason, past crankshafts have been engineered with generous safety factors and the occurrence of failures has typically been isolated to improper machining strategy and installation errors, rather than designs that struggled to meet fatigue strength requirements. However, the advancement in manufacturing technologies and processes, and the increasingly severe demands of these new engine designs, coupled with the desire to avoid overspecification and associated weight increases, has triggered a resurgence in research on fatigue.

Fatigue is a well-established body of research in the field of materials science. A solid understanding of the role of fatigue and design against failure is crucial when manufacturing

new components and has allowed engineers to mitigate the risks of fatigue failure [3]. The unfortunate difficulty with engine downsizing is the resulting decrease in bearing load capacity and the associated problems with fatigue life. Structural fatigue has become increasingly important due to the search for high-performance material solutions and increased manufacturing productivity. The crankshaft oil hole presents particular challenges due to the rare scenario of a drilled hole geometry that is subject to complex torsional and bending loads (Figure 1.1). In light of this, there is concern that as engines are downsized and specific power output increases, the safety factors of the components will continue to decrease. This research project was initiated from the belief that it is possible to alleviate this concern by better understanding the drilling process. The project utilised the combined resources of the Materials Science and Engineering Department and Advanced Manufacturing Research Centre of the University of Sheffield, and the project sponsor Ricardo plc.

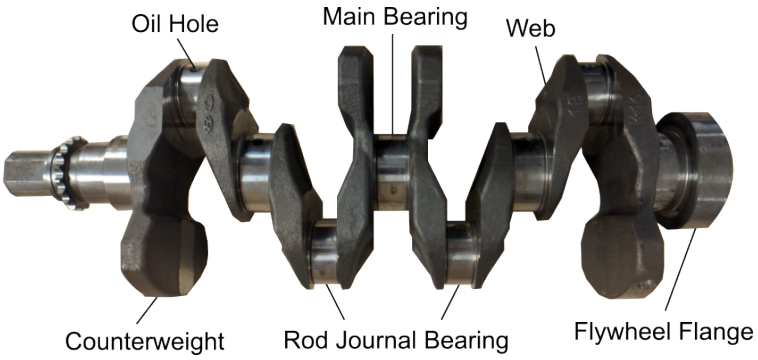

Figure 1.1: 4-cylinder inline crankshaft with the major parts labelled

1.2 Aim

The aim of this research project is to improve the understanding of the surface integrity of drilled crankshaft oil holes through the application of novel analysis methods to enable designers to apply safety factors to future designs with greater confidence and consideration for the manufacturing process.

1.3 Objectives

- Establish suitable methods for the characterisation of the shape of the drilled holes and how the process affects the surrounding material.
- Investigate surface enhancement procedures that could be implemented in the manufacturing process for such drilled holes.
- Develop a more complete understanding of the interaction between the drilling tool and the workpiece material and how this affects formation of the sub-surface microstructure.

- Identify the impact of potential changes to the drilling strategy that may be adopted in the coming years.

1.4 Thesis Structure

The experimental trials within the project align with the key main theme but are individually formulated to satisfy a combined industrial and research need.

Chapter 1 outlines the motivation behind the investigation of crankshaft oil-hole drilling and the establishment of a partnership between the University of Sheffield Advanced Manufacturing Research Centre (AMRC) and Ricardo plc. The aims and objectives of the research project are introduced.

Chapter 2 introduces the crankshaft and the materials and manufacturing methods commonly used in the production of automotive crankshafts. An appropriate steel alloy is selected for the research project, and particular attention is paid to the manufacturing steps that influence the generation of the oil hole. There is also a discussion surrounding potential failure mechanisms.

Chapter 3 reviews the available literature surrounding crankshaft fatigue failure, the influence of machining operations on the machined surface integrity, and the inspection methods that are currently available for the characterisation of machined surfaces. This chapter is laid out in this way to establish a link between the drilling operation and the expected lifetime performance of the crankshaft.

Chapter 4 defines the experimental methodologies used for the various tests found throughout the thesis without critical analysis of the decision behind their usage. This includes the method of operation of the equipment used.

Chapter 5 presents steps taken to optimise experimental procedures. Materials analysis is conducted on experimental and industrial drillings to build confidence that research-drilled hole specimens are comparable to industrial crankshaft oil holes. A tool wear study is conducted to determine a suitable cutting time limit for the efficient use of research tooling. Machining setup and monitoring methods are investigated. Surface and hardness inspection methods are also analysed to establish a best practice for characterising drilled holes.

Chapter 6 presents the results of an experimental machining trial investigating the effectiveness of the internal roller burnishing operation in enhancing surface integrity. Measured improvements are compared against the cycle time and reliability of the operation to determine whether it is a suitable choice for the enhancement of drilled oil holes. The chapter ends with a discussion surrounding the need for improved inspection methods for drilled oil hole surfaces.

Chapter 7 evaluates the use of X-Ray Diffraction and Barkhausen Noise inspection systems for the characterisation of machined surfaces. The use of a portable diffractometer and Barkhausen measurement equipment is tested for this novel purpose of characterising drilled holes and compared to Electron Back Scatter Diffraction analysis. Burnished and drilled hole specimens are analysed using these techniques and a potential temperature-driven deformation behaviour is proposed.

Chapter 8 presents the results of a thermo-mechanical materials testing study that was used to examine the behaviour of AISI 4140 steel during hot deformation. The temperature-dependent deformation behaviour of the alloy is discussed in relation to the previous chapter and potential implications for future machining operations.

Chapter 9 presents results from a Minimum Quantity Lubricant drilling trial investigating the influence of a sustainable lubricant strategy, operating at higher temperatures, on the microstructure and properties of the drilled near-surface. The chapter concludes with recommendations of research to be conducted by manufacturers prior to introducing sustainable lubricant strategies to their machining process.

Chapter 10 summarises the key outcomes and conclusions of this study.

Chapter 11 proposes future work to be conducted based on the findings of this thesis.

Chapter 2

Crankshaft Manufacturing and Materials Selection

2.1 The Crankshaft

The crankshaft is an extremely important mechanical component of the Internal Combustion Engine (ICE) that converts the reciprocating motion of the piston into rotational motion. This allows the energy that is extracted during combustion to be transferred to the wheels. The crankshaft consists of main journal bearings and crankpin/rod journal bearings that are connected by a large piece of metal known as the crank web. The crankshaft is coupled at the crankpin/rod bearing to the pistons by a connecting rod, which provides a mechanical linkage between the two components. During fuel combustion, large pressure waves are generated within the cylinder, which exert a vertical force on the piston face that is transferred through the connecting rod to the crankshaft. The crankshaft is subject to centrifugal forces as a result of its rotation and impact forces exerted by the connecting rod. These forces are experienced by the bearings for millions of engine cycles during the engine lifetime. As such, the bearings must be designed to withstand both the maximum load from the combustion event and the accumulated fatigue load. This requires the selection of a suitable design geometry, manufacturing route, and materials that exhibit the appropriate combination of properties for the application.

2.2 Manufacturing Route

Crankshafts are often classified by their method of construction. Here, crankshafts are divided into four categories: assembled, cast, billet-machined, and forged. In assembled crankshafts, the component parts are fabricated separately and shrink-fit or welded together. These are typically reserved for marine engines, where the crankshaft is too large to be built as a single piece. Cast crankshafts are manufactured by pouring molten metal, commonly

cast iron, into a mould that is set under cooling. This is a comparatively low-cost manufacturing route that still offers reasonable tensile strength and corrosion resistance. Billet manufacturing involves machining the crankshaft from a billet of steel. This is extremely expensive and time-consuming and, as such, is generally reserved for premium motorsport applications. Although the aforementioned methods have their respective benefits, the main production route for high-strength automotive crankshafts is forging.

The crankshaft processing route for forged steel crankshafts involves numerous time-consuming steps. The steel billet is first raised to an appropriate forging temperature, typically 900-1200ºC and then pressed into the desired geometry by repeatedly working the billet between a set of dies. Following this, the material is left to cool before being machined in numerous steps, including rough machining, grinding, and finish machining; during which oil hole drilling is completed. Crankshaft machining lines are extensive and throughput is key. Robotic systems transfer parts between numerous CNC machining centres to enable high-volume manufacturing (Figure 2.1).

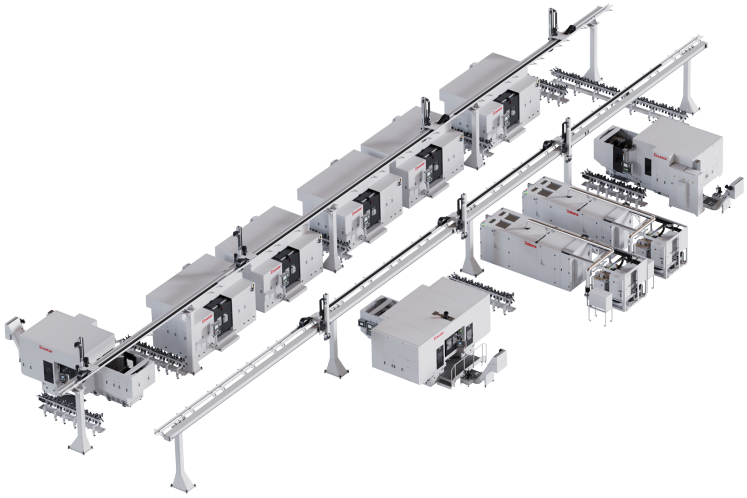

Figure 2.1: Example crankshaft machining line with numerous CNC machining centres [4]

Once the crankshaft is machined to the desired shape it is heat treated to produce the optimal combination of hardness, toughness and surface properties in what is typically a martensite-dominated microstructure. The oil hole drillings take place prior to heat treatment, whilst the crankshaft is in the as-forged condition, consisting of a predominantly ferritic-pearlitic microstructure. The hardness of the as-forged microstructure is approximately 300 HV, which is well within the capabilities of tungsten carbide drilling tooling. The crankshaft is always heat treated after machining because the large demands placed on the component during operation exceed the performance limits of the as-forged material. Heat treatment most commonly takes the form of nitriding or induction hardening. During nitriding, nitrogen is diffused into the surface by elevating the temperature of the part and holding it in contact with a nitrogenous material. The presence of nitrogen enhances wear resistance

and fatigue life. During induction hardening, a near-surface region of 4mm depth is raised above the austenite transition temperature (AC1) by electromagnetic induction coils and then rapidly cooled to form a martensitic-dominant microstructure. This causes a large increase in near-surface hardness as a result of the deformation resistance of the newly formed martensite. This provides benefits to wear and fatigue life and is an essential crankshaft processing step. Induction hardening provides the largest depth of modification and is often favoured by manufacturers. After heat treatment, the crankshaft is cleaned and inspected before being declared ready for use in service.

2.3 Materials Selection

The focus of this thesis is forged crankshafts, suitable for large-volume medium and heavy-duty applications. Materials used in crankshaft production require a good combination of hardness, toughness, wear resistance, and corrosion resistance. For this reason, steel alloys are commonly chosen for crankshaft manufacturing.

The material studied in this thesis is 42CrMo4/AISI 4140 steel, a medium-carbon alloy containing Manganese, Chromium and Molybdenum. 4140 steel is frequently used in crankshaft production due to its high hardenability, toughness and fatigue strength. Hardenability, described as the depth of the hardened martensitic layer that can be achieved by quenching, is of particular importance for crankshaft bearings since they undergo large bending, compression and torsional load cycles and high speed contact. Hardenability is heavily influenced by the austenite grain size, alloying elements, and carbon content. The large prior austenite grain size of 4140 steel inhibits the diffusion of carbides, since the carbon has further to travel to reach the grain boundary and the surface area of the grain boundary available for pearlite nucleation is reduced, increasing the propensity for martensite formation. This must be balanced against the increased propensity for quench-cracking of large grains by selecting an optimal austenising time, since grain size increases with time [5]. 4140 steel was chosen as the research material for this project since it offers a good combination of properties for high-volume medium and heavy duty crankshafts. The steel alloy was purchased as 115x115x250mm bars in the as-rolled condition to facilitate deep hole drilling. The chemical composition of the purchased material is presented in Table 2.1.

Table 2.1: Chemical Composition of AISI 4140 Steel

Element	**C**	**Si**	**Mn**	**P**	**S**	**Cr**	**Mo**
wt%	0.38-0.45	max 0.4	0.6-0.9	max 0.025	max 0.035	0.9-1.2	0.15-0.3

The mechanical properties of the material in the received condition are described in Table 2.2.

Table 2.2: Typical Mechanical Properties of AISI 4140 Steel

E (GPa)	UTS (MPa)	Oy (MPa)	Density (kg/m3)	Hardness (HB)
200	655	415	7800	300

2.4 Design Considerations

The main consideration for crankshaft designers is the peak cylinder pressure during fuel ignition. A larger peak cylinder pressure corresponds to a greater force on the piston which transmits through to the crankshaft journal bearing. Diesel engines operate at higher compression ratios than gasoline engines and therefore experience higher peak cylinder pressures. Heavy duty diesel engines, in particular, require large peak cylinder pressures to generate sufficient torque to move large loads. The forces exerted on the journal bearing include the force applied at the bearing by the connecting rod and inertial forces due to rotation of the crankshaft. The force on each bearing varies depending on which cylinder is firing at any given moment in time. This causes a cyclic force that can lead to fatigue failure. This type of failure is catastrophic and almost guaranteed to destroy the engine and surrounding components. Designing against fatigue failure of crankshafts is of great concern to automotive manufacturers.

In the past, the fillet where the bearing joins the web has been the most prevalent failure site due to the demands placed on the material in this location. In response to this, fillet enhancement methods such as deep-rolling have been optimised over the years to provide greater load-bearing capability. Modern downsized engines are required to provide the same power output through fewer cylinders with smaller volumes in order to increase efficiency. This is often accompanied by drivers operating at higher average engine speeds to extract power. This places greater forces on the crankshaft bearings and greatly increases inertial loads due to faster rotation. This combination requires modern crankshafts to be designed with much greater tolerance to high-cycle loading. But with the reduction in bearing sizes and increase in crankshaft loads, the oil hole has become an area of concern. The oil hole is required to transport oil from the main bearings to the rod journal bearings, and smaller rod journal bearings place the angular oil hole closer to the surface, with a sharper breakout. The oil hole is a weak point because of the stress concentration generated by the geometry and directing the drilling closer to the surface increases the load experienced during operation.

During service, the crankshaft is subject to high-magnitude cyclic loading as a result of the intake, compression, ignition and exhaust engine cycle. The effect of these combustion events is demonstrated in Figure 2.2, which shows the simulated change in load on the rod journal during the engine cycle. A stress analysis study was conducted in partnership with the sponsor company on a newly developed crankshaft. A linear elastic finite element model was used to determine material safety factors under an expected in-service load regime. The

lowest safety factor was identified at the oil hole exit of bearing three. For simplicity, the model used a global material model for the specified steel, without any consideration of local hardening effects. After machining, the bearing surfaces of the crankshaft are induction hardened to 52 HRC up to a depth of 4mm. The crankshaft in the study is modelled in an unhardened state. Maximum torsional stress is experienced at the outer edge of the bearing and this explains why in the unhardened model, safety factors were lowest at the hole breakout. However, there is a region below this 4mm hardened zone where torsional stresses remain relatively high, but there is no hardening effect. This region of the oil hole presents an increasing concern for designers, who must ensure that crankshafts are manufactured with adequate safety factors. This research project seeks to help this problem by improving the industrial drilling process.

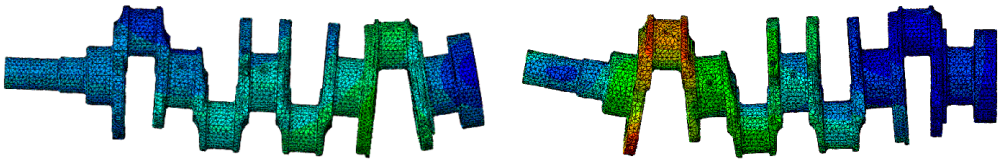

Figure 2.2: Variation in stress on the crankshaft rod journal bearings during operation, with red and blue denoting high and low stress respectively. Model generated by Ricardo Plc.

2.5 Machining

The quality of the machining process is a key contributor to the fatigue life of crankshafts. In crankshafts, fatigue failure can be encouraged by poorly prepared surfaces or can even initiate directly from machining-induced defects. The fatigue resistance of the drilled oil hole is likely to be heavily influenced by the surface and near-surface microstructure of the oil hole wall. The final state of this microstructure depends on the condition of the material prior to drilling and the deformation experienced by the hole wall during drilling. The pre-drilled microstructure is governed by prior manufacturing steps that are outside the bounds of this research and will therefore be excluded from this thesis. All research will be conducted on billets of as-rolled 4140 steel from the same manufacturing batch to maintain a consistent pre-drilled microstructure. The deformation experienced by the hole wall is governed by the tool-workpiece interaction. During drilling, the leading chisel-edge and cutting edges of the drill bit contact the material under high pressure and begin to generate shear in what is known as a chip (Figure 2.3). When the shear stress within the chip exceeds a pre-defined limit, the material breaks off and the process repeats. While this is happening, the outer diameter of the drill remains in permanent contact with the newly generated hole wall surface. This region of the tool is known as the margin and the contact here is specifically designed to stabilise the tool during cutting. However, this contact provides a secondary benefit by generating deformation at the hole wall surface.

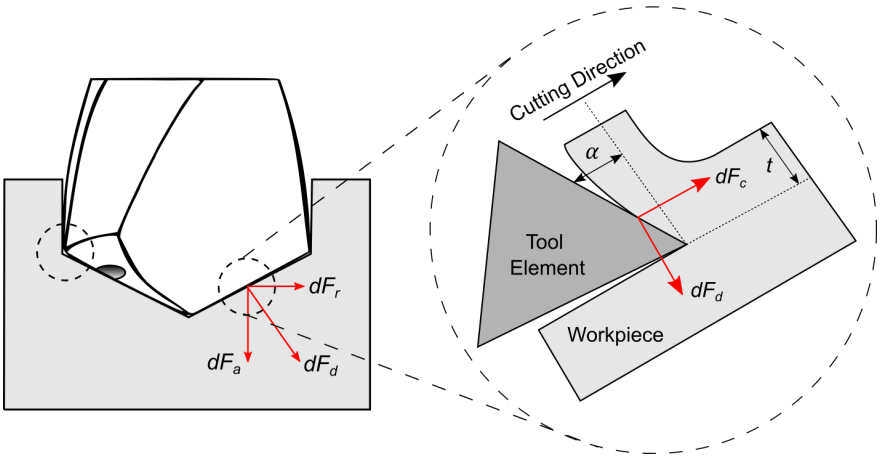

Figure 2.3: Schematic of a drill bit during operation, with the main cutting edge and margin highlighted, as well as the forces in the axial, radial, direct feed and chip directions

The interaction between the tool and the workpiece is governed primarily by the lubricant strategy, cutting speed and feed rate. The tool geometry and workpiece material properties are also key factors, but were kept constant for all machining trials in this project. The two common lubrication strategies for crankshaft drilling are emulsion coolant and Minimum Quantity Lubrication (MQL). Both lubricants are supplied in a through-tool configuration where fluid is fed through channels in the tooling and delivered directly to the tool tip. Emulsion coolant contains a mix of neat oil in the region of 8-12% and water. Minimum quantity lubrication is an aerosol mixture of high-pressure air and atomised droplets of oil. Although emulsion is the current dominant strategy, MQL is becoming increasingly popular due to the positive environmental benefits [6]. Cutting speed refers to the surface speed of the tool-workpiece contact and is measured in m/min. For a given tool diameter it is governed by the rotational speed of the spindle and may also be referred to in rpm. The cutting speed is specified at the outer diameter, but the relative velocity of the chip across the rake face decreases as you move toward the center of the tool. Feed rate describes the vertical travel of the tool in a single revolution, measured in mm/rev. The twist drills used in this study have two cutting edges, so the uncut chip thickness is equal to half the specified feed rate. As the cutting tool rotates it removes workpiece material in the form of chips and leaves behind a modified surface with several augmented surface integrity features (Figure 2.4).

Under loading the material initially deforms elastically, but when the yield stress is exceeded irreversible plastic deformation occurs. Plastic deformation can be accommodated atomically by either slip or twinning. During slip, layers of atoms slide over one another along crystallographic planes known as slip planes. Slip occurs once the shear stress across the slip

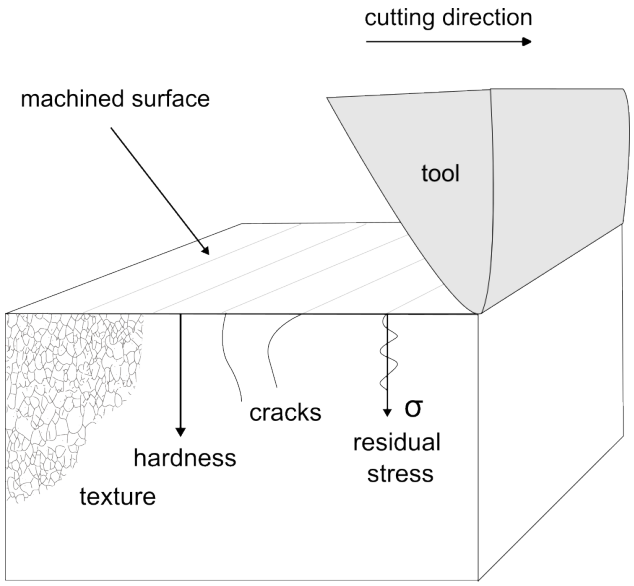

Figure 2.4: Surface integrity features generated by the machining process

plane in the direction of slip exceeds the critically resolved shear stress (CRSS). The CRSS is the minimum shear stress needed to initiate slip on a specific set of crystal planes and directions, also known as a slip system. According to the Von Mises criterion, five independent slip systems are required for a grain to slip. In materials science, slip is a deformation mechanism that occurs when layers of atoms in a crystalline material slide past each other under the application of an external force. Slip is an important mechanism in metallic plastic deformation and is crucial to many engineering applications. Twinning occurs when there is an insufficient quantity of slip systems for an arbitrary shape change and leads to a resultant crystal orientation where the atoms on one side of the twinning boundary are a mirror image of those on the other side. Twinning does not produce large quantities of deformation as a result of the small lattice strain, but can change the crystal orientation sufficiently to allow further slip to occur. A schematic of the crystal structures after slip and twinning is outlined in Figure 2.5.

Twinning takes places over a short time scale and reduced temperatures, high strain rates and low stacking fault energy increase the likelihood that twinning will be activated during deformation [7]. At low temperatures high-strength steels predominantly comprise of crystal structures exhibiting Body-Centered Cubic (BCC) arrangements. Certain steel alloys contain metastable austenite and showcase a Face-Centered Cubic (FCC) microstructure, but possess poorer material properties as a result [8]. 4140 steel consists of ferrite, pearlite and martensitic phases which all have a BCC arrangement. In comparison to steels with close-packed crystal structures such as FCC, in BCC steels the absence of stable stacking faults presents a barrier for the nucleation of twins and they exhibit poor twinning capability owing to their high stacking fault energy [9, 10]. Therefore, it is more likely that the material will deform through dislocation slip. As dislocations move, they can begin to pile

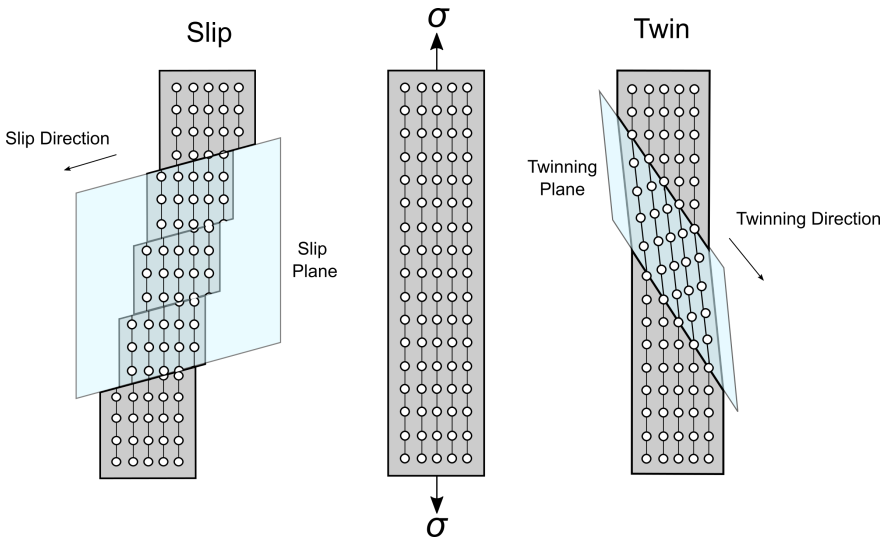

Figure 2.5: Mechanisms of dislocation slip and twinning under applied stress

up at grain boundaries. The concentration of these dislocations acts as a large barrier to crack propagation, thus increasing fatigue resistance. It is of interest to manufacturers to encourage this, and indeed surface enhancement processes, such as burnishing, are employed to promote fatigue resistance by increasing near-surface dislocation density. This is achieved by heavily deforming the near-surface region. However, excessively severe plastic deformation can induce phase changes in the deformed region through microstructural evolution to nano-crystalline martensite, which is detrimental to performance. It is important that the post-deformed microstructure of the hole wall is controlled to produce the desired material properties.

The quantity and magnitude of deformation in the machined surface and near-surface is a key determinant of the material properties and subsequent response to loading [11]. Manufacturers and researchers often seek to optimise surface integrity features with appropriate tool and parameter selection, but this is sometimes neglected in favour of minimising tool wear and maximising productivity. Productivity is a key performance metric for industrial operations and efficient cycle times are a necessity for high-volume manufacture. The competing priorities of these factors must be considered when designing the manufacturing process.

Chapter 3

Crankshaft fatigue failure mechanisms and contributing properties

This chapter reviews the current state of the literature in the fatigue of crankshafts and identifies potential key contributing properties to the fatigue strength of the component. The relationship between these surface integrity properties and fatigue performance is then discussed through analysis of past machining and related studies to ascertain the most important avenues of improvement. The literature review is purposefully structured in this way to provide a strong link between machining research and the performance of a manufactured crankshaft.

3.1 Crankshaft Fatigue

Crankshaft oil fatigue failure is driven by the repeated cycling loading of the component as it rotates over the course of millions of combustion events [12]. Under this cyclic load the material at the surface experiences alternating torsional, tension, and compression forces that encourage the formation and growth of cracks. These cracks can initiate from surface artifacts such as machining marks and can eventually propagate sufficiently far to drastically weaken the structural integrity of the material, leading to fractures that result in catastrophic failure in-service [13, 14]. The severity of the cyclic loading depends on several factors, including engine RPM, power output, and operating conditions. Higher engine speeds and greater power outputs, as well as more extreme operating conditions such as high temperatures or high loads, can increase the likelihood of fatigue failure. Proper design and materials selection are critical to preventing crankshaft oil hole failure through fatigue.

Various crankshaft fatigue failures have been analysed in the literature. Research surrounding fatigue failure originating at the oil hole is limited, perhaps due to the previous propensity for failure originating at the rod journal fillet. The fillet region where the bearing connects to the web is the most common failure point due to the large bending moment produced

at this location during combustion events [15, 16]. Errors in the machining operation have been responsible for multiple failures in the literature. A six-cylinder in-line diesel engine crankshaft that failed prematurely was analysed through fractography which revealed that over-grinding of a nitrided fillet region reduced fatigue strength in this critical location [17]. The same hypothesis was made for a similar diesel engine crankshaft failure [18]. Although the fillet region remains the most susceptible to fatigue failure, the application of fillet rolling procedures greatly enhances strength in this area [19]. With improving fillet enhancement technologies and decreasing bearing sizes, the oil hole is becoming increasingly subject to scrutiny.

Failure resulting from incorrect heat treatment was identified in a 1000cc Gasoline engine [20]. Whilst over-hardening was the root cause of the failure, the crack originated at the oil hole. Fatigue cracks can initiate from surface artifacts caused by machining operations and this is the most common cause of failure originating at the oil hole in the literature. Xu & Yu [14] aimed to understand the mechanism behind the premature failure of a cast iron diesel crankshaft which occured in-service after only 13,000 km of operation. Cracks were identified in three bearings, with full fracture of the bearing that carried the maximum load. All cracks originated from the oil holes. Inspection of the oil holes identified the presence of large dents approximately 3mm deep that were attributed to defects in the machining operation. It was proposed that these machining marks generated a stress concentration that ultimately led to fatigue failure. However, it is difficult to determine exactly where the failure originated because the fracture face is perpendicular to the hole axis. The failure location was also in the region directly beneath the induction hardened layer, which may have contained detrimental tensile residual stresses because of the hardening operation. Nevertheless, it is clear that the loads at the oil hole surface were sufficient to cause fatigue failure. Evidence of this type of failure can also be seen elsewhere, where failures are believed to have initiated from surface defects on the inner surface of the oil hole [21, 13].

Defects are an unfortunate consequence of high speed machining operations and the enclosed nature of the oil hole makes visual detection difficult. However by generating a hole wall with improved mechanical properties, these defects may remain stable under cyclic load. Studies from other fields have identified that surface defects that would otherwise lead to fatigue failure can be stabilised by the presence of plastic deformation and compressive stress fields [22].

3.2 Fatigue Factors

Studies show that in the absence of large material inclusions, fatigue cracks generally initiate at free surfaces due to the higher applied stresses and exposure to harsher conditions [23]. With this in mind, engineers continually pursue advances in tooling and machining strategies

to improve the quality of machined surfaces. Fatigue failure is complex and there are many factors that contribute to the fatigue life of machined components, including but not limited to residual stress, surface hardness, surface roughness, subsurface microstructure, and near-surface dislocation density. It is challenging to solely vary one factor through experimentation and isolate its contribution to fatigue performance. For instance, implementing a superfinishing process is likely to improve surface roughness, but may in turn enhance surface hardness and impart beneficial compressive residual stresses [24]. As such, there is at present no reliable model for predicting the fatigue life of machined components on the basis of the multitude of variables that exist in a machined surface. This may explain why standards for crankshaft fatigue life assessment rarely include factors for surface roughness, hardness and residual stress and yet research clearly suggests a strong link between these surface integrity parameters and the fatigue life of machined components [22, 24, 25, 26]. It is important to identify the relative improvement of fatigue performance due to these factors by synthesising machining and materials research and then designing the machining process to yield an improved combination of material properties. This section reviews the current literature surrounding the influence of the machining process on these variables and their subsequent contribution to fatigue failure.

3.2.1 Surface Finish

Since the majority of fatigue cracks initiate at free surfaces, it stands to reason that the quality of the surface would influence fatigue strength. Surface quality is generally quantified as the surface roughness, which describes the deviation of the surface topography from the ideal smooth form. It can be measured using various parameters the most common of which, R_{a} and R_{z} describe the average profile deviation from the mean and maximum profile peak to valley height respectively. For crankshaft oil holes, surface quality has implications for dirt entrapment, oil flow and customer perception of product quality but may also influence the fatigue strength of loaded parts. Excessive roughness presents a defect that creates localised stress concentrations on the surface [27].

Various studies have linked changes in surface finish parameters to the high-cycle fatigue strength of machined components. The cycles to failure of a 4140 Steel specimen under stepped-bar bending fatigue testing greatly reduced when R_{a} increased from 0.1μm to 1.6μm [28]. To achieve this change in surface roughness the tool nose radius and feed rate were modulated during the turning of the specimens. Nose radius and feed rate have been shown to also influence the generation of residual stresses within turned specimens, which is known to heavily impact fatigue life [23]. Gao [29] studied the influence of several surface finishing processes on fatigue life. The addition of electropolishing following grinding improved R_{z} but had a limited influence on fatigue life. The measured R_{z} after the initial grinding

step was already as low as 3μm and there was a small change in residual stress following electropolishing which may have altered the fatigue resistance.

Theory would suggest that applying a heat treatment such as annealing prior to fatigue testing would provide a reasonable estimation of the influence of surface finish. In the absence of a residual stresses differential between specimens following heat treatment, roughness contributed more significantly to the fatigue life of medium carbon steel [30]. Arola & Williams [**?**] found that high-cycle fatigue life of machined specimens of 4130 steel depended heavily on surface roughness and that fatigue strength decreased as roughness increased from 2-6μm. It is important to evaluate the results of these studies with respect to the expected surface finish of a drilled hole. Novovic et al. [31] identified a critical minimum roughness of around 2.0 μm, below which changes to roughness have a limited influence on fatigue life. Research has shown that with an appropriate machining strategy, a surface roughness below this limit can be achieved [32, 33, 34]. As well as excessive surface roughness, re-adhered chip material also presents a potential crack initiation site. Instances of re-adhered material can be reduced by limiting cutting temperatures, which can be achieved by selecting lower cutting speeds and superior lubricants [35]. Feed rate reduction may also help by reducing chip thickness and aiding efficient evacuation.

Discussion has focused around the fatigue benefits of a smoother surface finish but a high quality finish also reduces the likelihood that machining debris will mix with engine oil and cause severe damage to the system. Furthermore, a smooth surface improves part cleanliness because dirt and debris from manufacturing is less likely to become trapped. No negative effects of improving surface finish alone have been identified. Whilst a poorer surface finish does generate more frequent stress concentrations at the surface, fatigue life is more heavily influenced by the metallurgical properties of the surface and near-surface and these properties should be prioritised when selecting a machining strategy.

3.2.2 Mechanical and microstructural properties

Hardness is a measure of the resistance of a material to plastic deformation. The influence of hardness on fatigue life has been studied extensively for various materials and the relationship is specific to the material, processing and loading combination. Without the presence of phase changes, hardness is primarily driven by grain size [36]. The hardness properties of machined surfaces can be improved by encouraging grain refinement and enhanced dislocation density through concentrated plastic deformation. Kanemaru et al. [37] examined the effect of grain size on the fatigue strength of AISI 1141 steel through computational modelling and found that fine grained samples performed better than coarse grained samples under fatigue loading. The results agreed with further studies which have validated this relationship experimentally for other alloys [38, 36].

Liu et al. analysed the influence of machined surface and near-surface properties on the fatigue performance of steels [11]. Surface microhardness was found to decrease with cutting speed and interestingly, lower machining speeds were found to improve fatigue life, despite providing reduced compressive residual stresses in the near surface. Kuo [39] did not identify an appreciable change in surface hardness following drilling of Aluminium and Titanium with varying machining parameters. Although the shallowest hardness measurement was taken at 20μm from the surface, which may be beyond the heavily plastically deformed layer. At the highest feed rate and cutting speed the near-surface hardness was reduced to below the bulk hardness, although there was no notable change in microstructure.

Whilst hardness can be enhanced by grain refinement, increased material hardness can also be achieved through processing methods such as induction hardening. Induction hardening is a type of heat treatment process used to increase the hardness and wear resistance of metal components. During induction hardening, the surface of the metal is heated to above the austenite transition temperature, AC1 using an induction coil, then rapidly cooled above the critical cooling rate to form a hardened refined martensite layer. Compressive residual stress is also generated in the hardened zone. Yi et al. [40] investigated hardness and residual stress distributions in induction hardened steel discs of a similar alloy composition. The author combined the lattice spacing (d_o) results of X-Ray Diffraction (XRD) and Neutron Diffraction (ND) analysis at the surface and bulk material respectively due to the latter's greater penetration depth and accuracy in characterising the case material. The combined residual stress results are displayed in Figure 3.1, alongside an image of the corresponding hardened sample.

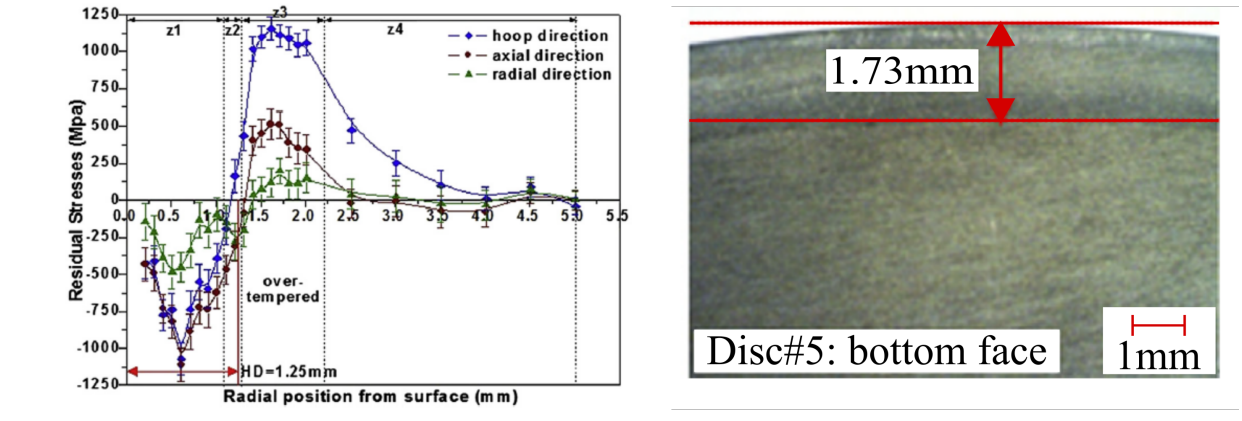

Figure 3.1: (a) Residual stress distribution in three directions, calculated based on XRD-measured d_o for the surface and ND-measured d_o for the core material (b) Heat treated surface with visible hardened layer [40]

The visible hardened layer is approximately 1.7mm thick. The near surface (1mm) was in a compressive stress state as expected, but there was an over-tempered region of tensile stress

beneath. An over-tempered region may be present in the oil hole following hardening, which emphasises the necessity to ensure a high quality drilled surface.

Whilst martensite formation is beneficial for wear resistance and yield strength, it is very brittle and can be detrimental to fatigue life if not formed under a controlled process. An example of uncontrolled martensite formation during machining is white-etching layer (WEL). WEL consists of ultra-fine martensite and is termed as such due to its intense white and featureless appearance under optical microscopy. WEL can be formed through two mechanisms: intense grain refinement due to severe plastic deformation, and thermally activated phase transformation [41]. Whilst a refined microstructure is generally beneficial for fatigue life due to the high density of dislocations, WEL is highly brittle, which is conducive to crack initiation and propagation [42]. As such, manufacturers are keen to prevent WEL formation during machining processes.

It is clear that induction hardening can provide material properties in selected high load regions, such as the crankshaft surface. Any influence of the grain structure prior to heating on hardenability is of interest to machinists, since knowledge of this could be leveraged to produce a better post-hardening oil hole. Increased austenite grain size is a key contributor to hardenability as the required diffusion distance of carbon and decreased grain boundary length for nucleation restricts the diffusion of carbides [43]. Characterisation of austenite is difficult, due to the relative instability of the phase in 4140 Steel at low temperatures. For this reason the mechanics of formation aren't particularly well understood. Shtansky [44] examined the kinetics of pearlite-to-austenite transformation for a chromium alloy. Nucleation appeared to occur preferentially at pearlite colony boundaries, but was also seen at the interface between ferrite and cementite within pearlite colonies. Interestingly, austenite that nucleated at the pearlite colony boundary did not cross further grain boundaries. and only expanded into adjacent grains. Defects play an important role in starting the transformation to austenite. Often, they serve as nucleation centers where the new phase can develop [45]. This suggests that heavily deformed pearlite with increased grain boundary and defect density, as found in the near-surface of drilled holes, may present more frequent nucleation sites. This may initially lead to an increased number of austenite grains within a given area. It is unknown whether following the continued application of heat these grains would expand and absorb one another. During induction hardening of 4140 Steel crankshafts, the near-surface is above the austenite transition temperature for approximately 10 seconds. Even if transformation were not to occur, increased pearlite boundary density may also provide benefits to fatigue stength. In ferritic-pearlitic microstructures cracks grow preferentially through ferrite and the presence of ferrite-pearlite boundaries significantly reduces the crack growth rate [46]. Fatigue crack resistance of ferritic-pearlitic microstructures has also been shown to improve when pearlite colonies were distributed rather than networked [47, 48]. Distributed colonies were proposed to generate a torturous crack path which limits crack propagation

and encourages crack closure. It is currently unknown whether this can be encouraged by the machining process.

It was clear when reviewing the literature that heat generated during cutting may be a significant contributor to the deformation mechanics and the resultant hole quality, including surface finish, hardness and residual stress profile. Ideally, any heat generated during cutting should be concentrated in the near-surface area. This serves to reduce the critically resolved shear stress in this region, encouraging deformation in near-surface grains, thus increasing near-surface dislocation density and introducing compressive residual stress and grain boundary strengthening where crack initiation sites are most likely to exist and stress concentration is highest. The trade-off is the creation of a tensile residual stress layer beneath, but fortunately loading in this region is lower. Unfortunately in reality heat generated during cutting transfers into sub-layers which are not mechanically deformed. Jacobus [49] examined near-surface residual stress in turning of annealed 4340 steel. The study identified a large tensile stress of 1000MPa in the near surface region followed by a region of compressive stress with increasing depth. Beyond 200μm, residual stress returned to zero for all tests, signifying no impact of machining below this point. As the author notes, the magnitude of the tensile stress is particularly important since the uniaxial yield strength of this material is approximately 400MPa at room temperature. The author theorises that the residual stress profile is due to the interaction between thermal and mechanical loads. Figure 3.2 outlines this mechanism in a cutting schematic.

Here the near surface layer, S is proposed to be a Heat-Affected Zone who's depth is influenced by the quantity of heat generated during cutting. This layer has a strain with an elastic, plastic and thermal component. Heat input causes workpiece thermal expansion on a microscopic level, termed here as thermal strain. However, as the part cools after machining, thermally induced strain is relieved. Therefore, the influence is solely the influence of heat on plastic deformation. But, heat may have a secondary impact on a significant impact on the ease with which material will deform and layers of material can accommodate strain. Varote [50] conducted microstructural analyses of drilled titanium alloy using dry and flood coolant strategies. Similarly to Jacobus [49], the plastically deformed layer was separated into a Heat-Affected Zone (HAZ) and Machining-Affected Zone (MAZ). The MAZ encompasses the whole area with a hardness higher than the bulk microstructure, whereas the HAZ is described as the very-near surface region where hardness varies due to thermal softening. A MAZ is present in dry and flood machining and increases in size with cutting speed due to increased plastic deformation. However, the HAZ is only present after dry machining due to the inefficient extraction of heat without coolant present. The HAZ also shows no variation with cutting speed, which is attributed to the low thermal conductivity of Titanium alloys. Whilst this may be true, the measurements were taken in 100μm depth increments, so it is possible that the depth resolution was too small to identify variation. If heat generated

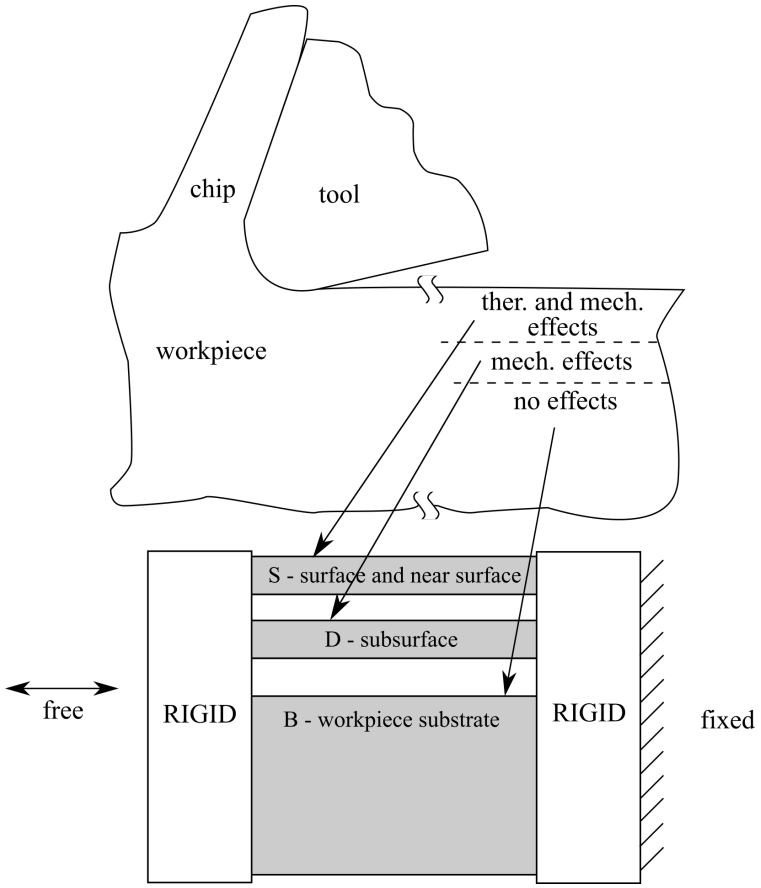

Figure 3.2: Schematic for the development of machining-induced residual stress, recreated from Jacobus [49]

during cutting is sufficient to raise the workpiece to above the austenite transition temperature, localised phase transformation may occur. This behaviour could be exhibited in 4140 Steel as it is capable of being heat treated to produce a Dual-Phase microstructure and is in fact often used in this condition if a balance of toughness and strength is required [51]. The partial austenisation and quenching of a near-surface machined layer could feasibly generate a dual-phase microstructure with a strained ferrite matrix, depending on temperature. This would provide an associated decrease in strength and experience weakening. Since a high martensite volume fraction is not necessary for this to occur, the depth of the transformed layer does not have to be large.

3.3 Summary

In summary, a clear link has been established between machining strategy, the fatigue strength of the machined surface and subsequent expected fatigue resistance of the crankshaft. The mechanisms of fatigue failure in crankshafts were identified by examining past studies of failed components, however examples within the research were limited due to industrial sensitivity. It was noted that machining issues were the root cause of a large number of

failures within the literature. A number of material properties were identified that exhibit a clear influence on the fatigue strength of machined components. Poor surface roughness encourages fatigue crack initiation by introducing stress concentrations, however the variation of roughness during crankshaft drilling is not expected to yield a significant change to fatigue strength. It was also apparent that reduced grain size inhibits fatigue crack propagation and beneficial microstructural evolution can be encouraged through selection of optimal machining parameters for the application. Better fatigue lives were generally achieved by promoting high near-surface hardness, a dislocation-dense microstructure and limiting large surface defects.

Chapter 4

Experimental Methodology

This chapter of the thesis outlines the setup and operation of the main experimental equipment used in this research project for the purpose of gaining an improved understanding of the crankshaft drilling process. This includes machine tools used to manufacture drilled specimens, custom test-cell equipment used to simulate the drilling process and the lab equipment used to analyse test specimens. The operation of any equipment that was specifically investigated and optimised in the research project will be outlined at the start of the respective chapters.

4.1 Machining

A number of machining trials were conducted during this research project. These machining trials took place on 3-axis machine tools located at the Advanced Manufacturing Research Centre and the Sandvik Coromant Solid Round Tools Development Centre in Sheffield, UK. CNC programs were manually programmed on machine. During machining, cutting forces were monitored with Kistler 9255B/C large plate bed dynamometers. Spindle runout was measured and recorded prior to each production run and if runout exceeded 20μm the tool was removed and remounted. An example setup within the machine is shown in Figure 4.1, although it must be noted that a dynamometer is not in use in this case.

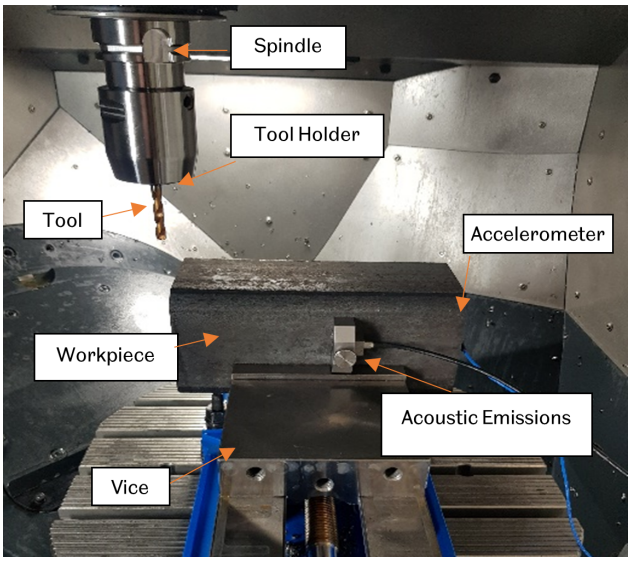

Figure 4.1: Inside DMU Evo40 Machining Centre [AMRC, Sheffield UK]

4.2 Thermo-Mechancial Compression Testing

As part of this thesis, a thermo-mechanical compression testing study is performed to understand the change in deformation behaviour of 4140 Steel with temperature and strain rate. A number of specimens were heated to various temperatures and deformed at high speed by a pair of compression platens under hydraulic pressure. During this study, all tests were conducted on a custom-built Thermo-mechanical Compression (TMC) testing machine at the University of Sheffield. The machine was specially produced by Servotest Ltd. with a custom control system that modulates deformation rate to maintain a constant True Strain rate. The machine specifications are shown in Table 4.1. The machine is controlled by six

Table 4.1: TMC Test Machine Specifications

Property	Machine Specification
Actuator Type	Servo Hydraulic
Maximum Strain	2
Maximum Strain Rate	100/s
Maximum Deformation Temperature	1200C
Maximum Load	500kN
Machine Stiffness	410kN/mm
Maximum FTTU Heating Temperature	1300°C
Quench Start Time	<0.5s
Cooling Methods	Air, mist, water
Temperature control and measurement	Embedded Sample Thermocouple

hydraulic pressure vessels used for high and low pressure functions. The high pressure vessels provide force to the main actuator which performs the deformation cycle. These vessels are mounted to the crosshead, a rigid beam that travels vertically up and down to allow the

correct tool height to be used for each specimen and tool type. The tools are produced from a high-strength M22 nickel-based super-alloy with a sufficient hot-hardness to withstand deformation of hard steel alloys. The bottom tool is fixed to the bottom post which sits above the load cell on the machine bed. The top tool is fitted to the upper post whose position is controlled by the main actuator. There is also a wedge that acts as a mechanical block on the crosshead, ensuring that the maximum strain specified by the operator is not exceeded. The wedge also protects the machine in the event of a hydraulic failure. These interior components involved in the deformation cycle are shown in Figure 4.2. The deformation takes place in the test furnace which is pre-heated to the desired deformation temperature.

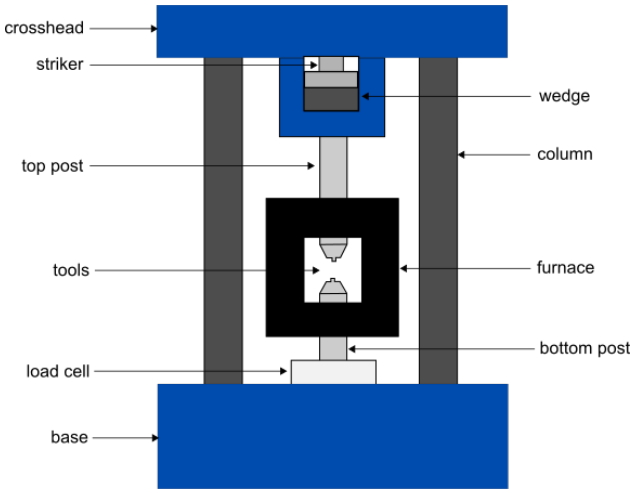

Figure 4.2: Labelled illustration of the interior components of the test machine

Machine input parameters include machine stiffness, specimen height and expected initial force. Machine Stiffness is re-calibrated when the machine is pre-heated to account for variations in stiffness due to temperature. The platens are brought into contact under a specified pre-load of 200kN and the resultant machine strain is recorded. The stiffness is then calculated by measuring the gradient of the linear portion of the load-displacement graph pictured in Figure 4.3. No direct strain measurements are taken during deformation. Since the test machine and platens are much stiffer than the compression specimen, strain can be inferred by the displacement of the platens below the input specimen height. The height of the sample was measured using digital callipers and taken as an average of three measurements at three locations on the surface to reduce error from misalignment of the caliper. Then, thermal expansion calculations are performed to obtain an expected initial sample height. This is the zero point from which the strain measurements are inferred. The initial force is the expected initial force required on the plates to begin deforming the material. An initial test run was used for each temperature to ensure that an appropriate expected initial force had been selected. If the expected initial force was overestimated, the initial strain rate would have exceeded the target value and vice versa. The test run log was analysed to verify if the target strain rate measured by the platen displacement had

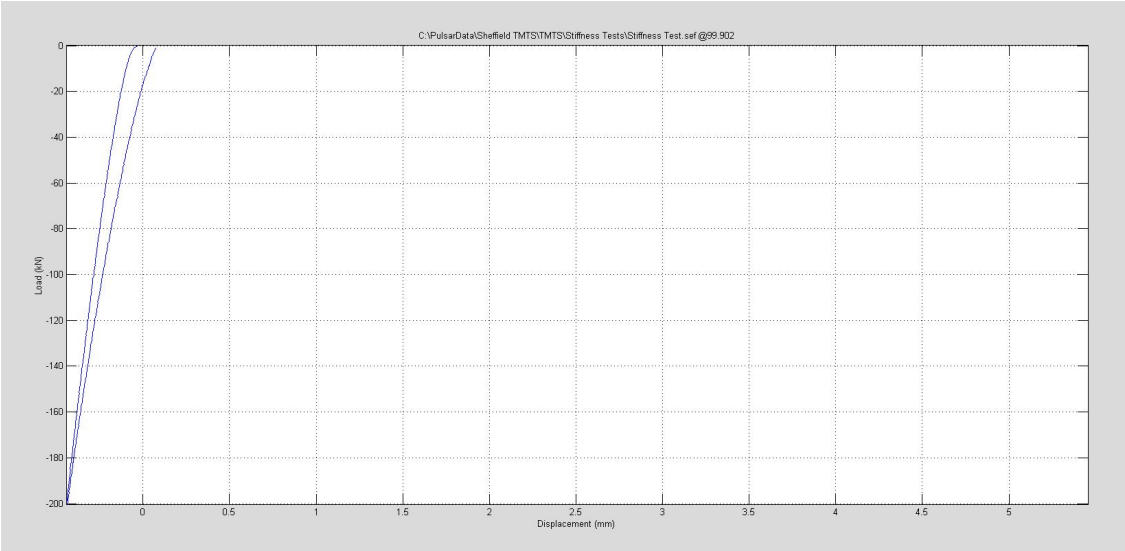

Figure 4.3: TMC stiffness calibration load displacement graph

been reached. A small error in initial force could be compensated for by the control system whilst the deformation is still in the initial elastic region. Although this may misrepresent the elastic properties for a given strain rate, provided the true strain rate stabilises before the onset of plastic deformation, it is unlikely to induce a change in plastic flow behaviour and post-deformation microstructure, which is the focus of this study.

Figure 4.4 shows the position of the sample, held by robotic arms prior to the start of a test. The sample is preheated inside the labelled Fast Thermal Treatment Unit (FTTU), which utilises two induction coils above and below to heat the sample at the specified rate. The software uses a thermocouple inserted into the sample to modulate the heating rate. The FTTU also provides cooling of the sample after deformation via forced air, water, or mist depending on the desired cooling rate. Displacement, load, temperature, strain and strain

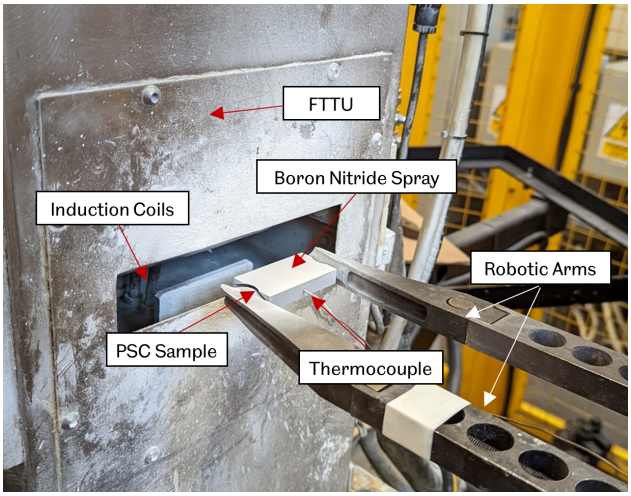

Figure 4.4: TMC Machine Setup before entry into the furnace and compression chamber

rate are captured throughout all stages of the experiment. The date sampling frequency

is maximised during deformation and minimised at all other times. This data can then be exported alongside the test specification for post-processing. All test data was analysed in MATLAB using programs generated by the author.

4.3 Surface Profilometry

Surface profilometry tools were used to assess the topography of various machined surfaces. This included contact profilometry and optical imaging systems. Basic surface profilometry was performed using a Mitutoyo SJ-120 profilometer. During operation, a diamond-tipped probe is traversed across the sample, and minute deflections caused by the surface topography are captured. Only single-line scans can be performed, and due to the drilled hole geometry, the accuracy of the measurement is heavily dependent on the orientation of the profilometer. This system was only suitable for use as an indication of the evolution of surface finish during machining trials. More extensive surface characterisation was carried out using an Alicona InfiniteFocus SL 3D measuring instrument (Figure 4.5). During operation, the lens focuses

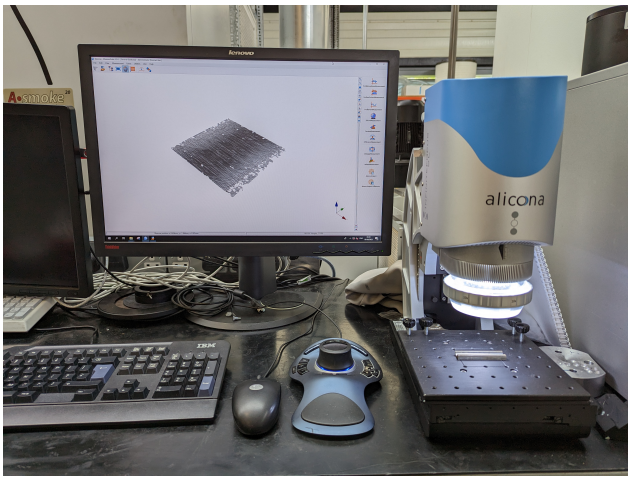

Figure 4.5: Alicona InfiniteFocus SL optical profile measurement system

on and images multiple planes at successive heights before stitching the images together to form a final surface topography. The system can achieve a vertical resolution of up to 10nm. The specimen is first placed on the measurement bed beneath the high-resolution lens. The bed can then be moved to align the area of interest on the specimen with the centre of the lens with the aid of the real-time camera display and laser marker. The upper and lower measurement limits are then set manually by bringing the specimen surface in and out of focus. The step height for each image is set by the operator, where a trade-off must be made between resolution and measurement time. Once the 3D image had been captured, the hole curvature was removed by applying a Robust Gaussian filter for arbitrary surfaces (ISO 16610-71). The impact of applying form removal is shown in Figure 4.6, where the colour represents the relative height of the measured point on the surface.

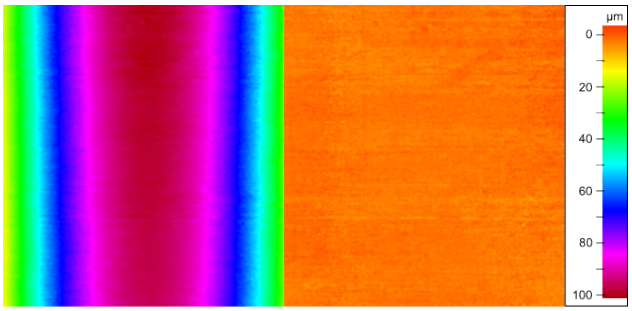

Figure 4.6: A heatmap of the surface before (left) and after (right) the application of form removal, superimposed over the surface topography

4.4 Sample Preparation

This section outlines the method of preparation of small samples for metallurgical analysis. Large samples were initially extracted from large workpieces or components using either a reciprocating bandsaw or wire EDM machine, depending on the geometry and condition of the material. The setup for wire EDM sectioning of a crankshaft bearing is shown in Figure 4.7.

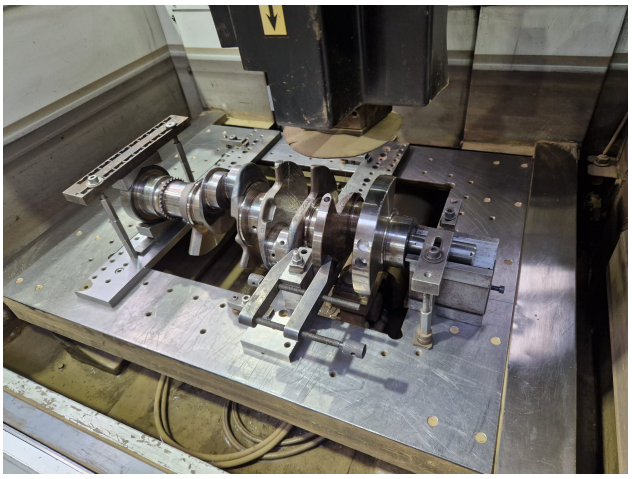

Figure 4.7: An industrial crankshaft fixtured to a wire EDM machine bed prior to sectioning

To induce minimal thermal damage in the recast layer surrounding the cut, a thin wire must be operated at a low power, commonly termed a skim cut. However, as a skim cut can only penetrate material up to 30mm thick, specimens containing deep-drilled holes must first be separated into smaller sections. Drilling holes at a greater distance apart makes this process more time-consuming, which in turn increases cost. The parameters when conducting wire EDM sectioning are outlined in Table 4.2

Once large samples had been extracted, they were taken to the materials laboratory to precisely section the region of interest. During precision sectioning, thermal and mechanical damage may have been caused by the cutting process. To reduce this, progressively less aggressive cutting speeds and finer cutting discs were used to minimise heat transfer into the

Table 4.2: Cutting parameters used in the wire EDM cutting process

Parameter	Value
Voltage (V)	16
Feed Rate (mm/min)	1
Wire Material	Brass
Wire Diameter (mm)	0.3
Distance between wire guide and top of work piece (mm)	0.2

sectioned material. Although it would be beneficial to investigate the effects of sectioning on the microstructure of the material, the grinding and polishing procedure required to prepare a sample for imaging removes the near-surface layers, which are most likely to have suffered damage. Therefore, instances of thermal or mechanical damage would be difficult to characterise using optical microscopy. For the analyses conducted in this thesis, it is assumed that the sectioned holes are representative of the machined state. A list of the equipment used in sample preparation is described in Table 4.3.

Table 4.3: Equipment and consumables used for the preparation of small samples

Stage	**Equipment**
Coarse Sectioning	Buehler Abrasimet
Fine Sectioning	Struers Secotom-20, Buehler Isomet 5000
Hot Mounting	Buehler Simplimet
Grinding	Automet, SiC Discs P400, P800, P1200, P2500
Polishing	Automet, MD Chem Polishing Pads

All samples were initially sectioned using a manually operated Buehler Abrasimet and Met-Prep abrasive cut-off discs. Silicon carbide cut-off discs were used according to the manufacturer's recommendations. The samples were then reduced to final size with a Struers Secotom-20 or Buehler Isomet, depending on the final sample size and proximity of the area of interest to the cut location. The Buehler Isomet is capable of operating at much lower material removal rates and speeds, reducing the amount of heat generated and the size of the thermally damaged layer. However, it requires smaller samples and has a greatly increased cutting time.

Once samples had been sectioned to an appropriately small size, they were mounted in conductive Bakelite under high pressure in a Buehler SimpliMet Hot Mounting Press. Conductive Bakelite was chosen as the mounting medium since it is compatible with Scanning Electron Microscopy (SEM). Samples were extracted from the mounting press in a 30mm diameter puck. Following mounting, samples were ground and polished with a Buehler Automet automated polishing machine. The machine applies a set force to the center of specimens mounted face down in a rotating specimen holder in contact with a rotating bed.

This ensures even application and reduces temperature build-up. During grinding, progressively finer grit SiC discs (P400,P800,P1200,P2500) were used at an applied force of 27N to produce a flat surface free of deposits and defects. Between grinding steps the surface was inspected with light microscropy to ensure all damage from prior grinding steps had been removed. Finally, samples were polished to a mirror finish in two stages using MD Chem polishing pads sprayed with 3um diamond solution and colloidal silica. A separate pad was used for each solution to prevent cross-contamination and samples were rinsed for one minute with water to remove leftover solution.

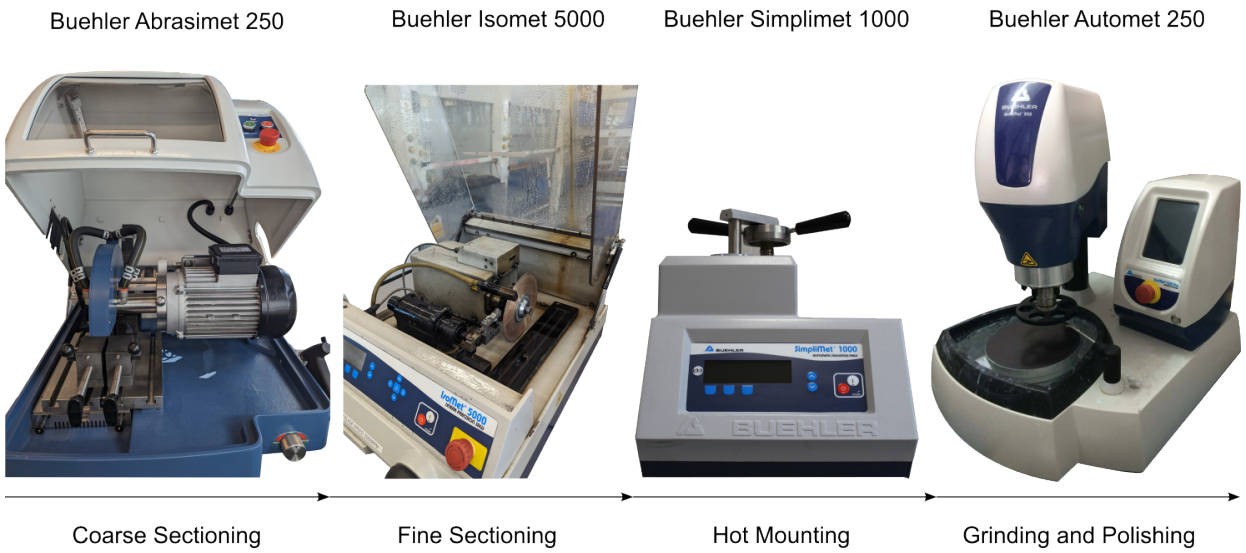

Figure 4.8: Process flow for the preparation of small specimens for materials analysis

In order for sample microstructures to be visible under microscopy, they had to be chemically etched. 2% Nital reagent was chosen based on the recommendations of [52] and prior industrial experience. 2% Nital was produced by mixing 2ml HNO_3 with 98ml methylated spirit. Polished specimens were dipped in the reagent in 10s intervals between which the sample was visually inspected with a bench-top microscope. As soon as the sample was lifted out of the reagent it was dipped in water to prevent further etching and Isopropyl alcohol for cleaning and drying. Once the grain boundaries became visible, the etching process was stopped as excessive etching can lead to marring of the surface and a reduction in grain visibility. All optical micrographs contained in this thesis were taken from specimens that had been etched in this way.

4.5 Material Analysis

This section higlights the lab equipment and analysis methods used to characterise the metallurgy of test specimens.

4.5.1 Hardness

Two hardness testing machines were used during the course of this research project to extract hardness profiles of processed specimens: the Durascan Microhardness indenter and the NanoTestVantage Nanohardness tester. The Durascan was used for measurements that required low spatial resolution since the smallest resolvable indent size was around 30μm. Conversely, the nanohardness tester was used when a large change in microstructure was expected at the micron scale. Microhardness and Nanohardness tests were conducted as per ASTM E384-22 and ASTM E-2546 respectively. Both systems are shown in Figure 4.9.

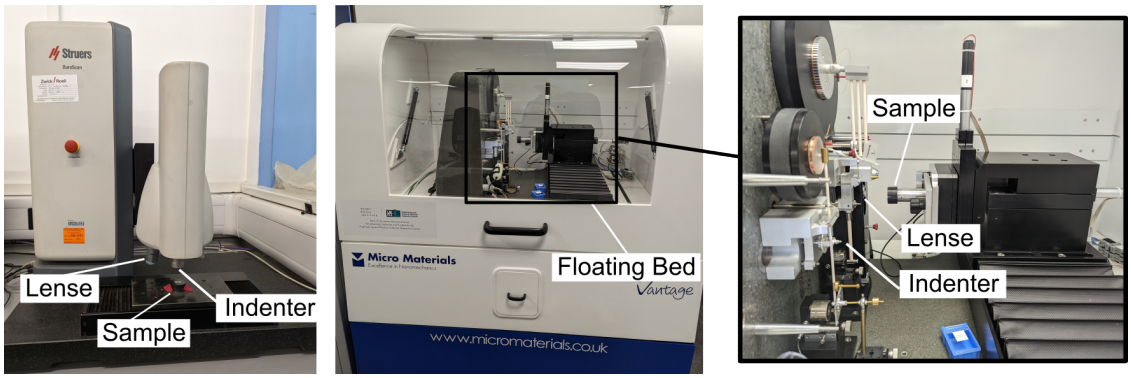

Figure 4.9: Durascan G5 and Micromaterials Nanotest Vantage hardness testing equipment

The Durascan G5 is a microhardness test machine that lowers a diamond-tip indenter into a specimen under loads of between 0.01kgf and 10kgf to assess the material properties. During operation the specimens were fixed to the test bed using putty on either side of the specimen, but no putty was placed underneath the specimen to prevent compliance issues. The specimen height was calibrated for each specimen through a touch-test, where the indenter was lowered slowly until a force was registered at the tip. The indent locations were then manually assigned in a test grid before the test was started. A dwell time of 15s was used to capture deformation creep. Indent size was measured immediately after each indent by the camera rather than at the end to reduce error due to specimen movement. The indent edges were identified through an image-processing algorithm. All images were also inspected post-test to verify that the software had accurately identified the indent edges.

The Nanotest Vantage Nanoindenter operates similarly to the Durascan but is designed to operate at loads as low as 10μN. At low loads, hardness tests are highly prone to errors induced by vibration transmitted through the floor, sample flatness and sample cleanliness. To reduce vibration error, the indenter system is mounted to a floating bed that is able to move independently of the machine base. To ensure sample flatness and prevent oil film error, strict preparation steps were adhered to as per Section 4.4 and samples were cleaned with Isopropyl alcohol prior to testing. The samples were mounted to the mounting stub

with super-glue and aligned to the indenter using the in-built optical microscope lens. The test grid was then chosen based on the required hardness profile and manually assigned in the software. During the test a dwell period of 15s was used to capture deformation creep and allow thermal drift compensation to be applied. The indentation data was then post-processed and a power law curve fit was used to extract material properties based on the Berkchov indenter geometry and distance of travel. The indents produced by low loads were only visible under high-magnification optical microscopy, therefore it was important to ensure the sample was flat, to reduce the need for repeats and excessive experimental runtime.

4.5.2 Optical Microscopy

Light Optical Microscopy (LOM) was conducted on polished and etched specimens to assess the material microstructure. All LOM within this research project was completed with a Nikon LV150N bench top microscope. A wide range of magnifications were available through 5, 10, 20, 50 and 100x optical zoom lens' and digital zoom within the imaging software.

Chapter 5

Experimental Validation and Optimisation

There were a number of important optimisation steps to be taken with various types of experimental analysis to be used elsewhere in the work, where information was not obtainable from existing literature or in-house knowledge. Outlined in this chapter are several studies which were conducted to develop optimum parameters and procedures. First, appropriate sample extraction locations are identified and steps are taken to validate the material properties of the research material and build confidence that experimentally-drilled holes are comparable to industrial drillings. Methods of processing machining data to verify the repeatability of research drillings are then conceived. Following this, a tool wear study is conducted to establish a reasonable cutting time limit for the efficient use of tooling. Finally, current standard specimen inspection methods for surface roughness and hardness are evaluated and improvements are proposed to increase measurement accuracy and enable superior characterisation of the machine-affected layer.

5.1 Industrial applicability

In this section, the results of the analysis of a drilled crankshaft oil hole specimen are presented, alongside investigations into the comparability of research drilled samples to industrial components. This work was completed to establish a method for comparing samples that evaluates the machined surface and excludes further material processing steps.

For experimental research to be comparable to industry, the material, tooling, machining cycle, and pre and post-processing steps of the experimental parts must match the industrial components as closely as possible. It is simple to select identical tooling, material specification and operate the same machining cycle, but it is much more difficult to emulate the pre and post-processing procedures such as forging and induction hardening. It is not feasible to obtain a production blank to conduct drilling operations on due to the large costs

involved. Besides, the object of this study is to evaluate the drilling process, not the entire manufacturing cycle. End-of-life components that have been taken out of service offer a useful alternative to allow comparison with research machined samples to understand the bulk microstructure and ensure that research drillings are representative of industrial drillings. Crankshaft samples taken from an operational engine were provided by the industrial sponsor for analysis, but first, appropriate sample locations that had not been influenced by pre and post-processing operations had to be established. Following machining, crankshafts are subjected to heat treatment and hardening procedures to establish an optimal combination of hardness, strength and ductility. For instance, post-machining, the bearing surfaces of the crankshaft samples provided were induction hardened to 52 HRC and a depth of 4mm from the hole breakout. Heat treatment is targeted at specific areas with the intention of leaving the core microstructure unaffected, but neighboring regions can experience changes to material properties.

Directly below an induction hardened layer, a heat-affected transition zone where hardness has been reduced relative to the as-machined state is generated. This occurs due to partial heating that is insufficient to induce the austenite transformation necessary for hardening, but sufficient to temper the microstructure and introduce grain recovery. If samples were to be taken from this location, they would not be representative of the as-machined state. Since the objective of this study was to investigate the influence of machining, rather than induction hardening, the size of this region had to be established before comparisons could be drawn between industrial and research drillings.

Hardness measurements were conducted on a cross-sectional crankshaft sample in 0.5mm increments from the top of the hardened region to a depth of 6mm. The location of the indentation array is superimposed over the etched specimen in Figure 5.1 with the hardened region clearly visible. As asymmetric hardening was found, shown here by a different hardened layer width on either side of the hole, measurements were taken on the side of the greatest layer depth. Hardness remained around the target value until approximately 3mm when it began to fall. After 4mm the hardness dipped to below the as-forged value as expected, before returning to the bulk unaffected microstructure. The high hardness of the treated near surface (3mm) is due to the presence of martensite. The martensite phase forms in the region when the austenite, generated by prolonged heating, is rapidly cooled. The transition from austenite to martensite is almost instantaneous and without sufficient time for carbon to diffuse out the result is a highly strained, dislocation-dense phase. The body-centered tetragonal structure of the martensite phase contains very few usable slip systems, which limits plastic deformation. Furthermore, the carbon trapped within the phase under rapid cooling is in solution, providing a solution-strengthening effect. Well beyond this martensitic layer at 6mm the microstructure is unaffected by heating and remains in the as-forged state. 6mm was chosen as an appropriate minimum depth for future analysis

as no heat treatment effects were evident at this point. With appropriate sample extraction

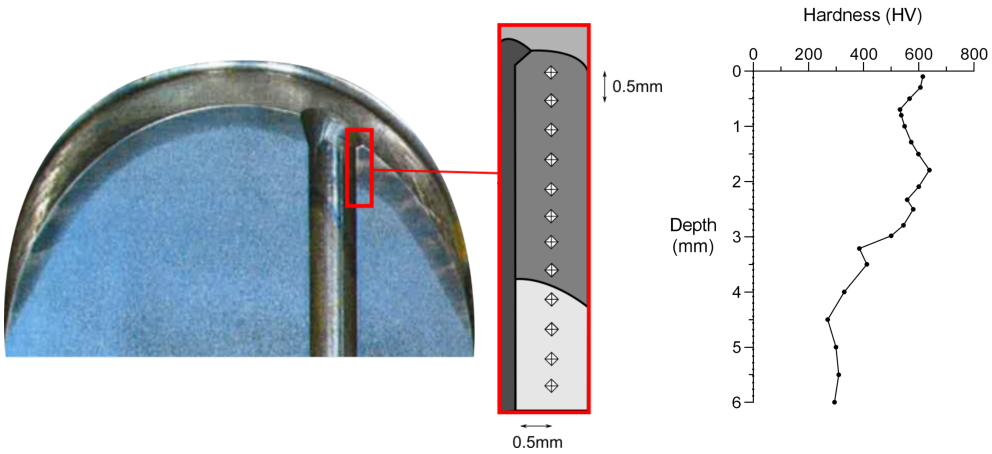

Figure 5.1: Schematic outlining the position of indentation measurements relative to the hole and bearing surface and the obtained hardness values

locations and inspection methods identified, it was possible to compare the influence of the drilling operation on the surface integrity of industrial and research specimens. It was not possible to compare surface finish as the crankshaft samples had evidence of oil burn and dirt entrapment from operational use. Hardness was used instead since any differences in the machining operation would likely present themselves in changes to the near-surface hardness profile due to heat transfer. Cross-sectional specimens were extracted from crankshaft bearing samples at a hole depth of 6mm in an attempt to eliminate heat treatment effects, as recommended in the previous section. The tests were carried out in an 5 x 2, equiaxed 0.5mm x 0.5mm array starting at a depth of 0.1mm below the machined surface. These measurement depths were chosen as they are a sufficient distance apart to negate proximity and edge hardness effects. The average of the five measurements at each depth was calculated and plotted in Figure 5.2 alongside the crankshaft hole samples. Most samples demonstrated

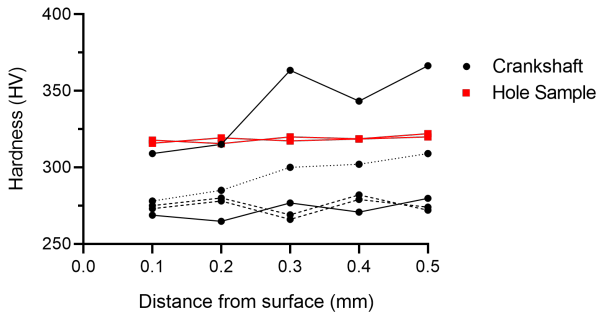

Figure 5.2: Micro-hardness measurements of drilled holes from crankshaft and research samples with line styles to represent different hole samples

a consistent hardness with depth, indicating that the the effects of drilling did not extend to the initial measurement depth of 0.1mm. One sample exhibited a significant increase in

hardness with depth. This specimen was taken from a bearing with an angular hole drilling and upon visual inspection it was noted that the later indents had passed into the induction-hardened layer. This is further explained by Figure 5.3, which demonstrates the effect of hole angle on the outcome of hardness measurements. An internal company report identified a similar phenomenon, with a positive trend in hardness as the measurement location moved away from the hole surface [53]. The previously assigned minimum measurement distance was subsequently increased from 6mm to 10mm to counteract this phenomenon. It must

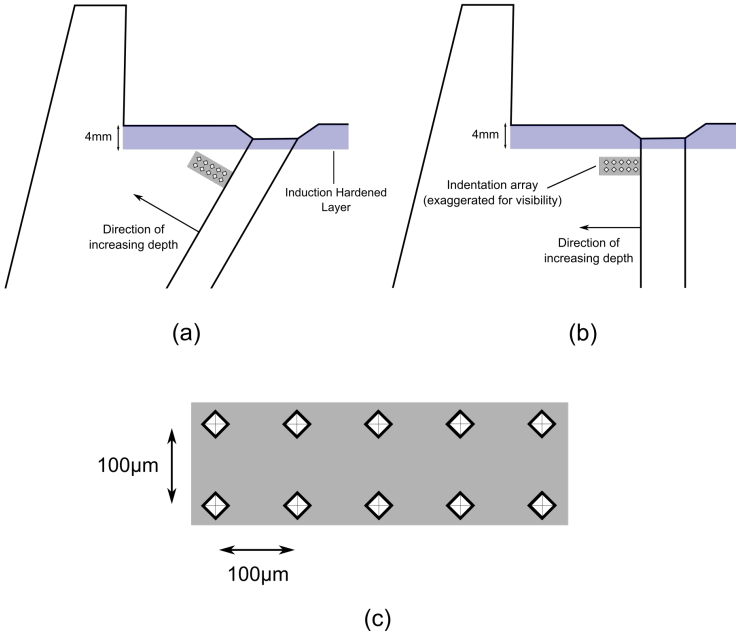

Figure 5.3: Indentation locations on crankshaft specimens for (a) angular drilled and (b) cross-drilled specimens as well as (c) Indentation array geometry

be noted that whilst identical tooling, material composition, material pre-processing, and lubricant specifications were chosen to accurately reflect industrial drillings, the fixturing, component rigidity and geometry differ. During crankshaft drilling the component is fixtured at either end, creating a two-point beam bending system. This is less rigid than the solid block test workpiece bolted to a base plate with drilling force applied in line with the fixture [54]. Furthermore, crankshafts are typically designed with either angular holes that run from the pin to the main bearing or cross-drilled holes that are perpendicular to the bearing surface. In both scenarios, the tool engages with a convex spherical bearing surface which reduces stability on the hole entry and increases the likelihood of tool-deflection and vibration. Since the area of interest for this study is 10mm below the hole entry, the tool is likely to have been stabilised by contact with the pilot walls by this point, so fixturing and geometry differences were assumed to be negligible.

This section identified a suitable minimum measurement depth of 10mm, which is not affected by further material processing steps that are out of the scope of this thesis. This allows any

samples generated in this research to be compared to industrial components with confidence that the drilling process is the main contributing factor to the surface integrity of the parts.

5.2 Process Analysis and Hole Validation

With a suitable hole comparison depth identified, this section moves forward to establish an appropriate workpiece fixturing system that stabilises the workpiece during cutting and ensures accurate transmission of cutting forces from the workpiece to the dynamometer. Then methods of processing these captured cutting force signals that are appropriate for monitoring of the hole drilling process are established.

5.2.1 Fixturing

To accurately monitor the machining forces and avoid vibration-induced error, a workpiece must first be fixed rigidly to a dynamometer. This requires a bespoke fixturing system for each machining application. Initial drilling tests were conducted to establish a suitable workpiece fixturing system for future drilling trials. 140 holes were drilled to a depth of 12mm in a workpiece of 4140 Steel with 8mm Sandvik R840 Solid Carbide tooling. The holes were machined in blocks of ten to allow tool wear measurements to be taken intermittently. The workpiece was clamped in a Kurt DX6 workholding vice fixed to a Kistler 9255B bed-dynamometer. The vice was chosen as it was rigid and simple to set up, but required verification as it was unknown whether the large footprint and weight would cause errors in the Dynamometer. As the workpiece was clamped in a vice and not fixtured directly to the dynamometer, the exact position of the holes with respect to the dynamometer force transducer piezos was unknown. As such, torque could not be calculated in post-processing and only vertical thrust force, F_z could be measured. This was deemed sufficient to validate the drilling cycle and identify anomalies. The machining cycle was programmed to machine holes in blocks of ten to reduce experimental and post-processing time, as illustrated in Figure 5.4.

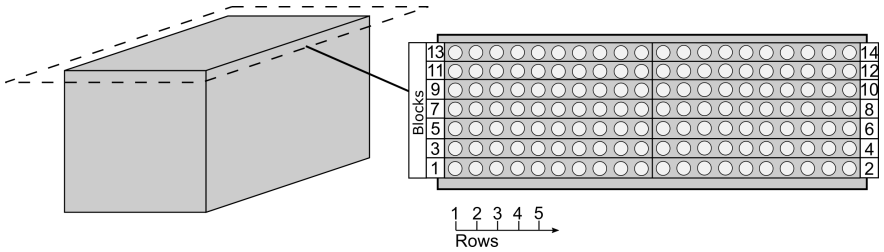

Figure 5.4: Machined workpiece with groups of holes separated into numbered blocks of ten and the direction of rows labelled. Despite the labelling convention, all blocks were machined from left to right

The progression of the measured average thrust force, F_z across the hole with increasing number of holes and blocks drilled can be seen in Figure 5.5. Groupings with linear gradients are sets of 20 which run from the left side of the workpiece to the right. Whilst the increase is less than 100N, a clear pattern is visible that may signify a setup or material property issues that could influence future experiments. Upon first inspection the repeating upward trend looks similar to a rise due to thermal drift in the dynamometer. However, the dynamometer was zeroed between blocks of ten, meaning thermal drift would present itself in blocks of 10 rather than the 20 seen here. In addition, thermal drift is unlikely to have impacted any of these results as the workpiece was isolated from the dynamometer through a vice, through-tool emulsion coolant was used, and a drift compensation function was applied to the data during post-processing. When this trend was noticed, individual data files were inspected and no significant drift was identified. Hardness testing was performed across the

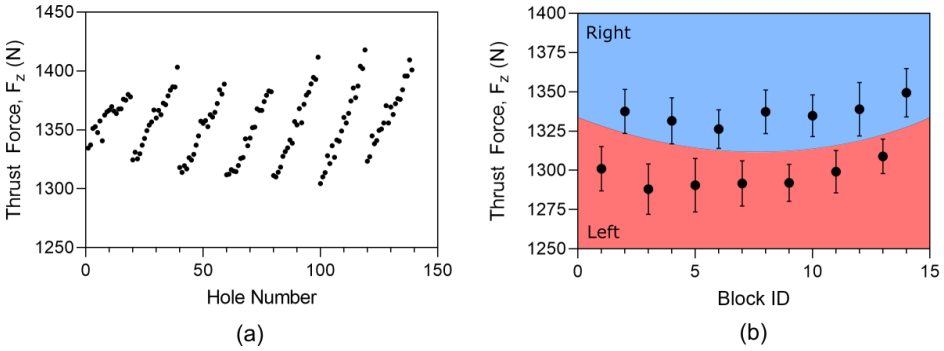

Figure 5.5: Thrust force progression (a) with increasing number of holes drilled (b) for each blocks of ten programmed holes

length of the workpiece surface with consistent results, ruling out material variation as a cause of the pattern. Thrust Force, F_z was calculated by summing the vertical force at the four individual dynamometer piezos. The force captured at an individual piezo was expected to be proportional to the distance between the piezo and the applied force at the tool. The contribution of the individual dynamometer piezos as a percentage of the overall force signal was calculated for all holes, and a bias to the right-hand pair was identified. This was attributed to a bending moment generated by the vice position during drilling. To mitigate this issue a new fixturing system was designed and manufactured. The fixture system utilised two riser blocks to lift the workpiece off the dynamometer. An assembled image of the workpiece, fixture, and dynamometer system is shown in Figure 5.6(a). 4140 Steel was used for simplicity and rigidity and counter-bored bolt holes were machined to ensure repeatable assembly. The block was mounted centrally to the dynamometer and hole position relative to the dynamometer piezos was known, as highlighted in Figure 5.6(b). Furthermore, reduction in machinable volume was minimal and the raised position enabled through-drilling and the study of the hole-breakout. Drilling tests were repeated and yielded a gradual increase in force and torque with each hole drilled and minor variations due to

individual hole dynamics, as expected. There was no evidence of a geometric-dependent force response, indicating that the new fixture system had solved this issue and was suitable for all future drilling trials.

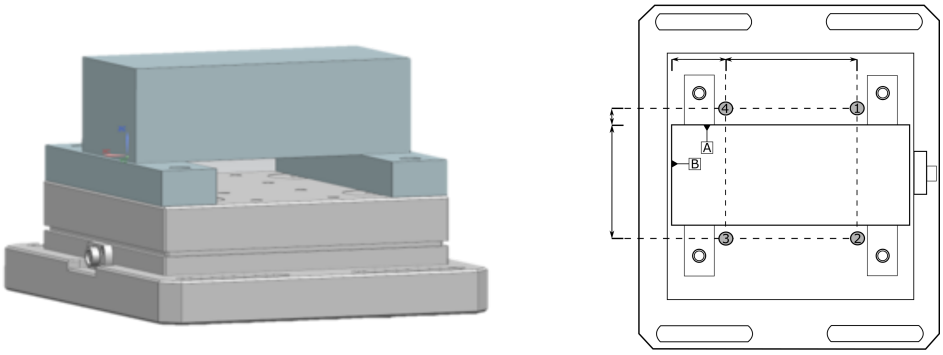

Figure 5.6: (a) Assembled fixture system with the workpiece bolted rigidly to two machined blocks (b) Fixture schematic including the position of x and y datum faces relative to the four dynamometer piezos

5.2.2 Signal Processing

Whilst industrial machining is widely considered to be a reliable process, the quality of a machined surface is susceptible to vibration-induced error, chip jamming and tool wear. Certain detrimental features such as scratches and poor finish are immediately evident upon visual inspection, whilst other features such as hole diameter tolerance and circularity require more extensive and costly analysis. Whilst producing holes with these errors is often unavoidable, it is important to identify them in works such as this so they can be excluded from analysis if required. Process monitoring offers a suitable method of pre-validating hole quality and identifying suitable holes for analysis. Force dynamometers are regularly used to monitor the repeatability of machining processes, since process variation can be identified by changes in cutting forces. These forces captured during machining require post-processing to identify the in-cut signal, to segment individual holes, and apply the appropriate analysis tools.

Segmentation is used to extract useful sections of the cutting data for use with various time and frequency domain analysis tools. It reduces the data set's size and ensures that analysis is conducted solely on the useful in-cut periods of the data signal. Several test holes were drilled in an AISI 4140 steel workpiece in the as-rolled condition to attain sample force data sets. The cutting signals' exact start and end points were identified with a threshold function that computes a moving average and detects when the vertical force increases/decreases by more than 100N. The function was validated against manual segmentation and deemed sufficiently accurate because the in-cut time was within 5 data points. Further refinement

was unnecessary because the effect on the calculated average force is negligible. This process is illustrated in Figure 5.7. During the monitoring of cutting forces, signal drift can occur,

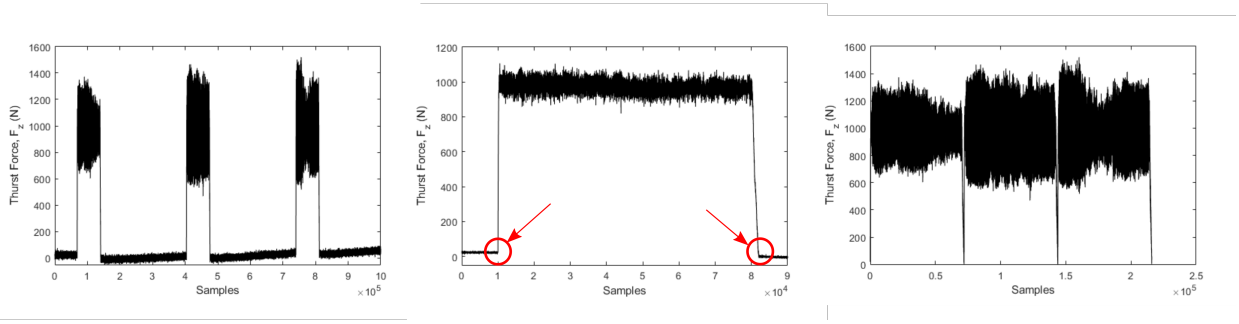

Figure 5.7: Segmentation of the in-cut portions using a moving average threshold function

where the zero offset position changes over time. Traditionally, thermal drift is accounted for by removing the gradient and offset of the initial seconds of the dynamometer signal from the entire signal. This assumes linear, invariant drift across the machining cycle. While this may be effective in most cases where the operation and sources of drift are well known, the characteristics of this individual operation have not been well studied. An improved drift compensation procedure was programmed in MATLAB whereby a fitted line of the two out-of-cut regions immediately prior and following each segmented hole signal is averaged and removed from the in-cut signal, as shown in Figure 5.8. The gradient of these two out-of-cut regions clearly differs, with a shallow negative gradient in the pre-cut signal and larger positive gradient in the post-cut signal. This same function is applied to each drilled hole individually. Thus, if signal drift varies with time the captured in-cut signal can still be extracted from the captured force profile. This is particularly beneficial when examining the gradient of the cutting force profile across the duration of the hole. An increase or decrease in force with tool depth could, in theory indicate problems with chip evacuation or heat generation that are of interest to the machinist. If signal drift is not accounted for, the force gradient cannot be determined accurately and these features cannot be used to characterise the drilling process. These segmentation and drift compensation functions were applied to all future force datasets in this thesis.

5.3 Tool Wear

5.3.1 Introduction

Cutting tools are subjected to significant mechanical forces and temperatures as they deform the workpiece material, resulting in the removal of tool and coating material, adhesion of workpiece material, and chemical diffusion. The gradual degradation of tool integrity during machining is termed tool wear and is dominated by three main types: abrasion, adhesion, and diffusion. Abrasion, the most common wear mechanism, occurs when hard chip material

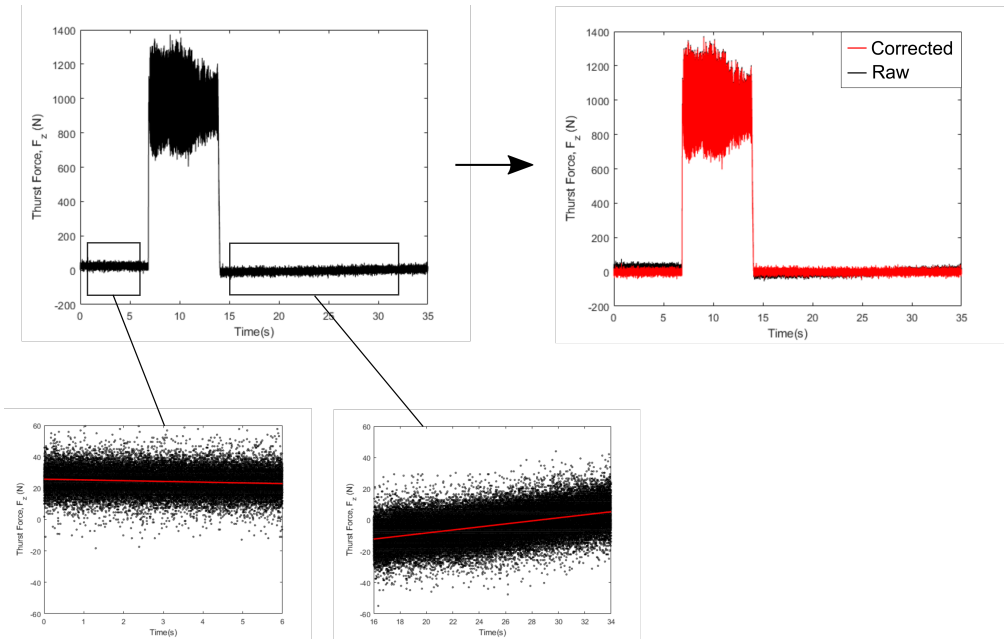

Figure 5.8: Method of compensating for signal drift and offset by deriving lines of best fit from pre and post-cut force signal and removing an average of these from the in-cut signal

contacts the tool and chips away the tool's surface. Abrasive wear usually leads to stable and predictable tool life. The commonly used flank wear criteria is a measure of abrasive wear. Adhesion is the spot-welding of workpiece material to the tool due to high friction and contact pressure at the sliding contact. Adhesive wear presents itself as a built-up edge that leads to inferior cutting mechanics and poor part quality. Once the adhered material reaches a critical mass it breaks off, taking tool material with it. Adhesion is accelerated during high-speed machining due to the greater contact temperatures and can lead to abrupt and catastrophic tool failure. However, it can be reduced with the application of an appropriate lubrication strategy. Finally, diffusion is a chemically driven process where the tool and workpiece interact at the high-temperature contact, permitting diffusion of atoms across the boundary and subsequent weakening and embrittlement. Diffusion is more apparent at higher machining temperatures, where chemical reactivity at the tool-workpiece contact is increased. Machining of materials with a high chemical affinity to the tool material also increases the likelihood of diffusion wear. Crankshaft drilling is typically conducted at high machining speeds. During orthogonal cutting of 4140 Steel with an uncoated tugnsten carbide tool, the wear mechanism was a combination of abrasion and adhesion at high cutting speeds [55].

Whilst these have been presented as three distinct wear mechanisms, the tool will experience a combination of these wear modes over its lifetime. The progression of tool wear with cutting time typically follows a variation of the Taylor Tool Wear curve [56], with three distinct sections: initial rapid onset, a steadily increasing secondary wear regime, and sharp failure. But, the exact behavior is unique to a particular combination of tooling, material,

and operation and must be characterised on a case-by-case basis. It is important to establish the time-dependent progression of tool wear for the drilling operation to maintain hole quality, minimise downtime and achieve part tolerance. A total cutting time limit is typically assigned to maximise machining time whilst avoiding deterioration of part quality and catastrophic tool failure. This limit is usually based on the wear of the flank face and may either be taken from manufacturer recommendations or determined in-house. A widely accepted tool flank wear limit for a tool of 8mm diameter is 0.3mm, at which point the tool would be removed from service and scrapped or reground.

The relationship between tool wear, cutting forces and surface integrity in machining has been studied extensively [57]. Variation in surface integrity is largely driven by changes in cutting temperature and tool-material contact conditions, which are both dominated by tool wear and yield a change in cutting forces. Therefore it can be reasonably assumed that holes drilled with similar cutting forces and levels of tool wear will exhibit similar surface integrity properties. A common experimental approach for characterising tool wear is to machine a workpiece at the desired parameters and take images of the cutting tool with an optical microscope at discrete time intervals. These images can then be post-processed at a later time and the time-wear graph can be used to assign a maximum cutting time limit based upon a pre-determined wear limit. Then, during industrial operation tools can be visually inspected for major signs of damage, without the need for frequent time-consuming measurement which impacts production costs. Practically speaking, for industrial operations avoidance of tool breakage and meeting tolerances are the primary concern. But tool wear can still be detrimental to hole quality within the acceptable wear limit. For research purposes, this would impact the validity of surface integrity analysis and any theories generated upon the basis of the machined surface condition. To solve this problem, a coupled surface quality and tool life trial was completed, where surface roughness and tool wear were measured in identical discrete intervals.

5.3.2 Tool Wear Study

140 holes were machined to a depth of 96mm in a workpiece of as-rolled 4140 Steel using 8mm Sandvik Corodrill 865 Solid Carbide tooling and through-tool emulsion coolant. A depth of 96mm was chosen as it generates a length-to-diameter ratio of 12, which is commonly seen in industry. Holes were machined with a cutting speed of 71.5 m/min and feed rate of 0.204 mm/rev, the recommended parameters for this tool and material combination. Pilot holes were machined for all drillings due to the high length-diameter ratio of tooling. The pilot hole acts as a bushing to guide and stabilise the longer, more flexible deep hole drills on entry, when the tool is prone to wander. Holes machined in industry would typically be piloted using a dedicated pilot drill from the same product line, however, an R840 drill was used instead due to stock shortages. This was deemed sufficient as the R840 has a

large point angle, ensuring the chisel edge of the main drill engages with the pilot hole first, followed by the cutting edges. Cutting forces were monitored using a Kistler 9255C Force Dynamometer and holes were programmed to be machined in groups of ten to allow frequent tool-wear images to be taken. Flank wear images were taken at ten-hole intervals with a Zeiss bench-top microscope and measured post-trial. The tool was also inspected for any signs of significant damage. 3D surface topography analysis of the cutting edges with optical profilometry equipment would have allowed the identification of adhered material and micro-scale tool-wear features, but this was not possible due to height restrictions in the equipment. It was also important to capture wear at the drill margin, as damage to the margin could yield poor surface integrity in the hole wall due to impaired contact conditions. Wear in this region is difficult to characterize with optical imaging, since in a vertical position the margins are hidden behind the corner due to the tool taper and in a horizontal position damage is visible but cannot be measured. Instead, a 3D surface topography map of one of the drill margins was taken before and after machining using a Bruker Alicona InfiniteFocusSL. After machining, the arithmetic mean surface roughness, R_{a} of the first and final hole in each block was measured using a Mitutoyo SurfTest SJ-210 Mobile Profilometer. Tool wear was contrasted against cutting force and surface finish data to identify deterioration in tool integrity. Machining chips were also analysed to identify any significant changes in chip morphology and microstructure that could have been caused by changes in temperature and friction due to tool wear.

5.3.3 Tool wear Progression

Tool flank wear was measured in discrete ten-hole intervals across the entire hole set. The evolution of flank wear, V_{b} with cutting time is presented in Figure 5.9. Flank wear initially increased rapidly, reaching 0.025mm within the initial 10 holes. Wear then increased steadily by 0.004mm/10 holes, reaching 0.08mm by the final hole. This is well within the manufacturer's recommended wear limit of 0.3mm. There were negligible changes to the margin geometry and no evidence of a significant build-up of adhered material on the cutting edges or margin. The change in surface roughness across the 140 holes was also measured and no statistically significant degradation in surface quality was identified. Thrust force and torque were calculated during post-processing for all 140 holes to further validate the consistency of the drilling process. 140 holes corresponds to a total surface distance of 1600m. Thrust force trended slowly upward as the tool cutting time increased, from 930N at hole 1 to 1000 at hole 140. Torque was high initially, before dropping down after 5 holes. Following this, torque trended slowly upward across the hole set. Torque as calculated with this method was found to fluctuate wildly due to the rapidly changing direction of applied force as the tool rotates. Averaged over the entire hole these fluctuations were negated. There was no evidence of excessive forces in any holes across the data set. Machining swarf was also inspected. Assessing chip morphology and microstructure is a fast, reliable method of

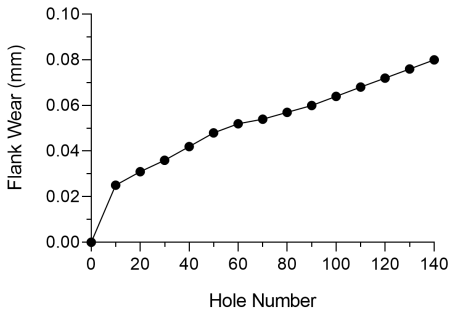

Figure 5.9: Progression of tool wear across the entire hole-set, measured in discrete ten-hole intervals

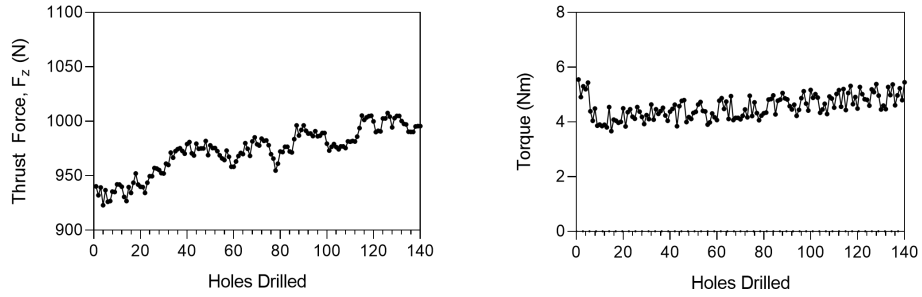

Figure 5.10: Progression of Thrust Force and Torque during drilling with increasing number of holes drilled

establishing the baseline quality of a machining process. Chips were gathered intermittently during machining in identical increments to tool wear and later inspected. Visual inspection identified no visual change in chip colour which would indicate excessive temperatures. This was further verified by characterizing the chip microstructure with optical microscopy. To prepare samples for optical microscopy, approximately eight chips were mounted in a single bakelite puck in various orientations, so all regions of deformation could be assessed. The mounted chips were then ground and polished to a mirror finish using the procedure outlined in Section 4.4. Care was taken to remove minimal material due to the small thickness of the chips (0.102mm). To reveal the microstructure, the polished chips were chemically etched by dipping in 2% Nital etchant in 10s increments. Nital reagent preferentially reacts with the more chemically active grain boundaries, generating a topography that is visible under light. A micrograph of a chip taken from the final block of holes is shown in Figure 5.11. The secondary shear zone is small, indicating no excessive friction at the chip-rake interface and while adiabatic shear banding is present, it is insufficient to suggest excessive heating. The tool wear images, cutting force data and chip morphology all suggest the tool remained within the secondary wear region throughout the 10-140 hole period. There were minor fluctuations in force attributed to slight dynamics and material changes, but there were no noticeable anomalies. There were also no significant changes to surface roughness

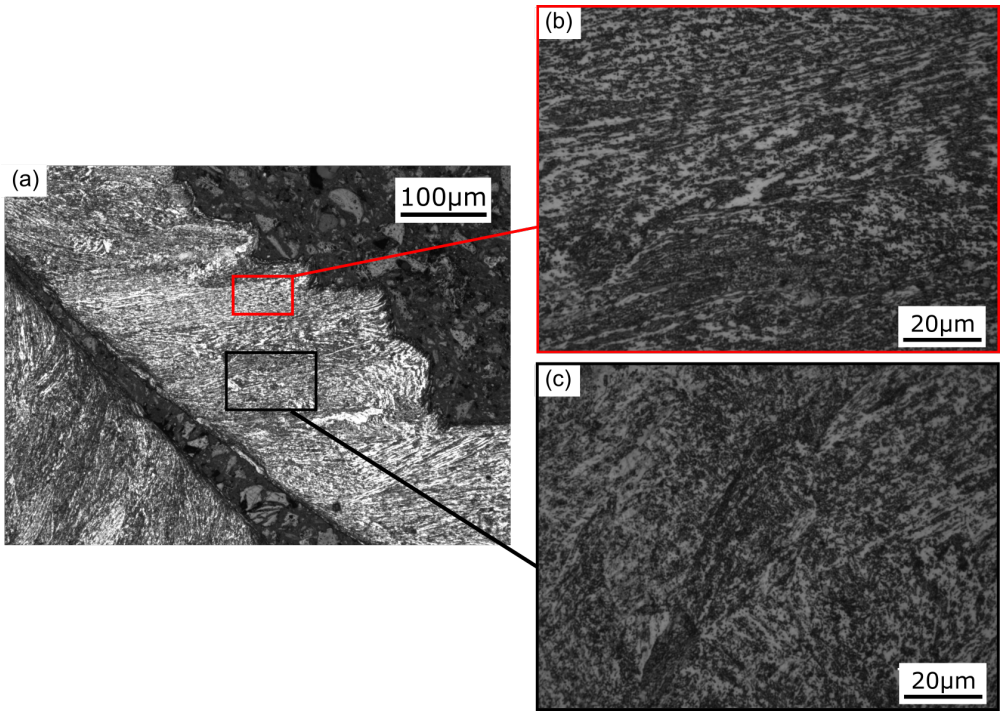

Figure 5.11: (a) low magnification full chip cross-section with regions of interest highlighted and minor adiabatic shear banding (b) magnified region of heavy unidirectional deformation (c) magnified region of limited deformation

as the total cutting distance increased. Henceforth, it was assumed that if the number of holes drilled with each tool remained below 140, any holes selected for inspection that did not exhibit anomalous cutting forces could accurately represent the entire hole set. Whilst tool wear is not the focus of this thesis, this methodology for pre-validating the suitability of machined holes for structural analysis is employed throughout. Since the assigned operating range was well within the manufacturer's recommended cutting time limit for this tool design and there was no intention to exceed the manufacturer's recommended parameters, it was deemed acceptable to use this criterion for all future research in this thesis. This method yielded an improvement over simple tool-life studies by establishing a period of stability within which research could be conducted. With a suitable cutting time range identified, the tool need only be inspected when changing machining parameters.

It was also noted that since the operation was stable over the 10-140 hole range it may be possible to use a single tool for multiple operations. For instance, when assessing the impact of a variable such as cutting speed on surface roughness, it may be possible to machine at two separate speeds using the same tool. This is contrary to the standard methodology in the literature and particularly in parameter optimisation studies, where a fresh tool is regularly used for each parameter set/operation. The use of a new tool is good research practice because the magnitude of tool wear is known to influence cutting mechanics and researchers are able to mitigate tool condition as a variable. But, in doing so it can be argued the research is less industrially applicable because performance is rarely evaluated

in the secondary wear regime, where tooling will spend the majority of its time in industry. Provided wear follows a stable progression, it may be more beneficial to conduct trials with tools in the secondary wear regime. By testing the tool in the condition it is likely to be in when machining industrial components, research results may be more applicable to industrial applications. Whilst this can be achieved when using a new tool for each variable, it requires more material usage and mirroring of tool wear between tests. That is, tools must be pre-worn to the same level of wear before the primary tests are conducted. This is expensive and time-consuming. A further benefit to operating with a single tool is the removal of any influence of the prepared tool geometry. Tool preparation can vary within or even outside the manufacturing tolerances and variation in edge radius can yield changes to cutting mechanics and result in poorer surface quality [58]. Operating with a single tool negates these geometric tolerance effects, provided tool wear is minimal. This new methodology is not suitable for tool wear studies, but for surface integrity analyses where the number of holes is already limited by the extensive hole analysis time, it offers a great improvement. Furthermore, cutting parameters must remain within the known operating range of the tool as provided by the manufacturer to prevent excessive wear.

5.4 Inspection Methods

In this section holes generated during Section 5.2 are used to examine surface and hardness inspection methods and establish a best practice for characterising drilled holes.

5.4.1 Surface Finish

Surface finish describes the topography of the machined surface and is used regularly in the literature as an indicator of the quality of a machining process. Mobile profilometers such as the Mitutoyo SurfTest SJ-210 used previously in this chapter enable fast, simple measurements that can be completed in-situ, without the need for preparation and sectioning. However, the sampling length is short and accuracy is dependent on accurate perpendicular alignment of the stylus and hole axis. For the purpose of predicting component performance, where more complete characterisation is needed, more advanced measurement methods such as optical profilometery are required. Whilst mechanical profilometers use a contact stylus to capture the form of the surface along a single plane, an optical profilometer can take 3D spatial images and scan large areas of components quickly, as shown in Figure 5.12. An example of this type of equipment is the Alicona InfiniteFocusSL Focus Variation Microscope. 3D surface topography scans of a machined hole surface produced in Section 5.3 were taken using an Alicona InfiniteFocusSL 3D Optical scanner to evaluate its suitability for the measurement of holes. The system slices the area of interest into layers of increasing depth, takes a surface topography scan of successive layers and then stitches them together to form a final image. Form effects of various orders can be removed including the hole curvature.

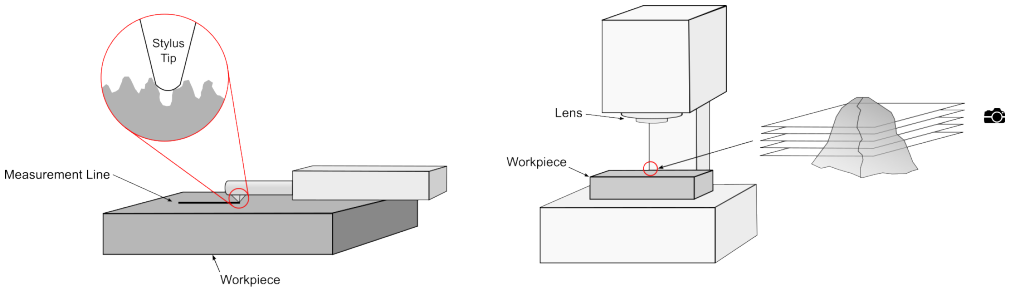

Figure 5.12: Schematic of the method of operation of a (a) contact and (b) optical profilometer

In this instance a Gaussian Planar Surface model was used to estimate the form of the hole and remove the curvature from the profile measurement. The curvature as estimated by the form removal function was compared against the hole diameter measured with digital calipers prior to sectioning to validate accurate form estimation. After form has been removed, surface topography analysis can be performed in either 2D or 3D. 3D analysis provides the user with spatial area roughness parameters such as S_{a}, which describes the average height of points on the surface relative to the mean plane. These are useful for contact surfaces and those without a dominant roughness direction, but the drilled oil holes commonly exhibit poorer finish in the axial direction due to the drill in-feed. Peaks and valleys in this direction are susceptible to crack initiation under loading which reduces fatigue life. To capture these features, 2D line scans can be taken in this direction at various widths. These evaluate the surface along a single 2D plane. Roughness parameters such as R_{a}, the average point height relative to the mean line can then be extracted. Evaluation of 2D profiles taken in the feed direction is most suitable for this application.

The width of this 2D line scan, the scanning width, can be adjusted based on the desired profile characteristics and was found to heavily influence the extracted profile. As the width is increased, profiles adjacent to the selected line are also measured and averaged to yield the final topography. A larger scanning width increases the number of measurement points, but, since these points are averaged, the sensitivity to features such as large peaks and valleys can be reduced, resulting in lower measured surface roughness. This is demonstrated clearly in Figure 5.13, which compares 1 μm and 30 μm scans at the same location. As width increases, there is a significant reduction in the height of peaks and valleys and an increase in the width of asperities due to an averaging effect. Large features that extend a long way around the circumference remain visible but are reduced in magnitude and some smaller features are removed altogether. So, increasing the scanning width may appear to be counterproductive. Indeed, research rarely makes note of scanning width or this effect, and contact profilometers, which are prevalent in the literature, use a low number of profiles. However, without significant repetition, surface quality measurements can be heavily

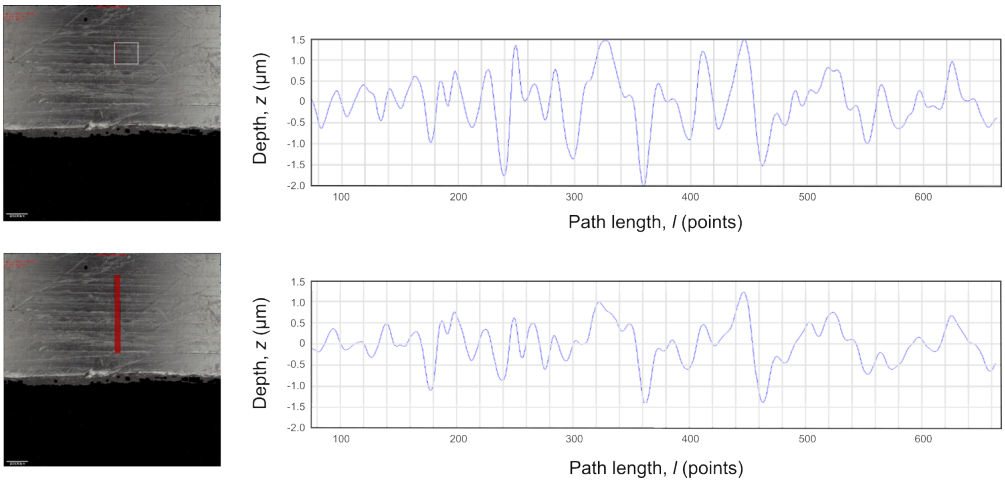

Figure 5.13: Surface scans at 1μm and 30μm scanning widths alongside the extracted profiles with identical y-axes

influenced. Furthermore, large features are statistically more likely to be captured because of the greater scanning area, albeit at a reduced magnitude. A short study was conducted to characterise this change in the extracted profile, further increasing measurement accuracy and attaining an optimal trade-off. The mean arithmetic roughness, R_a, maximum profile height, R_z, and root mean square deviation, R_q were identified as suitable comparison metrics for all holes. R_a represents the average deviation from the mean height of the profile and is widely used as a measure of surface quality. Despite its frequent use, it is insensitive to random profile features and may be less affected by the width of the scan. R_q is the standard deviation of the profile height and is slightly more influenced by scratches and contamination. R_z captures the peak to valley height and is useful to identify the presence of deep scratches or grooves and sloping peaks, such as machining marks and chip scratches. R_z is most sensitive to large profile features and is theoretically most likely to be affected by scanning width.

R_z, R_q, and R_a were calculated as the scanning width increased incrementally from 1 profile (1 μm) to 45 profiles (45 μm), with results displayed in Figure 5.14. All three parameters demonstrated an inverse S-shaped function. R_z was most affected with a sharp decrease after 10 profiles and a later leveling off point. This corresponds to the previous smoothing of peaks in Figure 5.13. Since the change in parameter values from 1-10 profiles was minimal, 10 profiles was selected as an appropriate scanning width. This improved the measurement reliability without sacrificing the capture of important profile features. It was also decided that R_q was not necessary in future investigations due to the similarity between the R_a and R_q curves. Optical profilometry was shown to sufficiently characterise the surface quality of machined holes, provided form is accurately estimated and removed, and a suitable scanning width is selected.

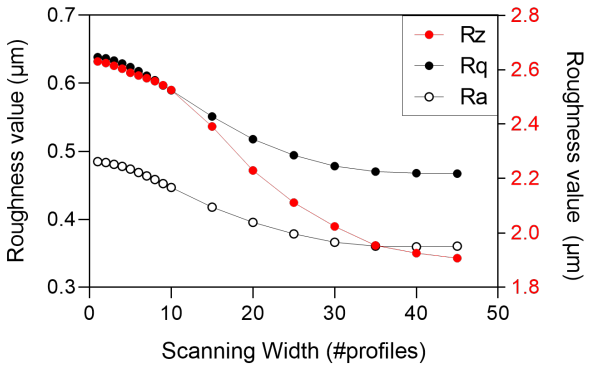

Figure 5.14: Change in surface roughness parameters with increased scanning width

5.4.2 Hardness

Hardness is a key surface integrity metric that describes the resistance of a material to local plastic deformation. Hardness manifests itself in materials because of irregularities in the crystal structure that impede the relative displacement of planes of atoms. During machining, material at the near-surface plastically deforms and irregularities known as dislocations pile up at grain boundaries and can be impeded by a variety of other features. As a result of the greater chance of dislocation-dislocation interactions, the greater the near-surface dislocation density, the less readily the material deforms and the harder the surface is. This is important in oil holes, as a harder oil hole surface is more likely to resist the initiation of cracks that cause catastrophic fatigue failure [59].

Hardness can be assessed with a number of techniques, but indentation testing is the most commonly used in machining research. During indentation testing, an indenter tip made of a high-hardness material is pressed into the surface under a precise force, and the size of the indent left behind is used to calculate the hardness. A dwell time is also used to mitigate dynamic loading effects. Before hardness testing, it is important to assess the suitability of the material for testing and determine a suitable load for the chosen specimen type. Bulk high-load material hardness measurements are a good method of understanding the global material properties and produce a large indent of the order of hundreds of microns that is resistant to error due to poor preparation and incorrect measurement. But, a typical near-surface machining affected layer is 10-100 μm thick and would not be resolvable under these limits [60, 61, 62]. Characterisation of a machining-affected layer requires a sufficiently small indent to sit within this region. This is further complicated by the requirements of ASTM E384-17, under which all measurements should be taken at a minimum distance of $2.5\times d_{\mathrm{i}}$ from the edge of the specimen and each other to mitigate edge effects due to lateral displacement of material [63]. Preliminary testing was conducted on the material to find a suitable method to characterize the near-surface layer.

Initial hardness measurements were taken at six locations in a test sample to identify an approximate diameter of the indent, d_{i}. The tests were completed using a Struers Durascan Microhardness Indentation tester with a force of 9.81N and a dwell time of 15 seconds. The method of operation of this machine is described in Section 4.5.1. The samples were polished to a mirror finish to reduce errors due to changes in surface height. A relatively high load was used because this test was purely to determine the approximate hardness of the material. After retraction, an automated image processing algorithm was used to measure the indent. The system initially struggled to measure the indent as the etched microstructure interfered with edge detection. Manual detection was used instead, but accuracy was poor. At the low magnification used for measurement, small changes to measured diameter can yield significant changes in the calculated hardness. A colour correction was applied to the grayscale hardness image, which more clearly delineated the indent, and solved this issue.

The average indent diameter across the six repeats was 78μm, corresponding to a hardness of 305 HV. This load is too high for further testing since a minimum edge distance of 200 μm would be required to conform to ASTM E384-17 [63]. An indent diameter of below 10μm is required to take measurements reliably within the machining-affected area of interest. The load required to produce an indent of this size is 0.159N, as calculated from Equation 5.1 using the calculated hardness of 305 HV.

$$F = \frac{htVgd^2}{2\sin\left(\frac{\alpha}{2}\right)} = \frac{300 \times 9.81 \times 0.01^2}{2 \times \sin\left(68\right)} = 0.159N \tag{5.1}$$

The closest indenter load available to this was a HV0.01 test at 0.0981N. The tests were repeated under this load (HV0.01), with a resulting indent diameter of approximately 8 μm. Although this was now sufficiently small to resolve the machining affected layer, the indent was difficult to resolve with optical microscopy. As seen in Figure 5.15, it is difficult to accurately delineate the poorly focused indent edges due to light reflecting at the edge boundary. The optical images are captured at a resolution of 2048×1536 pixels and the physical width of the image as calculated from the scale bar is 120μm. This corresponds to a width per pixel of 0.06μm. Imperfect focus further enhances this error. A 10 pixel error in measurements yields a hardness change of 39 HV. This is a widely recognised problem in research, and various image process algorithms have been developed to aid the measurement of hardness test indents. Various image processing algorithms were tested with limited success. The sample could have been transferred to alternative, higher power microscopes, but this would have required manual assessment of each indent and introduced the risk of indent misidentification.

Optical profilometry was a potential solution to this issue. The Bruker Alicona InfiniteFocusSL was used to capture the surface topography of the indented regions in an attempt to

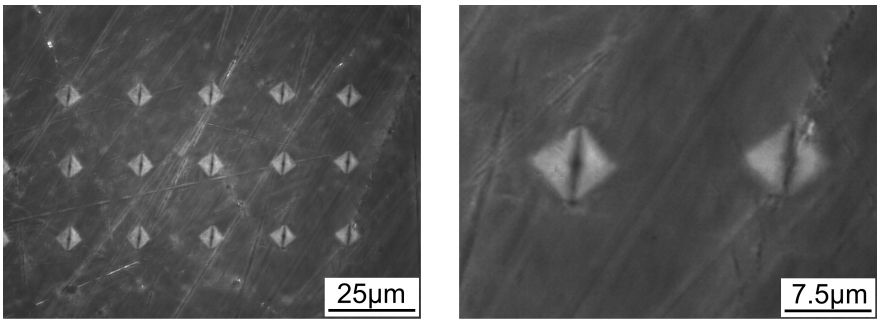

Figure 5.15: (a) Optical micrograph of an indented sample under 100x zoom and (b) magnified further in post-processing

measure the diameter. The system struggled to capture the geometry due to the reflection of light and it was difficult to delineate the edges. It was also a time-consuming process. Microhardness testing was concluded to be insufficient to accurately characterise the hardness profile of the near-surface machined layer under these limitations and an alternative method should be sought.

Nanohardness testing capability was identified with a NanoTest Vantage machine that could provide indentation and measurement in a single operation. Since the system has highly calibrated vertical drives, it was able to compute the indent size from the vertical travel depth and the known indenter tip geometry, rather than optical measurement of the indent. This improved measurement accuracy and allowed small areas to be characterised to a high resolution, without the requirement for advanced imaging. Sample preparation was important, since oil films, debris and flatness can impact measurements at this scale. The full system specification and method of operation is outlined in Section 4.5.1.

Whilst this equipment had previously been used to quantify phase variations in materials, analysis of machined holes on this scale is rare in the literature. This presented a unique opportunity to identify minute variations in the microstructure of the machined near-surface that are critical to component performance and often invisible with standard testing methods. A cross-sectional drilled sample of rolled steel with a bulk hardness of 400HV was indented under a 1mN load in 20μm increments from 10-190μm below the machined surface with three repeats. Repeats are necessary since indents this small are subject to error due to micro-scale phase and grain orientation changes. The resultant hardness profile is presented in Figure 5.16. The hardness measured at the near-surface is significantly higher than the bulk material hardness of 400HV for all tests, suggesting that there is significant plastic deformation at this location. All three test profiles then show the same trend of decreasing hardness with depth before levelling out at 50μm. This suggests that for this sample the depth of machine-affected layer is approximately 50μm. There was no evidence of near-surface reduction in hardness that would be associated with edge-spreading. It can

therefore be assumed that the near-surface measurements are representative of the material properties. 10μm is significantly closer than the previous minimum resolvable depth and this method of measurement offers a clear improvement over microhardness testing. It must be noted the variation in hardness between profiles seen here reinforces the need to conduct multiple repeats. The setup time involved with performing nanohardness analysis is greatly increased relative to other test methods, but this was deemed an acceptable trade-off based on the improved results that were seen. Whilst it may have been possible to indent directly

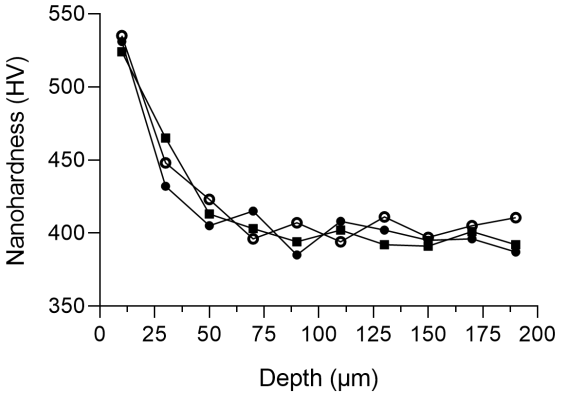

Figure 5.16: Variation of the measured hardness with depth below the machined surface

into the machined surface, the overlap between the radius of curvature and the indenter tip would have introduced a geometric inaccuracy, as illustrated in Figure 5.17. The indent diameter in the curved direction would be larger than the indent in the flat axial direction and the indenter displacement would likely exceed the deformed layer depth, capturing the bulk material beneath. There is also a high risk of equipment damage if the specimen is not centered perfectly. Whilst it may have been possible to grind the surface flat, this would have required high-precision polishing equipment and would have almost certainly damaged or altered the near-surface deformed layer. As such this was not explored as part of this study.

5.5 Summary

In summary, analysis scripts were generated to extract the in-cut signal from grouped cutting data and remove thermal drift using drift correction data from before and after each hole rather than the start of the measurement signal. A fixture system was manufactured to stablise the workpiece and allow thrust force and torque to be measured accurately. A study was conducted to assess a suitable cutting time range for each tool within which all holes machined with the tool are comparable by monitoring cutting forces, surface roughness and chip morphology. 10 holes was found to be a reasonable minimum limit to negate adverse effects from initial rapid tool wear. To this end, no holes machined within the first 10 holes

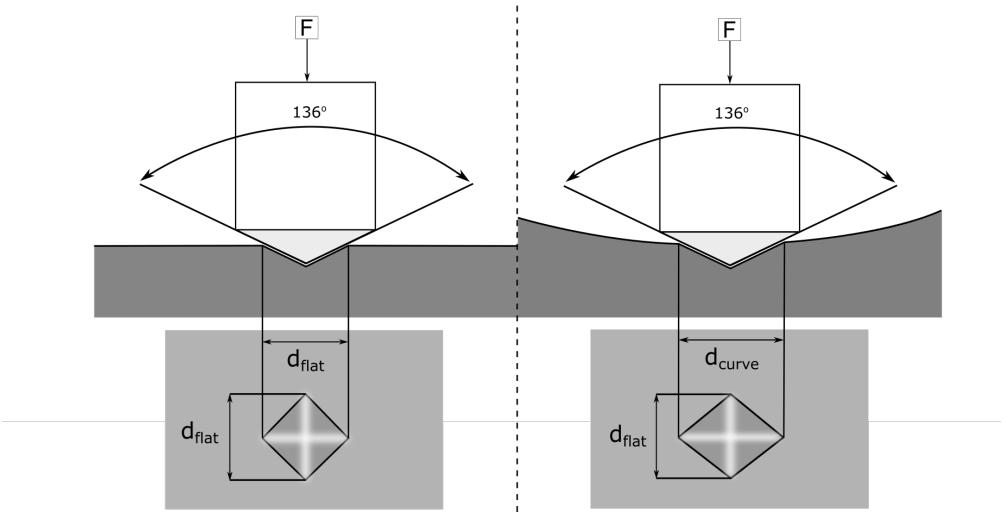

Figure 5.17: Hardness indent test schematic for flat and curved surfaces demonstrating the source of geometric inaccuracy due to curvature

of tool life should be examined and analysed, since condition may vary considerably. The 140th hole was chosen as a maximum since this is the maximum number of holes that can be machined in a single workpiece of material and at this limit wear effects remained minimal. Henceforth, it was assumed that any holes examined within this range would have experienced similar cutting mechanics, provided no erroneous cutting forces were identified. It was also hypothesised that the current standard research methodology of using a new tool for each test variable does not accurately reflect industrial operations, since tooling will spend the majority of time in the secondary wear regime during industrial machining. Instead, it was proposed that a single tool could be used for multiple test variables in surface integrity studies provided the number of holes was limited and tool wear was minimal. This has the further benefit of negating tool edge radius effects that come from manufacturing tolerances and tool preparation. Surface finish and hardness measurement techniques were then analysed to assess their suitability for the characterisation of drilled holes. Optical profilometry with a 10μm profile width yielded satisfactory results and allowed superior characterisation to contact profilometry. Nanohardness testing with automated depth measurement was shown to be the only suitable method of extracting a near-surface hardness profile due to the small depth of heavily plastically deformed layer and difficulty in measuring low-load indents. Finally, examination of an induction hardened crankshaft sample revealed that the oil hole microstructure was modified to a perpendicular hole depth of 6mm, despite the target depth during manufacture of 4mm. 10mm was subsequently chosen as the minimum analysis depth for all future drillings to allow any holes machined in this thesis to be compared with industrial components and eliminate induction hardening effects. The work completed in this chapter established appropriate methods of generating and examining drilled holes for the purpose of investigating crankshaft oil drilling operations.

Chapter 6

Burnishing

6.1 Introduction

Due to the ever-increasing performance demand placed on engine components by emissions regulations, enhancing the fatigue resistance of powertrain components is a crucial concern for automotive manufacturers. Crankshafts in particular undergo cyclic, reversed loading during engine operation and require compressive residual stresses, high hardness, high-quality surface finish, and a suitable microstructure at all surfaces of loaded material to remain structurally sound throughout the product life cycle. Various modern techniques such as deep-rolling and shot peening have demonstrated proficiency in inducing beneficial residual stress fields and have been applied at the crankshaft bearing surface along with extensive finish machining and hardening steps to produce a hard, high-strength surface [64]. These procedures are well represented in the research literature and, in previous decades, numerous studies have investigated the mechanisms that contribute to the generation of an optimal surface [65, 66, 67]. However, the drilled oil hole has received less attention in the literature. Although it is a potential failure site, because of the high concentration of stress, little research has been undertaken to analyse the surface integrity of oil holes. This may be in part due to the past dominance of the bearing fillets as a failure point and the extensive material preparation required to analyse drilled holes. Nevertheless, it was proposed in Chapter 3 that the generation of a high-quality drilled oil hole may be integral to the design of future downsized internal combustion engines.

One plausible technique to achieve this objective is the use of burnishing to plastically deform the drilled hole wall and induce grain refinement and compressive residual stress beneath the surface. A burnishing tool typically uses a hardened spherical or cylindrical pin or roller that smooths and finishes surfaces by applying pressure and rolling or sliding over the surface. Since the applied force is greater than the yield stress of the workpiece material, asperities are flattened and the near-surface material is deformed. As a result

of the flattening of asperities, the surface roughness is greatly reduced, often yielding a mirror finish. Because the near-surface is plastically deformed, the microstructure remains in a highly strained compressed state, with associated beneficial residual stress. In addition to the generation of compressive residual stresses, burnishing induces modifications to the sub-surface microstructure, dislocation density, and material hardness. A schematic of the burnishing process is shown in Figure 6.1.

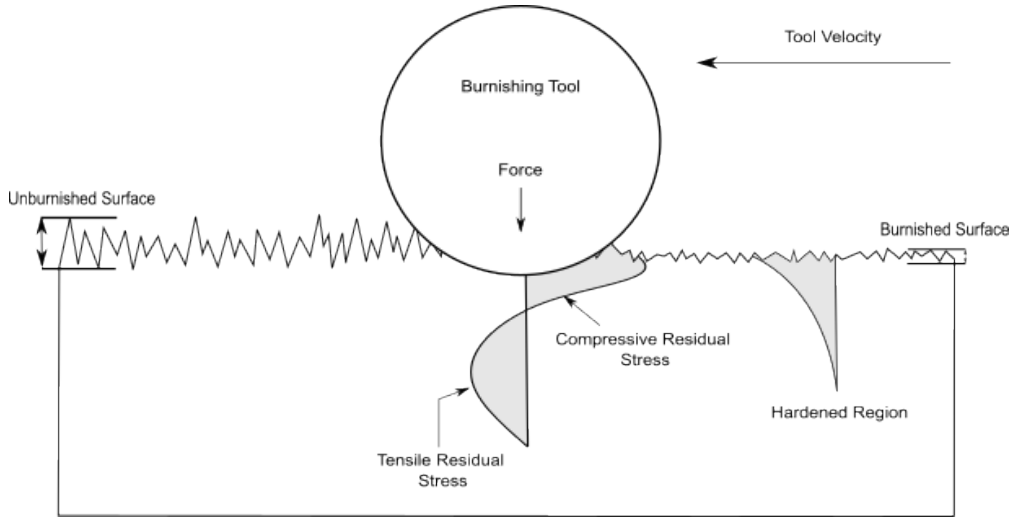

Figure 6.1: A burnishing schematic highlighting the applied force and movement and the associated effects to the near-surface material

External burnishing has shown efficacy in introducing favorable material properties in machined surfaces [68, 69, 70]. Despite this demonstrated benefit, internal roller burnishing is less well-studied in the literature due to the reduced number of applications for the process. Whilst external burnishing typically uses a single static hardened pin or roller, internal roller burnishing tooling uses multiple highly polished hardened steel rollers that sit within a metal cage at the tip of a rotating tool shaft. A Cogsdill Roll-A-Finish internal burnishing tool is shown in Figure 6.2.

Tooling is manufactured to a nominal diameter and finely adjusted by the operator before use. The precise diameter is achieved by rotation of a collet that forces the rollers outboard/inboard thus increasing/decreasing the diameter respectively in small increments. The tool is compatible with common tool-holding solutions and is loaded into the machine like a regular solid-cutting tool. During operation, the burnishing tool is fed into the drilled hole under forced rotation at a pre-determined speed as emulsion coolant is provided by the external flood coolant nozzles. Process parameters can be varied within the manufacturer's recommended range and can be optimised for a particular workpiece material and hole geometry through experimental testing. As the rollers are hardened, the tool can process hard materials including automotive steel alloys.

Figure 6.2: A Cogsdill Roll-A-Finish burnishing tool aside a drilled hole with the main components and movement axis labelled

The three main roller burnishing variables are tool diameter, burnishing speed and feed rate, with the nomenclature of d, V_c and f_n respectively. These parameters decide the rate of plastic deformation (strain rate), the tool-workpiece interaction volume and the magnitude of friction. The diameter determines the axial interference between the tool and the hole, controlling the tool-workpiece interaction volume and thus the burnishing force. Provided the applied force is sufficient to generate a contact stress larger than the yield stress of the workpiece material, asperities will be deformed. Burnishing force is well studied in the external burnishing literature, as a force dynamometer can be attached to the tool. But, this is not possible during internal burnishing as the rollers apply the force perpendicular to the tool, and a load cell would need to be placed beneath the bearing to measure axial load. Theoretically, force could be inferred from the coefficient of friction μ and torque, however, μ is unknown and cannot be assumed from external burnishing research due to differences in coolant penetration and deformation temperature. Burnishing speed, measured in meters/minute refers to the radial surface speed of the rollers as they rotate around the hole. Feed rate, measured in millimetres per revolution, describes the vertical distance traveled by the tool with each full revolution.

In material removal operations such as drilling, more aggressive machining parameters will generally reduce cycle times at the expense of increased tool wear. Manufacturers must therefore select parameters that provide an optimal trade-off for their respective application because high contact forces at the cutting edge can increase abrasive tool wear and subsequent expenditure on tooling, and long cycle times are detrimental for high-volume industries such as automotive. In burnishing, tool wear is much less of a concern, since the magnitude of deformation is comparatively much lower due to the lack of material removal and low depth of tool penetration. Therefore to simplify this research, wear of the burnishing tool was not characterised and focus was placed on the relationship between surface integrity and cycle time. In the work outlined in this chapter, an experimental machining

study was conducted to analyse the influence of internal roller burnishing on the hole quality of AISI 4140 drilled holes. Hole quality was characterised through surface finish, hardness and microstructural analyses. The approximate hole condition of the drilled holes prior to burnishing was pre-validated using drilling force data and the burnishing forces were used to assess the influence of the machining parameters on the burnishing mechanics. The work is presented as a cost-benefit analysis to determine whether improvements warranted the increased cycle time.

6.2 Experimental Method

6.2.1 Drilling Operation

The size and quality of the hole prior to burnishing is an important factor in the burnishing process. If cutting parameters, tool geometry and lubrication are kept constant and provided the fixture system is rigid, hole quality is likely to be dominated by tool wear. As drilling tools are used, the chisel edge, flank, outer corner and margin begin to progressively wear. This can significantly change the tool-material interaction and typically causes a reduction in hole quality in the form of changes to circularity, hole diameter and surface roughness. Hole diameter is particularly important as in internal roller burnishing the depth of burnish is determined by the axial interference between the burnishing tool diameter and the drilled hole diameter. Burnishing tool diameter is kept constant and as a result of tool wear and dynamic instability the drilled holes may vary in size. Sandvik Corodrill 865 tooling has a manufacturing tolerance of m7. According to ISO 286-2, the diameter of a nominal 8mm drill with an m7 tolerance can lie within a range of 7.985 to 8.000mm. At the length scale of the burnishing contact, this 15μm deviation can alter the burnishing mechanics. It is possible for the drilled hole size to decrease due to margin wear, but it is more likely that a built-up edge will accrue on the margin, increasing the effective tool diameter and subsequently the hole size. It is important to approximate hole quality prior to burnishing to ensure the measured effectiveness of the burnishing process is accurate. CMM measurement of drilled hole diameter, process monitoring and surface profilometry offer a suitable solution to validate the approximate condition of drilled holes prior to burnishing and were completed in this work.

Drilling trials were carried out to produce a workpiece of machined holes ready for burnishing. 140 holes were drilled into an AISI 4140 Steel workpiece to generate holes for burnishing. Drillings were completed on a DMU Evo 40 Linear Machining Centre using 8mm Sandvik Corodrill 865 tooling. Holes were drilled to 96mm using the manufacturer-recommended machining parameters of 71.5 m/min and 0.204 mm/rev. Cutting forces were monitored using a Kistler 9255C multi-component bed dynamometer at a sampling frequency of 10kHz. Blaser Vasco 7000 coolant was used in a through-tool configuration at an 8% coolant concentration.

Tool wear was measured intermittently every 10 holes. The surface roughness of the drilled holes was measured in 10 hole increments using a Mitutoyo SJ-210 Mobile Profilometer. The hole diameter was also measured in 20 hole increments at a depth of 40mm and 60mm using a Coordinate Measuring Machine (CMM). This was critical because tool wear can yield a reduction or increase in drilled hole diameter, depending on whether there is excessive abrasion or adhesion and this changes the axial interference and deformation depth of the burnishing tool. Circularity was also measured to ensure that the drilled holes were within industry specifications. Whilst holes were burnished at various states of wear to mitigate any tool wear effects, it was essential to capture any significant changes to allow holes with similar initial geometries to be analysed and compared. CMM analysis is expensive and time-consuming, but was deemed a necessary addition to improve the research accuracy and industrial applicability. Cutting forces, tool wear, hole diameter and surface finish data were used to pre-validate hole condition prior to burnishing to ensure that any drilling artifacts were identified and excluded from burnishing analysis.

6.2.2 Burnishing Operation

The three main internal roller burnishing parameters are the tool diameter, feed rate and burnishing speed. In this study, increasing tool diameter was used as a proxy for increasing force, since no commonly available tooling offered force control. The initial burnishing diameter was set using the manufacturer's recommended procedure. Firstly, the diameter was matched to the prepared hole diameter by lowering the tool into a drilled hole and gradually increasing the tool size until the rollers could no longer slip through the hole, similar to a ring gauging method. It was then increased by a further 10μm to operational size to encourage deformation of the hole wall as opposed to pure sliding contact. The tool manufacturers' recommended procedure was used to set the initial tool diameter, as this is the procedure that would be followed should the process be implemented in industrial crankshaft manufacture. Tool diameter was then increased for the 2nd set of holes. Tests were first conducted at this diameter and then repeated with diameter increased by a further 10μm. These two diameters were used to mitigate error due to incorrect tool setting and improve understanding of the burnishing mechanics. Burnishing speed and feed rate were selected with values at the limit of the manufacturer's recommended operating range to achieve maximum process variation. Experiment runs were organised in a full factorial design of experiments model as it utilises the minimum number of experimental runs to determine the main effects of each variable and interactions between variables. Feed rate and burnishing speed were expected to alter the burnishing mechanics by changing the rate of deformation and magnitude of friction. This was in an attempt to reach burnishing conditions with dominant mechanical and thermal effects. The combination of the two parameters also determines the process time which is an important metric in industrially applied operations. The productivity of drilling and burnishing operations can be compared by multiplying the

feed rate (mm/rev) by the spindle speed (rpm) to calculate the vertical travel speed. The impact of augmenting the burnishing parameters is outlined in Figure 6.3.

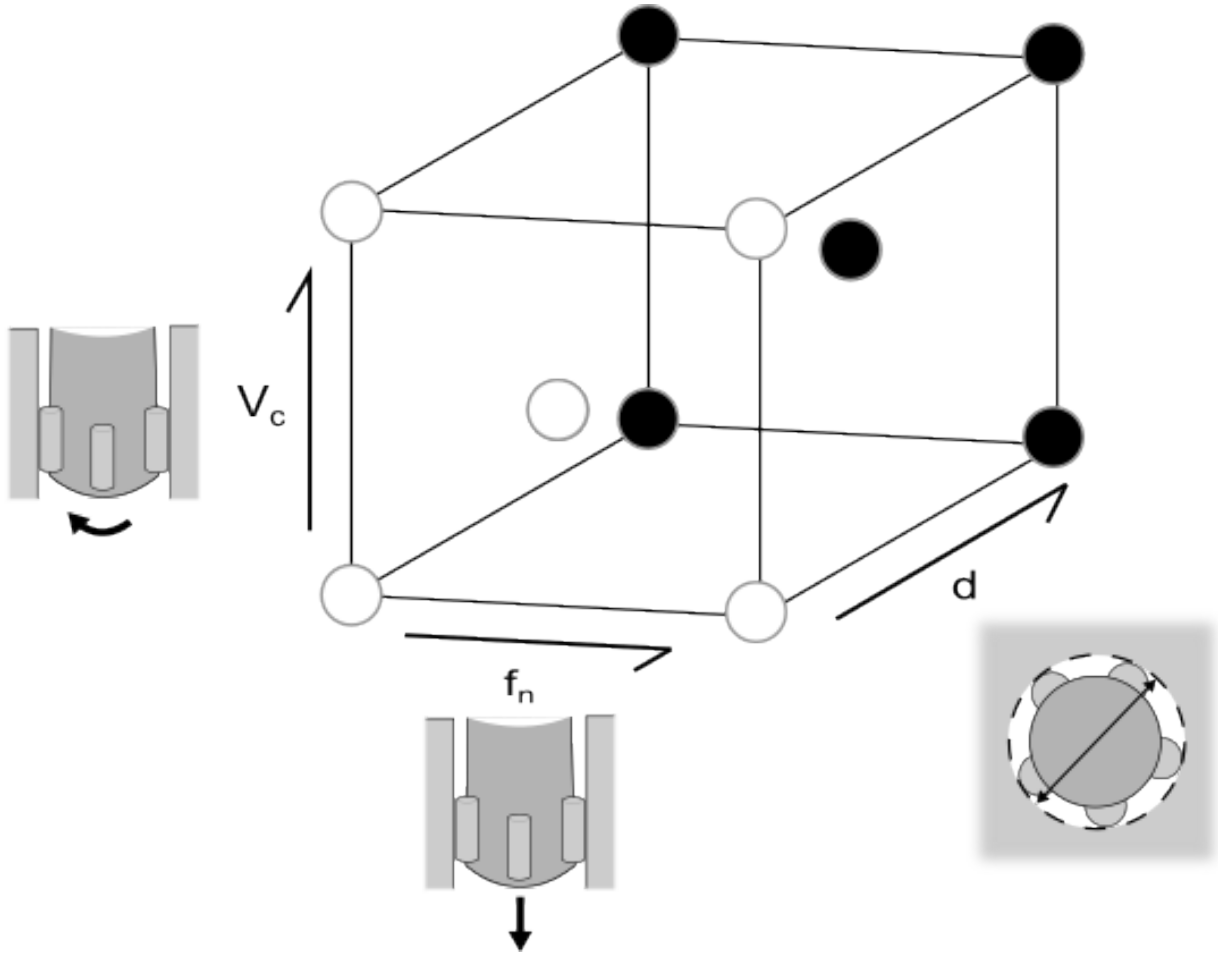

Figure 6.3: 3-Factor Full factorial experimental model outlining variation in burnishing speed, feed rate and diameter

Each hole was burnished to a depth of 48mm, which is half the depth of the drilled hole. This allowed the burnished and drilled portions of the same hole to be compared. This is important as it enables performance to be expressed as a percentage improvement. Seven repeats were taken for each parameter set and diameter combination. These repeats were conducted on groups of holes drilled at different magnitudes of tool wear. For example, parameter set 1, diameter 1 was used to burnish the 4th, 24th, 44th, 64th, 84th, 104th and 124th drilled holes. This ensured the experimentation closely represented industrial machining, where holes are drilled with a cutting tool in multiple wear states. This is outlined in Figure 6.4.

Dynamometer data was captured during burnishing to verify that a force was generated and the cutting tool was engaging sufficiently to deform the surface. No material is removed during the operation and it is relatively quiet, so it is difficult to validate that deformation has occurred on-machine without force dynamometry. The data collection rate for the Dy-

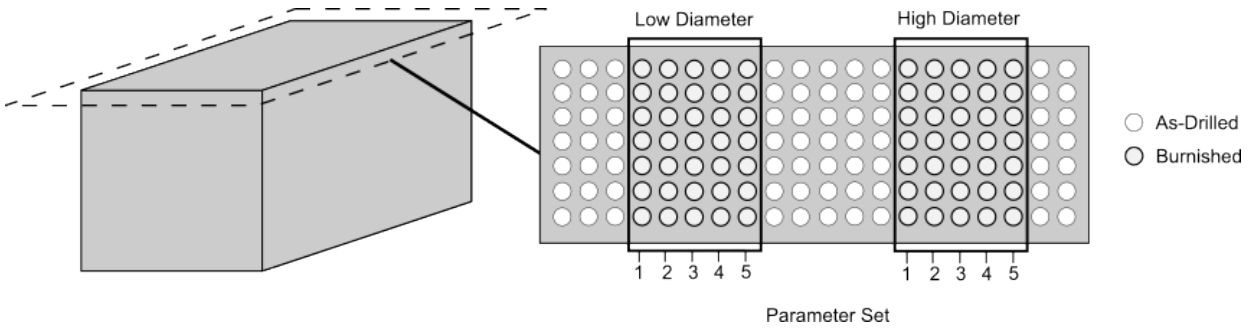

Figure 6.4: Schematic outlining the location of drilled and burnished holes and the repeats

namometer was 20kHz, providing a spatial resolution of 0.5μm in the axial direction and 50μm in the radial direction. In an as-rolled state, 4140 steel typically has a ferritic-pearlitic microstructure with a grain size of $>$ 9 ASTM ($<$ 16μm) according to DIN EN 10247:2007 [71]. This equates to an exposed grain area of between 178 and 366 μm^2 assuming an equiaxed grain geometry, which is larger than the sensor resolution. The low ratio of spatial resolution to expected grain size offers high resolution in the axial direction, allowing good expected differentiation of grain effects. A dwell time of 60 seconds was programmed between hole sets to allow the tool to cool, reducing the effects of thermal expansion. The tool was also cleaned with compressed air during this period to remove any debris and contamination that may affect the contact, which provided further cooling. Blaser Vasco 7000 emulsion coolant was supplied via external flood application at 8% coolant concentration. Whilst through-tool coolant may have been more effective, the tooling geometry prevented through-tool application.

6.2.3 Surface Inspection

Surface inspection was conducted on the drilled and burnished holes to quantify the improvement of surface finish as a result of the burnishing operation. To achieve this, holes were sectioned open and inspected with a Bruker Alicona InfiniteFocus SL optical measurement system. The system generates a 3D surface topography by capturing 2D images in layers of successive depths which are then joined to form a 3D surface topography, from which surface roughness profile measurements can be extracted. A 10μm wide, 4mm length profile was taken as per the recommendations from Section 5.4.1. Measurements were taken for all parameter sets and three repeats were conducted at groups 1, 3 and 6, representing holes that were burnished after being drilled at varying levels of tool wear. All holes were inspected at depths of 30mm and 60mm to capture both the burnished and drilled region. Five randomly selected as-drilled holes were also inspected to validate the consistency of the drilled hole condition. The maximum profile height R_z, arithmetic mean roughness, R_a were chosen to compare the surface finish of the drilled holes. They provide a comprehensive picture of changes in the surface profile introduced by machining, as outlined in Section 5.4.1.

6.2.4 Sub-Surface Characterisation

To characterise microstructural evolution in the near surface due to burnishing, small samples were extracted from the machined workpiece in two cross-section orientations, a radial view and an axial view as displayed in Figure 6.5. An axial view is advantageous since a single micrograph exposes a depth profile from which multiple measurements can be taken. But, the exposed width of the plastically deformed layer (PDL) is dependent upon the accuracy of the sectioning procedure and the quantity of material removed during preparation. This is important since, as demonstrated in Chapter 3, the depth of the machining-affected layer is a key surface integrity metric. A significant quantity of material is removed during grinding and polishing. Sectioning off-center further amplifies this issue. Although an axial view may be useful for identifying microstructural variation with depth, it is an unreliable method of comparing holes machined with different processes and parameters. Although the radial view only exposes a single layer of grains and requires multiple samples to be generated to conduct repeats, it is not sensitive to material removal. It was decided from this point forward that radial views would be used to compare machined microstructures and axial views would only be examined if there was expected to be a large change in cutting mechanics with depth, such as when an erroneous change in force is detected.

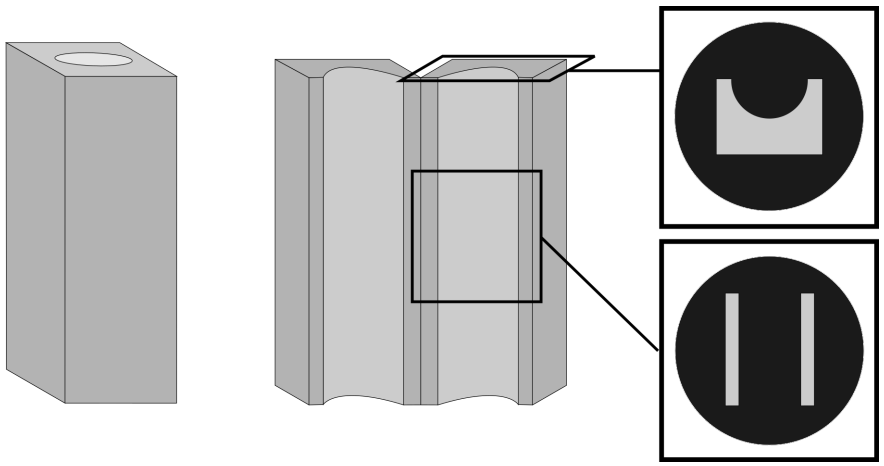

Figure 6.5: Sectioning procedure to produce two cross-sections from a machined hole, a radial view (upper) and an axial view (lower)

Due to the large workpiece size, which exceeded the limits of bench-top sectioning equipment, the workpiece was first sectioned with a band-saw and then reduced to the final analysis size with a Buehler Isomet 5000 and silicon carbide cut-off wheel. The small hole samples were then mounted in conductive bakelite using a Buehler SimpliMet 3000 hot mounting press and polished using the preparation procedure outlined in Section 4.4. For the grain structure to be visible with light microscopy the surface required etching. To achieve this, samples were chemically etched with 2% Nital reagent in 10s increments immediately after polishing. The chemical reagent preferentially reacts with the more chemically reactive grain boundaries

and introduces a textured surface topography that is visible under light. Images were taken with a Nikon LV150N upright metallurgical microscope at various magnifications to identify alterations to the near-surface microstructure as a result of the burnishing operation. Near-surface deformation was difficult to characterise under light optical microscopy (LOM) and hardness testing was subsequently conducted in an attempt to quantify the depth of the plastically deformed layer and the extent of deformation in the near-surface.

To establish the evolution in hardness below the hole wall surface, cross-sectional samples were analysed using a Nanotest Vantage Nanoindentation system. Previous work in Chapter 5 had demonstrated that microhardness analysis was not sufficient to differentiate thin regions of deformation. Testing was conducted under a maximum load of 10mN. Indents were taken in 10μm increments of increasing depth from the machined surface, beginning at 5μm. The size of the indent and subsequently the hardness were calculated using the indenter travel recorded by the calibrated drives and the known Berkovich indenter tip geometry. A series of load cycles is shown in Figure 6.6.

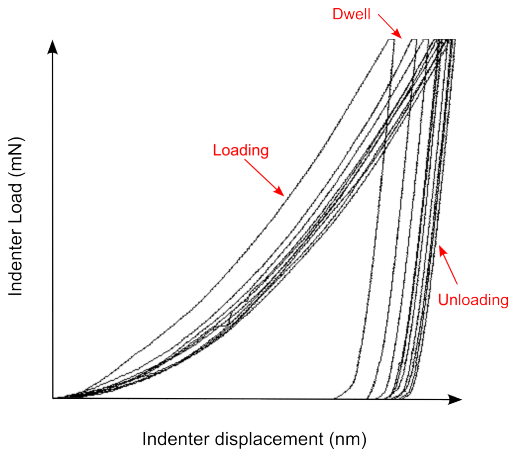

Figure 6.6: Example load cycles applied to the indenter tip during a series of nanoindentation hardness tests

6.3 Results

6.3.1 Drilling

The graph in Figure 6.7 shows the evolution of the cutting force across the entire hole set, as measured by the dynamometer mounted below the workpiece. Force was captured for every machined hole and post-processed in MATLAB to remove sensor drift effects, segment the in-cut portion and calculate the average force across the entire hole. Thrust force, F_z rose by 5% from an average of 930N over the first 10 holes, to 1010N over the final 10 holes. Five sets of force data were randomly selected and manually inspected to ensure that there was no evidence of inefficient cutting, such as excessive vibration. All followed the expected pattern of sharp increase in the cutting force at initial contact followed by a steady region once the

cutting tool had fully engaged. No anomalous holes with large force spikes or gradients were identified in the cutting force data.

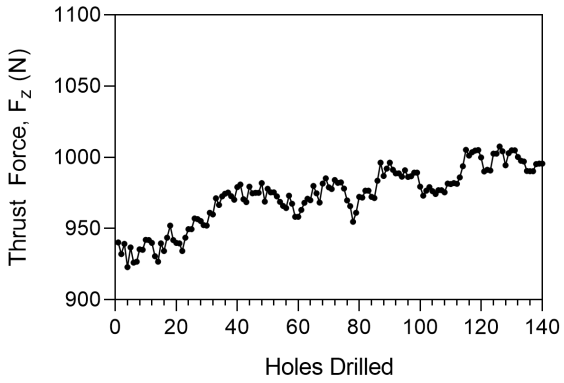

Figure 6.7: The evolution of vertical thrust force during drilling with increasing number of holes drilled for a single tool

The cutting tool was routinely removed from the machine tool and inspected under an optical microscope. It was of importance to identify signs of blunting of the chisel edge and notch formation at the cutting edges, as these can greatly affect cutting efficiency. Images of the cutting edges were captured at a known zoom and scale and reviewed after the test to calculate and record the average wear across the cutting edges. After machining, the workpiece was examined with a CMM system. The diameter and circularity of every 10th hole was measured in 10mm increments between 10mm and 70mm hole depth. The progression of tool wear with holes drilled is shown in Figure 6.8 alongside the diameter of the holes measured with the CMM system.

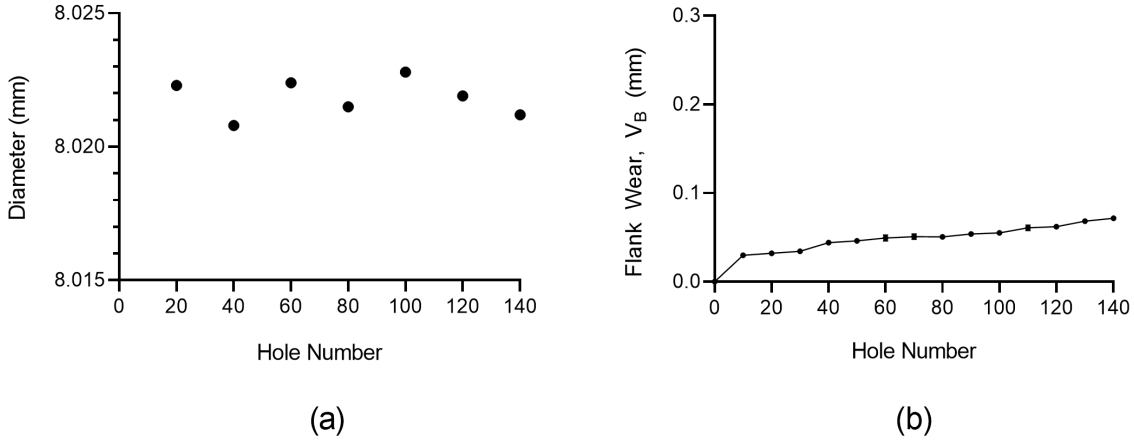

Figure 6.8: Change in (a) Measured hole diameter and (b) Tool flank wear over the hole set

These two results were compared to identify whether the diameter of the tool varied significantly as the tool was worn, either through reduced margin size or a built-up edge. Flank

wear, V_B increased rapidly over the first 10 holes before returning to a steadier wear rate for the remaining 130, reaching an average of 0.08mm across both cutting edges after the final drilled hole. This is still well within the acceptable flank wear limit of 0.3mm, so all holes were deemed suitable for burnishing if required. Due to rapid initial wear, the first 10 holes were excluded from further analyses, and this is consistent with the recommendations of Section 5.2. The CMM measured diameter varied across a range of 20μm, with no visible trend with the number of holes drilled. The circularity of the hole was also measured and the average across the five measurement depths is shown in Figure 6.9 together with a graphical representation of a hole specimen.

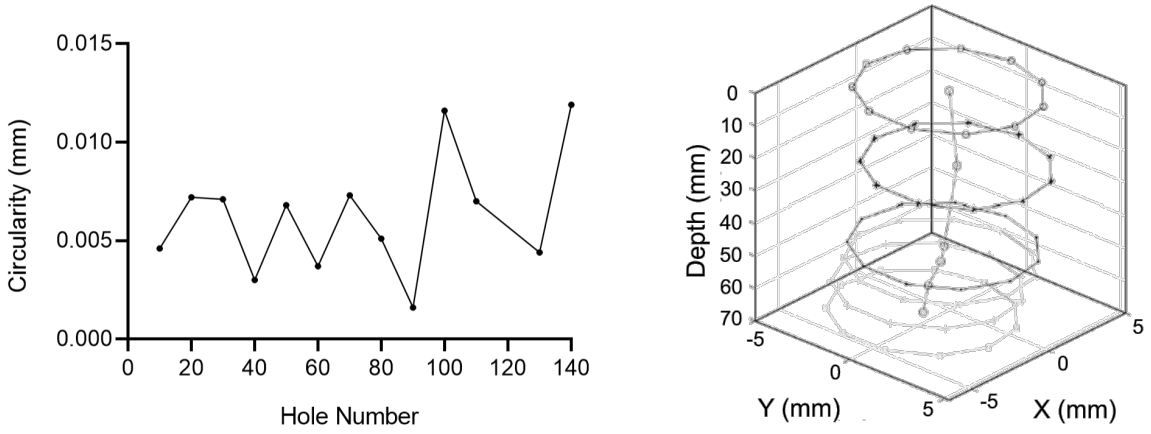

Figure 6.9: Change in circularity with increasing number of holes drilled and a reconstructed hole geometry based on geometric data obtained through CMM analysis

Poor hole circularity can theoretically reduce the stability of the burnishing process by causing a periodic increase and decrease in effective hole size. Since the burnishing tool diameter is fixed, an increase in the diameter of the hole causes a decrease in axial interference and vice versa. This causes a cyclic change in force which inhibits the operation's effectiveness and at worst may lead to vibration. Circularity is also influenced by any acircular rotation of the tool, termed spindle runout. This is the inaccuracy in the rotation of the spindle that causes it to rotate off its intended ideal axis. Runout was measured at 12μm using a dial gauge immediately prior to machining. The run-out specification is a maximum of 20μm. Since circularity is only marginally larger than the measured spindle runout and within the runout tolerance, the results were deemed acceptable. All inspections from this point forward were conducted on the as-drilled region of sectioned hole specimens after the burnishing operation had been completed.

The surface of five randomly selected drilled holes were inspected with a Bruker Alicona InfiniteFocus SL Optical measurement system. The arithmetic mean roughness, R_a, root mean square deviation, R_q and maximum profile height, R_z of the imaged surface topographies were compared, with the results displayed in Figure 6.10.

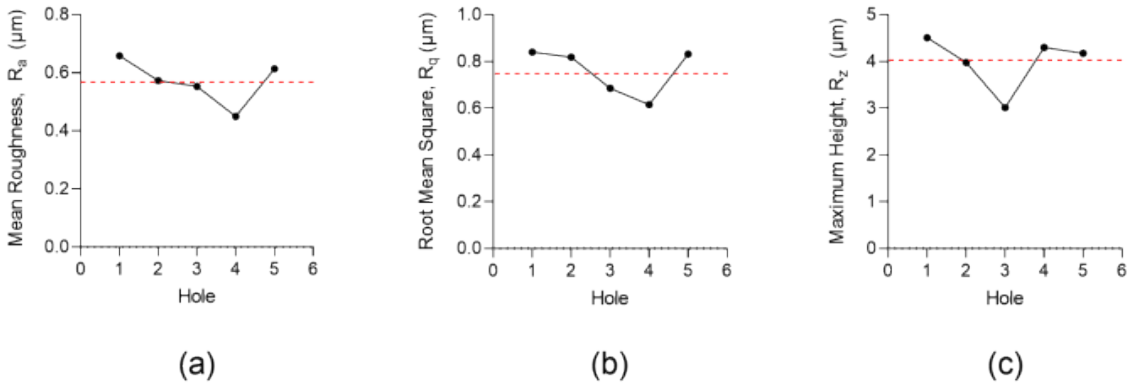

Figure 6.10: Measured (a) R_a, (b) R_q and (c) R_z surface roughness parameters from drilled hole surfaces

The mean value of R_a was 0.56μm and results varied by $\pm$33% across the five holes with an outlying low value of 0.45μm at hole four. R_q varied by $\pm$25% around a mean of 0.75μm. Again, hole four had the lowest measured value of 0.62μm. R_z varied by $\pm$19% around a mean of 4μm but this time hole three presented the lowest roughness value. R_z is most sensitive to surface scratches and pile-up, which suggests that hole three contained smaller and/or fewer scratches. All holes were within the acceptable manufacturing tolerances for crankshaft drilling as set by the industrial project sponsor, however, there was clear variation between the five holes. For example, the difference between hole one and hole four was particularly large and it is likely that burnishing of these two holes would yield a different final profile. Similarly, the surface scratches evident in hole three are smaller than those in hole one and may be completely removed following burnishing. Comparison of only the final burnished state of these two holes would ignore any discrepancy in drilled condition. Due to the variation between holes that is evidenced here, it was decided that all burnished holes would be compared to their reference drilled state by measuring the non-burnished portion of the same hole. This method allows a relative surface improvement to be calculated that takes into account the quality of the drilled hole.

6.3.2 Burnishing Force

During burnishing, the contact forces at the tool-workpiece interface were captured in 3-axes by a force dynamometer mounted between the workpiece and the machine bed. This data was post-processed to calculate the average force across the entire hole depth for each burnishing operation. A linear regression model was then computed from the average force data which interpolates the burnishing force response across all combinations of parameters within the experimental bounds using a Partial Least Squares (PLS) model. PLS was selected arbitrarily as the regression model. The model validity was 90%, which confirms the model fits well with the experimental data within the experimental bounds. Therefore,

conclusions surrounding the relationship between burnishing parameters and force can be made with reasonable accuracy. However, this conclusion is limited to parameters within the experimental bounds. If prediction of forces was required in the future, the model would need to be validated against further experimental data, beyond the training dataset. The presence of center points in the experiment matrix allowed curvature to be examined, which describes the non-linear response behavior within the experimental bounds. Contour plots of the influence of burnishing parameters on the burnishing force at the two separate tool diameters are presented in Figure 6.11.

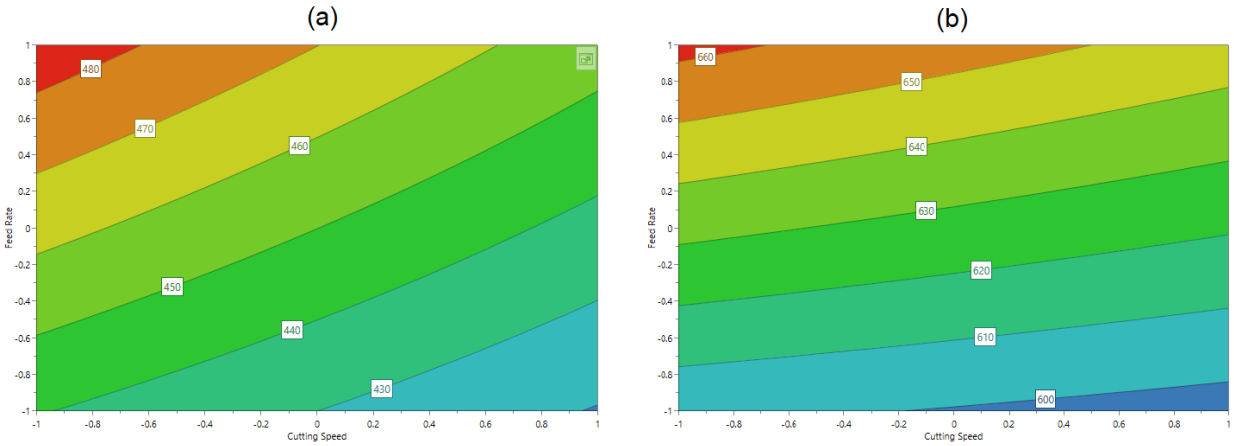

Figure 6.11: Contour plot of the measured burnishing forces for the (a) small tool diameter and (b) large tool diameter

The burnishing forces increased with the diameter of the tool for all parameters. Forces increased with feed rate and decreased with burnishing speed at both tool diameters. However, the gradient of the force-parameter relationships changed with the diameter of the tool. At the smaller tool diameter, the force increased from 545N at the least aggressive parameter set, to 610N at the most aggressive, a change of approximately 12%. At a low feed rate of 0.3048 mm/revolution, the force decreased from 560N at a burnishing speed of 32.67 m/min to 545N at 92.99 m/min. As the feed rate increased and the tool moved vertically more with each revolution, the contact forces became more sensitive to burnishing speed. At 0.3556 mm/revolution, the decrease was from 610N to 570N. This is a larger decrease in both absolute and percentage terms. In contrast, as the burnishing speed increased, the forces became less sensitive to the feed rate. At the higher tool diameter, the force differed by a maximum of 11% between 765 and 850 across the parameter range. Unlike the small diameter, at a low feed rate, the force was almost entirely insensitive to burnishing speed. Increasing the burnishing speed from 32.67 m/min to 92.99 m/min yielded a change of only 5N. At the maximum feed rate, when the tool was deforming the largest amount of material with each revolution, the force changed by 30N across the range of burnishing speeds. At high burnishing speeds, forces were less sensitive to feed rate, similar to the small-diameter operation.

All force profiles contained a sharp increase in force as the tool came into contact with the workpiece, which began to level off and stabilised after the initial seconds of burnishing. The time it took for the force to stabilise for each hole was well correlated with the vertical feed rate of the tool. All holes stabilised after the tool had traveled a vertical distance of approximately 8mm, which is the same length as the burnishing tool rollers.

6.3.3 Surface Integrity

6.3.3.1 Surface Finish

The surface topography of the burnished surfaces was captured to assess the variation in the final machined condition within the operating range. Figure 6.12 summarises the change in the mean arithmetic roughness, R_a and ten-point mean peak to valley height, R_z of the burnished surfaces with varied rotational speed and feed rate.

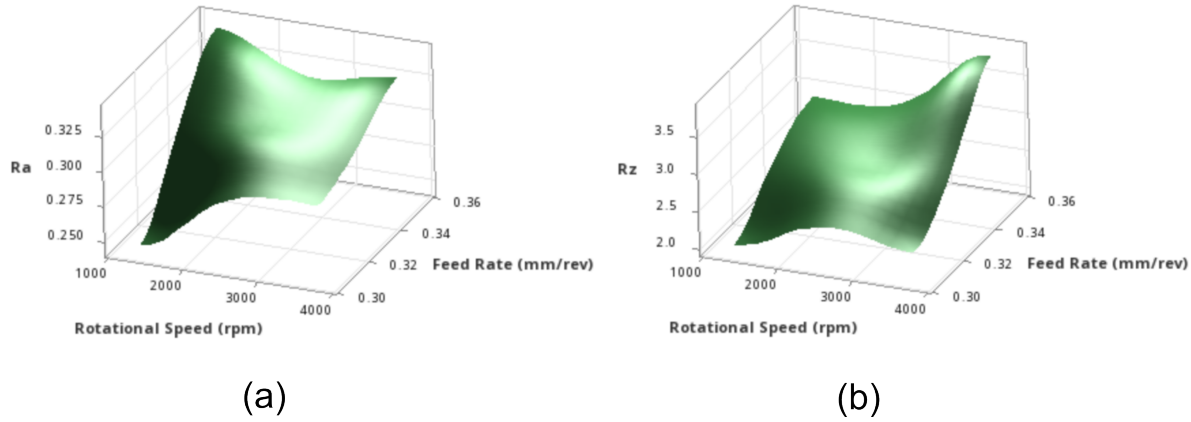

Figure 6.12: Response surface plot of the mean (a) R_a and (b) R_z values for the burnished surfaces

Both roughness parameters were negatively affected by an increase in feed rate at all rotational speeds. An increase in rotational speed had a negative effect on R_a at the low feed rate and a positive effect at the high feed rate. R_z was negatively affected by increased rotational speed at all feed rates. Following the results of Section 6.3.1, the as-drilled portions of the same holes were also measured to assess the influence of the drilled condition on the performance burnishing operation. The variability in R_z for the drilled surfaces was large, with a minimum and maximum across the dataset of 2.73μm and 6.81μm respectively. R_a on the other hand was more consistent, ranging from 0.38μm to 0.54μm. Importantly, all drilled surfaces were within the tolerance set by the manufacturer of the burnishing tool.

The previous results demonstrate the main effects of modulating rotational speed and feed rate within the operating parameters, but from an industrial perspective, the resultant cycle time for the machining operation is key. It is important to consider the trade-off between the cycle time and surface quality, since increased cycle times give rise to higher manufacturing

costs. To this end, R_a was compared in terms of productivity, expressed by the vertical feed rate of the operation (Figure 6.13). R_z was not considered due to the large variability in the as-drilled surfaces. To account for the minor variability in R_a for the as-drilled surfaces, the relative change in surface finish after burnishing was also calculated as a percentage improvement.

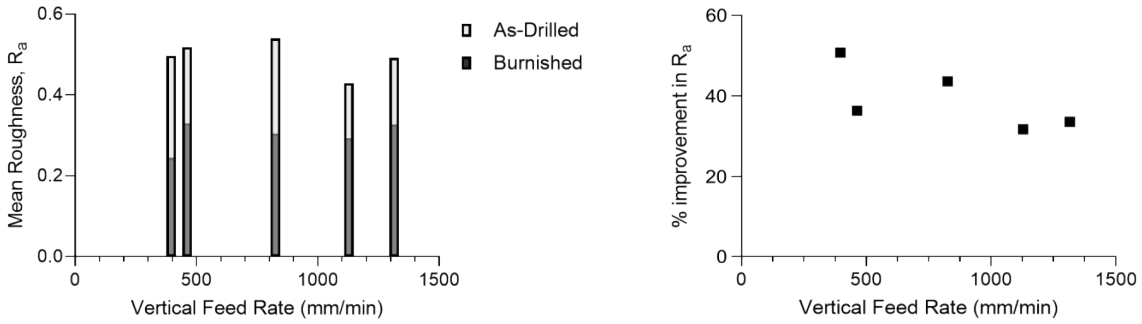

Figure 6.13: Absolute and percentage change in R_a following burnishing

Burnishing consistently provided a reduction in mean profile roughness compared to the as-drilled condition, regardless of the parameter set. The reduction in roughness varied between 27% and 50%, with a weak negative correlation between improvement and vertical feed rate.

6.3.3.2 Sub-Surface Properties

A machine-affected layer was generated beneath the surface by both the drilling and the burnishing processes. This was first characterised through light optical microscopy (LOM). Example as-drilled and burnished optical micrographs are shown in Figure 6.14. The microstructure of the drilled samples exhibits a band of refined and sheared grains in the near-surface region that extends to a depth of around 20μm, giving the appearance of swept grains. Deformed grains are also sheared in the direction of rotation, with apparent shear strain decreasing progressively with depth. Beyond 20μm the grains are uniform in size and consist of randomly distributed pearlite within a ferrite matrix. All samples examined demonstrate a consistent sub-surface grain structure and there was no evidence of white-layer formation.

As seen in Figure 6.15, the burnished samples initially exhibited a darker region near the surface of the micrograph compared to the bulk microstructure, despite the fact that the exposure time was identical throughout the sample. Strangely, the grain structure was still visible beneath and appeared to show single grains across both the dark and light regions. Repeats were performed by repolishing and etching the same surface, and a dark region was no longer visible. The preparation procedure was updated to reduce the etching time by 5 seconds to prevent over-etching of the burnished region.

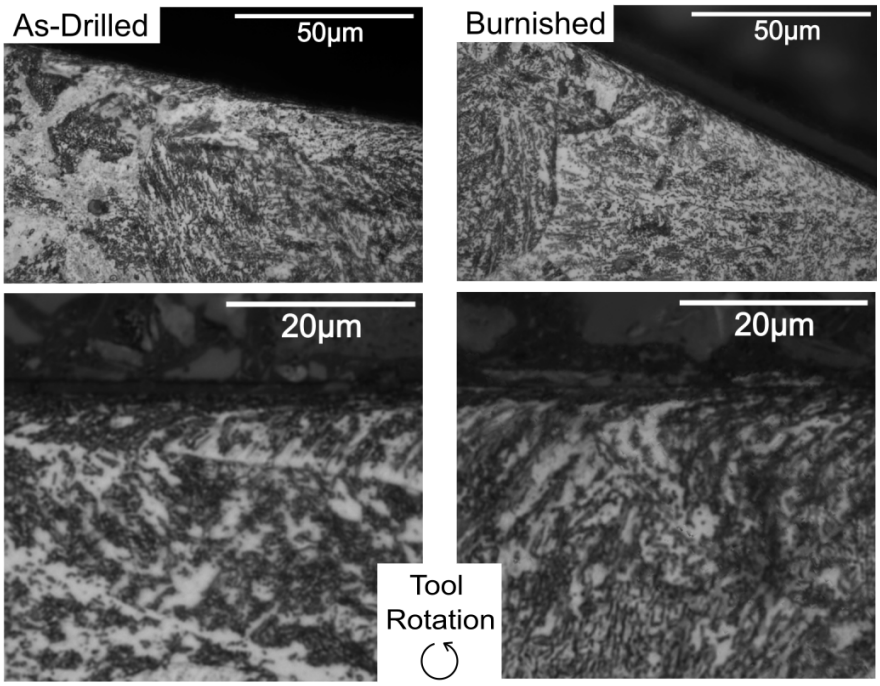

Figure 6.14: Optical micrographs of etched specimens taken from as-drilled and burnished hole specimens

It was not possible to identify significant variation in deformed microstructure with varying burnishing parameters. Scanning Electron Microscopy (SEM) was performed on the samples in both an etched and non-etched state, but it was not possible to identify further information than what was gathered from LOM. To provide further microstructural information, nanohardness testing was conducted on three prepared specimens: as-drilled, burnished at low productivity and burnished at high productivity. Low and high productivity represent the operations with the minimum and maximum vertical tool speed respectively. These were chosen because cycle times are key in automotive machining operations. Three indentation profiles were generated for each specimen at three locations. These locations were a sufficient distance apart to negate proximity hardness effects. The low-load of a nanohardness test theoretically allows small machining-affected layers such as those seen here to be resolved. Nanohardness testing was conducted in increments of 10μm, beginning at 5μm from the surface. Results are displayed in Figure 6.16 alongside the specification of the machining cycles, including the predicted cycle time to burnish a 96mm long hole.

The as-drilled surface exhibited a sharp increase over baseline hardness at 5μm depth that diminished steadily towards 30μm with good repeatability. From 30μm the hardness remained low but with increased variability between repeats. The burnished surfaces both demonstrated an enhanced hardness at 5μm that dropped sharply to below the drilled hardness from 15-25μm before recovering and emulating the as-drilled profile. The change in hardness profile between the two burnishing parameter sets was small compared to the large change in cycle time.

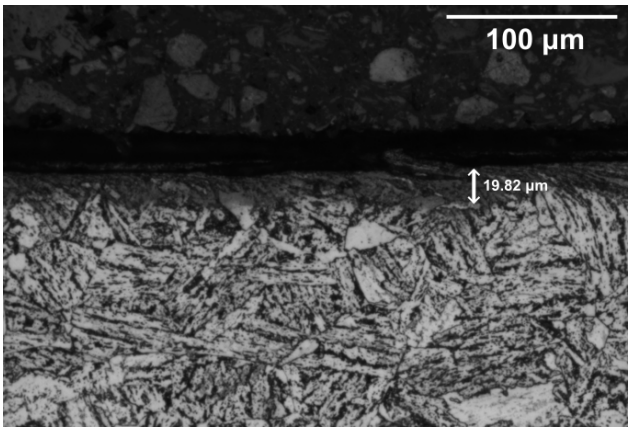

Figure 6.15: Optical micrograph of a burnished hole sample at two magnifications, with evidence of a dark region at the near-surface

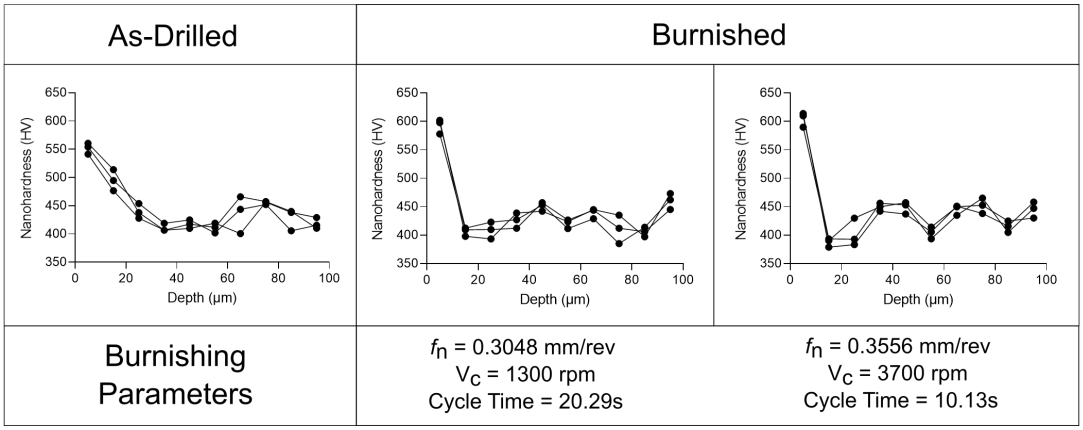

Figure 6.16: Nanohardness profiles taken from three 96mm hole specimens in three different machining conditions

For a 96mm hole, the approximate cycle time for the drilling operation is 29s when operating at the mid-range of parameters with a spindle speed of 2845 rpm and feed rate of 0.204 mm/rev. This includes 10s of cutting and a 19s tool retraction. A subsequent burnishing cycle for the same hole takes 13 seconds at the mid-range of 2500rpm and 0.3302 mm/rev. This includes a 6 second tool retraction time for a combined 45% increase in cycle time for the generation of the oil hole. This may increase further if a slow retraction time is required. The operating range is much larger for rotational speed (1300-3700 rpm) than for feed rate (0.3048/0.3556 mm/rev), therefore cycle time is most sensitive to rotational speed. Additional time is also required for tool changes. If surface integrity improvements cannot be obtained without an acceptable cost to productivity, the process is unlikely to be implemented in industrial manufacturing.

6.4 Discussion

6.4.1 Drilling

The drilling operation was monitored with force dynamometry and analysed with surface inspection techniques to identify erroneous holes and pre-validate hole condition prior to burnishing. Cutting forces rose 5% across the 140-hole set and tool flank wear reached 0.08mm over the same period. This is well within the 0.3mm usable limit of 0.3mm of the tool, and the increase in force was expected due to steady degradation of the cutting edge. The increased propensity for built-up edge (BUE) formation due to higher tool temperatures as the tool wears is always a concern for manufacturers. The diameter of the hole drilled measured with a CMM varied by a maximum of 20μm, which was only marginally higher than the measured tool runout of 12μm. BUE formation generally leads to an increase in hole size and the absence of a large change in hole diameter suggests that BUE was not a major concern. BUE effects can be counteracted by tool margin wear, but 3D surface topography scans of the tool margin both before and after machining only revealed minor surface degradation. There was also no evidence of a correlation between cutting force and hole diameter. This suggests that the rise in cutting forces was not due to the presence of a built-up edge at the cutting tool margin, since this would increase the effective tool diameter and coefficient of friction and increase the force required to rotate the tool. The circularity of the hole was consistently below the maximum run-out specification for this tooling. This is important, since an acircular drilled hole geometry would place varied loads at different points around the circumference of the burnishing tool. At a macro-level, this could cause vibrations and at a micro level it could lead to differing depths of deformation which may impact results. Since forces remained stable with no rapid increases in consecutive holes and surface finish was consistent, it was assumed that the hole condition of all holes prior to burnishing was consistent. This is consistent with prior research that saw a positive correlation between thrust force and surface roughness across various tool geometries and coolant methodologies [72]. The measured surface hardness of the as-drilled hole was much higher than expected and concentrated to the near-surface with a narrow machining-affected layer. Hardness also reduced steadily toward the core microstructure. High surface hardness is attributed to the double-margin design used for the Sandvik Corodrill 865 tool, which increases the number of contact points between the tool and hole wall and thus the number of tool passes.

6.4.2 Burnishing

In this section, the force profiles are initially examined to better understand the critical contact between the tool and the hole wall. Subsequently, the various surface integrity results are evaluated to determine if burnishing has significantly improved the workpiece

properties. Any beneficial effects are weighed against the extended cycle time to gauge the feasibility of incorporating burnishing into the crankshaft manufacturing process.

6.4.2.1 Tool Diameter

In burnishing operations, force is an important performance indicator and is often considered the primary determinant in burnishing research. In internal roller burnishing, the applied force is governed by the diameter of the tool. The burnishing force commonly exhibits a parabolic relationship with surface properties, in which increasing the force generates increasingly favourable properties until an optimum point, where properties begin to deteriorate [73]. Low forces are indicative of poor tool engagement, resulting in minimal deformation, leading to suboptimal surface finish and near-surface microstructural refinement. This lack of engagement can even precipitate vibrations due to intermittent and unstable interactions between the tool and material irregularities. Conversely, an excessive force may cause the tool to penetrate beyond the asperities, leading to grooving, or in extreme cases flaking and removal of surface material, which diminishes hardness. Ensuring that the diameter remained within this range was vital. Across all parameters, a significant rise in burnishing force was observed with an increase in tool diameter. As the tool engages a larger volume of material, it generates a larger shear zone and more intense work hardening. When operating at the larger tool diameter, there was a noticeable enhancement in surface finish over the initial drilled state, with no signs of surface grooves or marring. Hence, the level of burnish was considered satisfactory. Further experimentation surrounding the tool diameter was deemed beyond the scope of this research. Further discussions are focused on the holes processed using the larger diameter tool.

6.4.2.2 Bearing Contact and Lubrication

All of the burnishing force profiles exhibited a reducing positive gradient over the first few hundredths of a second followed by an immediate transition to a constant stabilised force. The distance of tool travel during the ramped portion was calculated considering the vertical speed of the tool and was found to be consistent for all burnishing parameters. The calculated distance of travel was approximately equal to the full length of a single roller bearing within the burnishing tool. This confirmed that the entire bearing made contact with the hole wall. The reduction in the force gradient as more of the bearing surface came into contact suggests that most contact forces are concentrated in the lower portion of the bearing. This could be explained by the slight back-taper on the bearing that reduces the diameter toward the top. Due to the permanent contact between the bearing and hole wall, it is difficult for metalworking fluid to penetrate into the contact zone, except when the surface is pre-lubricated and fluid is entrained under sliding. This is similar to the tool margin and wall contact during drilling. In drilling, cutting fluid travels out of the tool-end at high speed before impacting the bottom of the hole and being directed back up the outside of the tool.

The circular motion of the tool drags the fluid upwards, lubricating the contact surfaces and removing heat from the hole. Burnishing relies on the flood method of fluid delivery, whereby a nozzle attached to the turret is directed at the hole (Figure 6.17). While the fluid reaches the hole at relatively high pressure, the circular motion of the tool acts against the direction of travel of the coolant, forcing it back out of the hole and away from the machining zone. Any fluid that does pass the burnishing tool travels straight out of the hole without interruption. There is no fluid return and therefore no back-pressure. Cutting fluid is far less effective at extracting heat and lubricating the contact surfaces in burnishing than in drilling. This may be worsened by increased rotational speed, leading to higher contact temperatures and a reduced ability to extract heat from the enclosed hole. It would be beneficial to measure the flow of coolant around the tool at various rotational speeds, but unfortunately, this was not completed at the time of testing. There was no evidence of a changed parametric relationship between hole quality and speed between lubricated and dry conditions, which suggests that at the speeds used coolant flow was not impacted by speed. Hole quality has been shown to improve when burnishing with lubricant rather than dry [74], which supports the observations here that coolant is effective.

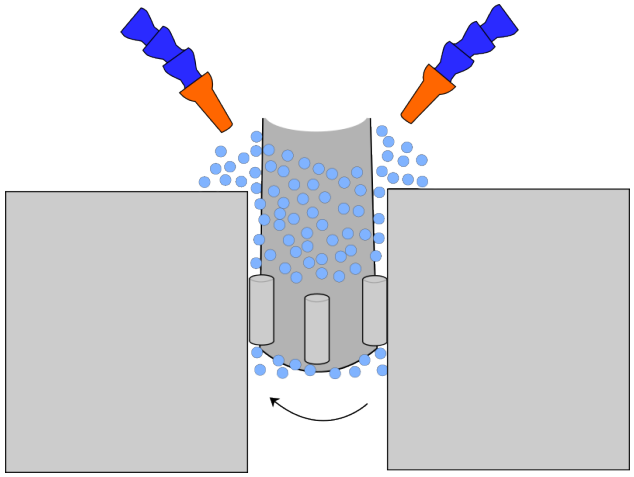

Figure 6.17: Schematic demonstrating the restricted delivery of metalworking fluid to the contact zone as a result of the permanent workpiece contact

6.4.2.3 Surface Quality

It is clear from the surface topography analysis that modulation of burnishing parameters did not produce significant impacts on surface roughness. It was initially thought that decreasing the feed rate would improve surface finish due to the reduced spacing between passes, but this did not appear to be the case. Repeated passes of the burnishing tool have been shown to improve the measured surface roughness during external burnishing. Rao [73] identified a negative logarithmic relationship between number of passes and surface finish. It is hypothesised that this is caused by repeated deformation of surface irregularities

and plastic flow ahead of the bearing. Gomez-gras et al. [75] conclude that when the lateral pass-spacing, as governed by the feed rate, coincides with the distance between the pile-up and valley of the previous pass, the surface roughness improvement is maximised. Any decrease beyond this lateral pass-spacing is unlikely to be beneficial and will lead to decreased productivity. There is a large difference in tool geometry between the external burnishing process referenced in the studies and the internal roller burnishing process used here. External burnishing uses a single spherical bearing with a single point contact on the surface, so as the tool feeds across the workpiece, the contact point moves introducing a ridge on the workpiece surface. As feed rate increases, the distance between these ridges increases, generating an undulating surface topography that increases the measured surface roughness. On the other hand, internal burnishing uses a series of long cylindrical rollers that pass over the same point on the hole wall multiple times, preventing the formation of any feed ridges and reducing the impact of feed rate on surface roughness. Furthermore, as the internal burnishing tool used here operates with multiple rollers, the lateral pass spacing is significantly reduced compared to external burnishing operations and the number of passes is much higher. Even at the highest feed rate in this study, the number of passes still far exceeds the number seen in other studies [73, 75]. This explains why feed rate was almost inconsequential for surface finish. Rotational speed had a slightly greater effect, with increased speed leading to a reduction in mean arithmetic roughness R_{a}, but still limited impact on the peak to valley height R_{z}. Increased rotational speeds generate more heat, which can aid the plastic flow of asperities around the bearing, thus reducing R_{a}. But again, as the number of passes is so high with this tool, even at low burnishing speeds the contact temperatures are likely to be high enough to encourage deformation by the final pass. This is supported by the weak influence of speed on the measured forces. Since R_{z} is heavily dependent on the depth of surface scratches, any impact of reduced flow stress may have been limited by the diameter of the tool. Given the limited effect of surface finish on fatigue life within the order of values seen here, it is not recommended to consider surface roughness as a key variable when selecting parameters. Instead, focus should be placed on the evolution of the surface and subsurface microstructure.

6.4.2.4 Microstructural Evolution

Light optical microscopy (LOM) is commonly used in material science as a first step toward material characterisation [76, 77]. Specimens were initially examined for features that could be detrimental to performance, such as white etching layer (WEL). There was no evidence of white layer formation in either the drilled or burnished samples. This is positive from a performance perspective and also provides evidence that near-surface temperatures did not exceed the austenisation temperature of the material and deformation in the hole wall was moderate. During initial analysis, a dark region was identified in the near surface of burnished samples. The initial presence of a dark region within the near-surface

microstructure of some specimens suggested there was large microstructural alteration. A similar phenomenon has been identified in the near-surface microstructure of rolling contact fatigue (RCF) specimens where, under high-cycle repeated contact, dense bands of carbide-like structures form at the contact surface [78]. It is hypothesised that these carbides form due to dislocation rearrangement during plastic deformation, which gives rise to the transportation of carbides to the grain edges, giving a thick appearance. Given the number of passes of the burnishing tool was in the region of 10^2 rather than the 10^8 passes experienced by the RCF specimens, it is unlikely that this mechanism had occured here, unless the bands formed almost instantly under deformation. Since the dark regions disappeared upon re-polishing and etching, they may have been an artefact of an excessive initial etch at the edge. Heavily deformed regions may be more prone to over-etching due to the increased density of grain and sub-grain boundaries. As the dark region was only present on a few burnished specimens and no drilled specimens, over-etching of the more deformed region was assumed to be the cause. The etching exposure time was reduced by 10 seconds and the artefact disappeared without a significant impact to the visibility of the grain structure.

If it is assumed that the aforementioned dark layer was a preparation artifact, there was no discernible visible change in microstructure between the drilled and burnished specimens. Visible grain refinement following drilling was minimal, which is a testament to the high quality of modern drilling tool design. LOM analysis of drilled AISI 304 steel samples has identified similarly small regions of local plastic deformation [79]. Given the small size of deformed layer following burnishing, it is not surprising that optical characterisation was not successful. Localised plastic deformation may also extend beyond the visibly deformed grains. Metallographic examination of externally burnished C45 steel revealed a densely deformed surface layer that was approximately 300 μm thick, but hardness measurements revealed a further deeper subsurface region of minor deformation which continued to a total depth of 700 μm [80]. This suggests that LOM alone is not suitable for internal roller burnishing research.

Although the plastically deformed layers in the drilled and burnished samples were small, the resolution of the nanohardness measurements allowed the variation in hardness across the machining affected layers to be seen. There was evidence of sharp changes in hardness between repeats at the same depth. Due to the small indent size, results could be influenced by small-scale microstructural changes caused by indenting regions of ferrite and pearlite (Figure 6.18). Pearlite is harder and contains a strong brittle phase, while ferrite on its own is soft and ductile. Increasing the volume fraction of pearlite increased measured hardness in ferritic-pearlitic steel [81]. Using multiple repeats for each specimen alleviated this issue.

Investigations of the material hardness profile in the near-surface of burnished specimens revealed a weak correlation between the burnishing parameters and post-burnish properties.

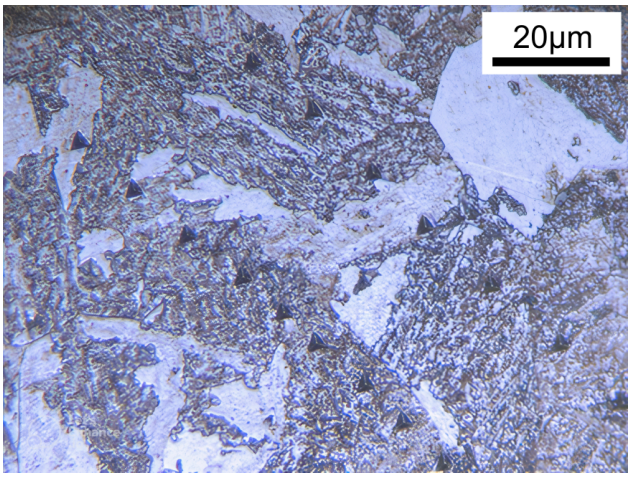

Figure 6.18: A micrograph of an example indented specimen with regions of ferrite and pearlite

The most aggressive burnishing parameters, as defined by the highest vertical feed rate, yielded the greatest improvement, with a 10% increase from 550HV to 605HV. Research suggests that reducing feed rate increases surface hardness up to a limit, through a mechanism of repeated strain hardening with successive passes [75]. However, this relationship was not seen here. As mentioned previously, the number of tool passes during internal roller burnishing is vastly larger than most burnishing processes and likely to exceed the limit of improvement identified in the literature [73]. Although surface hardness improved greatly for all burnished holes, a region of reduced hardness was identified below the heavily deformed near-surface region (Figure 6.19).

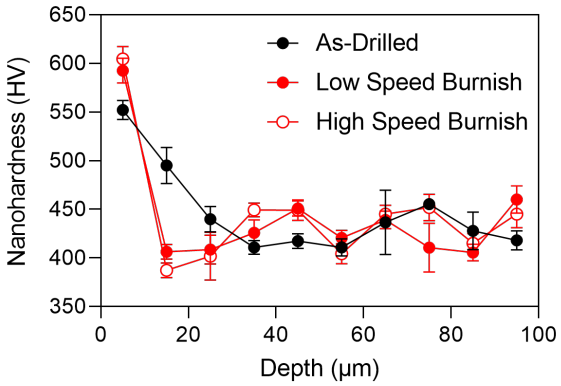

Figure 6.19: Nanohardness profiles for as-drilled and burnished hole conditions, demonstrating a reduction in hardness at 15μm

The measured hardness was below that measured during the drilling process, meaning this region had been softened by the burnishing process. The reduction in hardness between 15μm and 25μm depth was repeated at both parameter sets and multiple repeats and so was unlikely to have been a test error. There was also no evidence of the agglomeration of ferrite

which could have driven a reduction in measured hardness. Burnishing generates large shear stresses in the surface grains, which promotes grain refinement as a result of the associated increase in dislocation density, hence the large increase in hardness at 5μm. However, as a result of adiabatic heating during deformation and friction generated by the high-pressure and high-speed contact, significant quantities of heat are generated. The beneficial concentration of deformation in the near-surface may have originated from a reduction in flow stress within this area driven by the transmission of frictional heat from the contact zone. But, if this heat is sufficient to have an effect past this heavily deformed layer, a tempering effect may have been introduced to the layers beneath that do not experience the same magnitude of shear stress as the surface. Whilst tempering is predominantly used to improve ductility in 4140 steel with a martensitic microstructure, nanohardness analysis of a dual-phase steel revealed reduced ferrite grain hardness following tempering at temperatures below the austenite transition temperature [82]. As would be expected from the reduction in dislocation density that could happen at any elevated temperature. The rate at which tempering proceeds remains uncertain; however, deformed microstructures, like those found on drilled surfaces, tend to be more susceptible to recovery and static recrystallization when exposed to heat, which provides the thermal energy to increase the rate of the atomic diffusion and dislocation motion processes which underlie these changes. The internal strain energy accumulated during deformation acts as the primary driver for this behaviour. Consequently, significant changes in the microstructure can progress in a relatively brief timespan [83].

Interestingly, the greatest softening effect corresponded to the specimen burnished at the highest feed rate and burnishing speed, which also had the highest average force during the burnishing operation. If heat generation is the driving force behind the reduction in hardness, a concurrent reduction in forces would ordinarily be expected due to thermal softening. But this may have been negated by increased strain hardening due to strain rate sensitivity phenomena. In most metal alloys, larger strain rates induce a greater strain-hardening effect through a phenomenon termed strain rate sensitivity, where the material dynamically strengthens during deformation. Strain hardening can be enhanced by the presence of elevated temperatures, due to thermally-activated dislocation motion [84]. Strain-rate sensitivity is rarely a determinant property in material removal operations, since at the strain rates in the order of 10^5 that they operate at the variation with rate is negligible. Strain rates achieved during burnishing operations are much lower because of the lower resultant plastic strains. With successive rapid tool passes, dislocation density is raised, counteracting thermal softening behaviour and preventing a reduction in forces with burnishing speed, all whilst frictional heat is transmitted to the deeper layers. This hypothesis explains how a heavily deformed near-surface and region of reduced hardness can be generated without a significant reduction in burnishing forces.

The microstructure following burnishing has significant implications for the performance of the crankshaft oil hole that are not represented in the external burnishing fatigue testing literature. In the heavily deformed and work hardened near-surface layer, there is a high density of grain defects, generating high internal stresses, which may be beneficial and act as a barrier to limit crack initiation and early propagation. But fatigue life may be negatively impacted by the recovered region, due to its reduced yield strength, particularly if surface scratches that had not been removed by the burnishing process were to exceed this depth. A literature search did not identify further instances of this recovery phenomenon being reported in previous studies. However, the internal roller burnishing research is limited and hardness testing is often conducted at loads that are too large to capture variation seen here in the near-surface layers. It is therefore suggested that this phenomenon may occur quite widely in roller burnishing operations.

6.5 Contribution to drilling knowledge

Whilst the focus of this research was the surface integrity of burnished hole surfaces, the research provided insights that may be applicable to the drilling process. During internal roller burnishing, the contact between the rollers and the hole wall resembles the contact between the drill margin and the hole wall immediately following cutting, albeit with a more optimal contact geometry (Figure 6.20). The tool used in these studies utilised a new double-margin design, which increases the number of contact surfaces between the tool and the hole wall to four. It is hypothesised that the mechanisms by which surface integrity is improved in burnishing may also apply during the drilling operation and the surface integrity of drilled holes could be improved through studying contact between the margin and hole wall. During drilling it is commonly accepted that forces will decrease with rotational speed because the tool-workpiece contact will generate more frictional heat, which serves to increase material temperatures and reduce the flow stress required to initiate and maintain plastic deformation. This response is dominated by the mechanics of the chip removal process at the main cutting edges, so it is difficult to validate if the same force response occurs at the margin-wall contact. This is important because unlike other machining operations, this secondary contact ultimately determines the final microstructural condition of the hole wall. The burnishing operation is representative of this contact.

During burnishing, increasing speed was less impactful to forces than expected. Since there is no material removal in burnishing and the induced plastic strains are low compared to machining, it is possible that frictional forces were dominant. The work of Obadas [85] identified an increase in friction coefficient with increased sliding speed in a steel-steel contact. Contact temperature also increased with sliding speed and is likely to have increased adhesion and contributed to the friction change. This adhesion would drive large changes

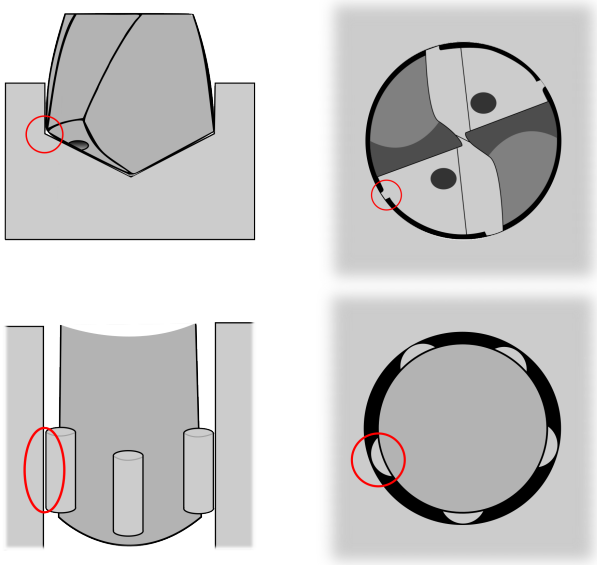

Figure 6.20: A schematic demonstrating the similarity in contact points during the drilling and burnishing process

to the sub-surface microstructure, since the surface would experience higher levels of shear. The margin-wall contact may also follow this same relationship.

In response to the results of this work and prior to conducting further characterisation, a short margin rubbing study was completed to determine whether the margin-wall contact could be studied in isolation. During the test a solid round drill was used in place of a burnishing tool and fed through a drilled hole. Cutting forces were monitored to validate contact between the tool and hole wall. Unfortunately there was evidence of excessive scratching and marring on the surface following the tool pass. The drill is very stiff and so is not able to accommodate acircularity in the hole by flexing and elastically deforming like the burnishing tool rollers. During the drilling cycle the tool is also stabilised and centered by the chisel edge, whereas during this tool pass the only contact was between the drill margin and hole wall.

6.6 Concluding Remarks

Internal roller burnishing of drilled holes yielded a significant improvement in surface finish, with a particular reduction in peak-to-valley height, concurrent with the deformation of surface asperities. The surface hardness was also improved over the drilled condition, which was attributed to concentrated deformation of grains under the applied shear stress. Operating at the most aggressive burnishing parameters encouraged the generation of a heavily deformed hole wall surface whilst providing the shortest cycle time. Unfortunately, a recovered region of low hardness was generated at approximately 10-20μm from the surface due to a hypothesised contact heat transfer effect. Although deformation was anticipated to diminish steadily

with depth, the results imply that the heat generated during contact is sufficient to reduce hardness at a not-insignificant distance from the surface. The mechanism behind the reduction in hardness was hypothesised to be the recovery of the structure and the reduction in dislocation density, although more advanced microscopy techniques are required to validate this. As recovery of the grain structure progresses, defects are annihilated and rearranged, leading to a decrease in hardness and a reduction in internal strain. This phenomenon was not identified in the literature, but this absence is attributed to the sparsity of internal roller burnishing research and frequent use of microhardness testing, which is incapable of measuring sufficiently close to the surface to capture regions affected by heat transfer. The recovered region of low hardness presents a possible route for rapid fatigue crack propagation through the material, should the manufacturing defects identified in Chapter 3 be present in the surface. This is not an acceptable surface outcome from an industrial perspective and extensive testing would be required to validate that the resultant microstructure was not detrimental to fatigue strength. A standardised testing method for the fatigue strength of holes loaded in combined bending and torsion is not currently available and therefore full component testing including hydropulse crankshaft fatigue studies would be required at great cost. As a result, the decision was made at this stage to focus research attention on the drilling process and not pursue burnishing further. This was reinforced by the acceptable hardness profile of the drilled surfaces, which was attributed to the new double-margin tool design.

It was also noted that extensive sample preparation was necessary to analyse samples through light optical microscopy, particularly because multiple burnishing parameters were used and a large number of repeats was needed. Still, limited information was gained. It is in the interests of industrial applicability for this research to continue investigating alternative combinations of techniques for sample characterisation that are less time and resource intensive.

Chapter 7

Microstructural Analysis of Drilled Surfaces

Research surrounding the characterisation of machined surfaces has gained pace in recent years, especially since the development of new measurement equipment including advanced optical profilometers and hardness testing machines and optimised experimental methodologies. Recent development of established techniques has improved the field of surface integrity and the study of the response of materials to machining. Despite the prevalence of drilling operations in manufacturing, the research surrounding the surface integrity of drilled holes is more limited than other machining operations. It is clear that the hole quality requirements of crankshaft oil holes are increasing year upon year, therefore consideration must be given to the capabilities of inspection methods for drilled surfaces.

It is clear from the results of the previous chapter that it is difficult to characterise the impact of the crankshaft drilling process on the microstructure of the material using optical microscopy alone. The size of the plastically deformed region is small, particularly with advanced tooling, and microstructural features are difficult to distinguish. Extensive sample preparation time is also required to generate results. Even then, the results may not always be useful. For example, optical micrographs were insufficient to identify the extent of burnishing-induced grain refinement, although the process is known to induce large microstructural changes. The near and sub-surface microstructure of a machined surface is a key contributor to the fatigue life of the material. As such, it is important to understand the impact of the machining process when designing loaded components. With this in mind, it was decided that alternative analysis techniques that were more suitable for industrial applications should be sought and investigated. The requirements included minimal preparation, fast setup, and the ability to differentiate samples with large microstructural differences. The technique did not have to work in isolation, but instead identify appropriate samples for further analysis with more costly and time-consuming techniques to encourage the efficient use of resources. Literature analysis together with industrial research identified X-ray

Diffractometry (XRD) and Barkhausen Noise Analysis (BN) as possible suitable methods for this purpose. The research also identified electron backscatter diffraction (EBSD) as a means of validating the findings of XRD and BN and conducting more extensive analysis once suitable samples had been selected. The expertise of the industrial partner in these areas is limited and exposure to these techniques and the results gained from this research allowed them to gain a useful insight into the crankshaft drilling process.

XRD is a versatile technique that can obtain information such as crystal structure, lattice strain, and crystal size by analysing the interaction between X-rays and material surfaces. This makes it ideal for characterising plastic deformation in the near-surface of machined specimens and is why it is frequently used to inspect materials. According to Braggs Law, the diffraction angle of the incident X-rays is a function of the inter-atomic spacing and can be used to quantify the magnitude of deformation (Figure 7.1).

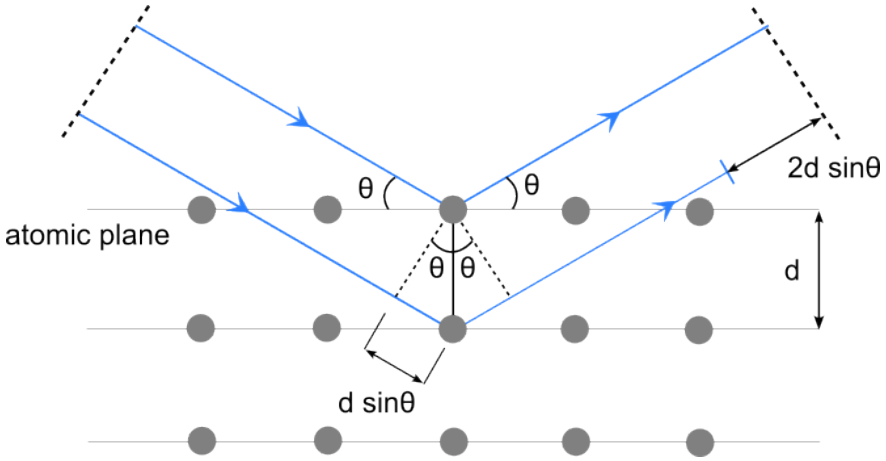

Figure 7.1: A schematic of X-ray Diffraction and the change in path length between diffracted waves

Many XRD analysis systems are limited by the small maximum sample size and the extensive sample preparation required before measurements can be taken, which is not favourable for industrial research. Whilst the literature is dominated by research involving static X-ray diffraction instruments and small samples, portable X-ray diffractometers are available, which enable measurement of larger specimens and workpieces without extensive preparation procedures. This makes them much more conducive to industrial crankshaft drilling research. The Proto i-XRD portable diffractometer allows measurements to be taken on much larger specimens such as machining workpieces. It was proposed that drilled workpieces could be sectioned with one band-saw sectioning procedure and then swiftly characterised using the portable diffractometer system. XRD analysis offers a faster method for characterising drilled-hole samples and establishing the results of changes in the industrial process. It also supports a simplified quality control process and allows samples of interest to be identified for further analysis.

Barkhausen noise analysis is a similarly valuable non-destructive testing technique that is capable of evaluating the near-surface microstructure by measuring the response of the material to the application of an electromagnetic field. Below the curie point, ferromagnetic materials comprise of regions in which the magnetic fields of atoms are aligned known as magnetic domains. When not under an applied external magnetic field, these domains are randomly oriented and separated by domain walls. When excited by an external magnetic field, the domains will tend to rotate toward the direction of the applied field, and preferably orientated domains will grow and absorb other domains [86]. Material defects such as inclusions limit this behaviour and thus increase the activation energy required for domain motion through a mechanism known as domain pinning [87]. This creates a lag between the increase in applied magnetic field and resultant change in magnetisation of the material [88]. Barkhausen Noise testing relies on this phenomenon of discontinuous increase in magnetic flux density to characterise materials.

During BN testing, a magnetic field generated by a excitation probe under an applied magnetising current passes through the material. As the magnetic field strength increases the magnetic domains within grains begin to align themselves with the direction of the applied field (Figure 7.2). Any aforementioned pinning sites restrict this evolution. When the magnetic field is strong enough to overcome this energy barrier, the group of atoms flip their spin almost instantaneously. The sudden change in magnetic polarisation introduces a sharp change in magnetic flux, which is captured by a measurement probe.

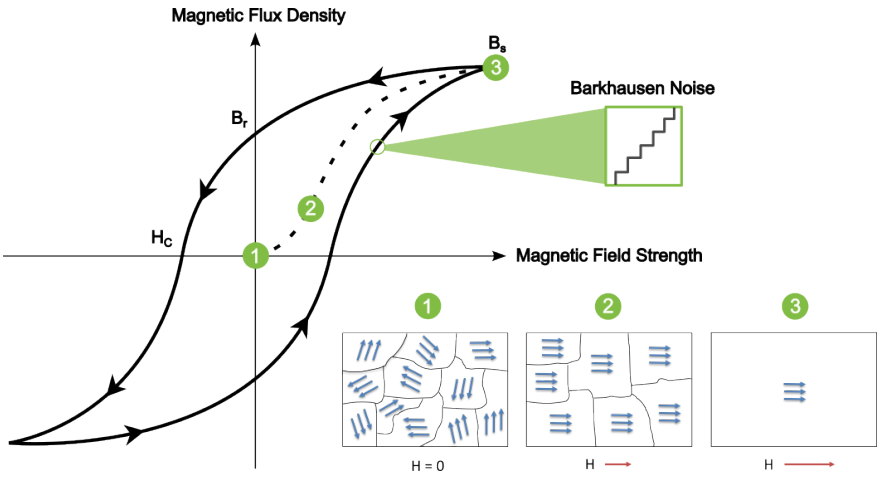

Figure 7.2: Domain wall motion and change in magnetic flux density in the material under the application of increasing magnetic field strength

The quantity of Barkhausen Noise emitted is linked to the number of pinning sites [89]. Increased hardness and compressive residual stress in the near surface driven by plastic deformation change the rate of change of magnetic flux. Unfortunately, these two properties have similar effects on the BN signal. Ordinarily this would pose a problem for materials analysis and would necessitate lengthy characterisation studies. Fortunately, if the holes

are sectioned open across their diameter, most of the residual stresses in the circumferential direction will have been relieved. Theoretically, the influence of residual stress on the Barkhausen Noise Signal is then reduced and the response becomes dominated by the microstructural composition of the near-surface. A schematic of a Barkhausen measurement probe and an example response signal is shown in Figure 7.3.

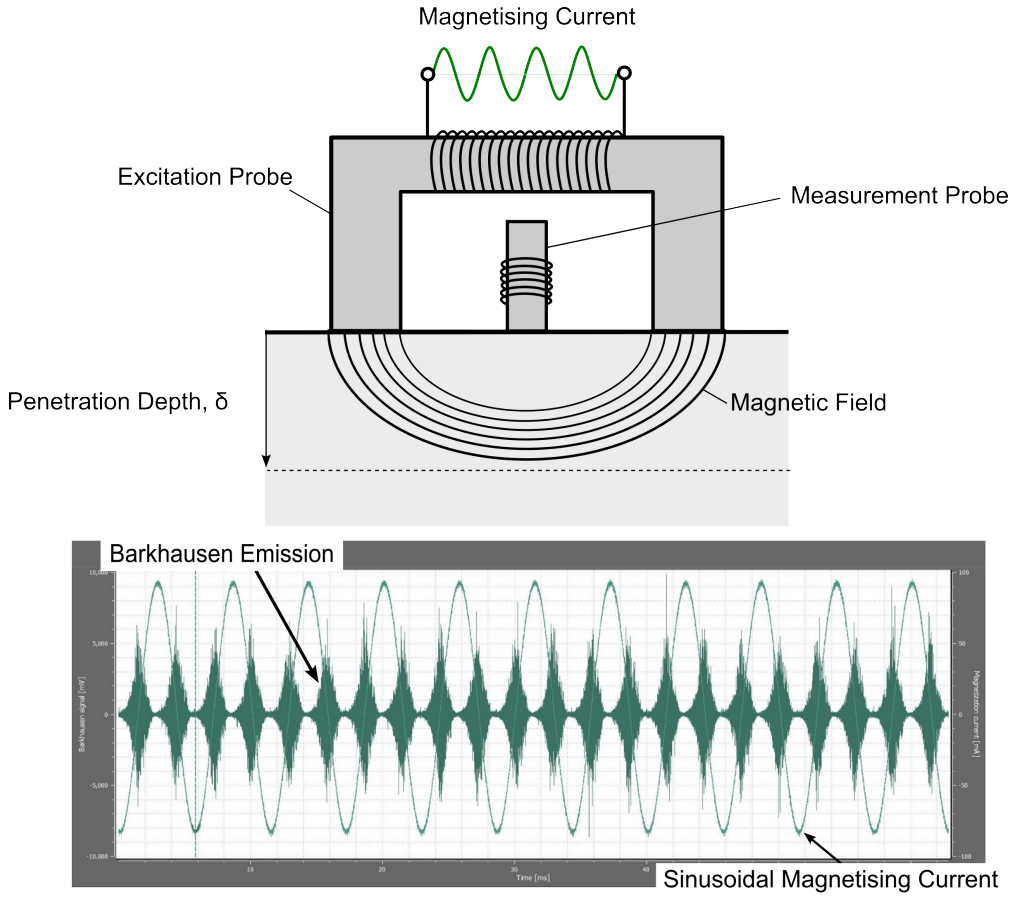

Figure 7.3: A schematic of a Barkhausen Noise measurement probe, with an example profile showing the emitted Barkhausen Noise with the change in magnetising current

With the potential advantages of these techniques in mind, an experimental scheme was devised to assess the capabilities of XRD and BN analysis and better understand the crankshaft oil hole drilling process. Since the use of XRD and Barkhausen Noise analysis for this application and in this setting is novel, the results of these analyses had to be verified with another established technology. Electron Back Scatter Diffraction (EBSD) was chosen for this purpose because of the high level of microstructural detail it provides across the entire thickness of the machining-affected layer. Electron back-scatter diffraction is an SEM technique used for the characterisation of the crystallographic orientation of materials that has shown effectiveness in phase identification in steel alloys [90]. The technique generates a map of a material's constituent grains and their respective phases by indexing the diffraction patterns produced when an electron beam interacts with the crystal lattice. These diffraction patterns, known as Kakuchi bands are identified automatically by the software through

use of a Hough transform, a robust image detection algorithm for the detection of linear features. This data is captured rapidly as the microscope scans the surface and colour-coded to signify regions of similar orientation. EBSD analysis is much higher resolution than optical microscopy and is even capable of characterising sub-grain boundaries and damage. EBSD analysis of sectioned hole specimens could provide a quantitative assessment of grain disorientation that can be used to establish the level and distribution of deformation within the near surface of machined specimens and validate the findings of XRD and Barkhausen noise analysis.

7.1 Experimental Method

In this section the setup and method of operation of the XRD and BN analysis equipment is first described, followed by the experimental scheme to investigate their effectiveness. This includes the justification for the sample types that were chosen and the measurement locations that were used.

7.1.1 X-Ray Diffraction

A Proto iXRD portable residual stress diffractometer equipped with a chromium X-ray tube was used for XRD inspection. An example of the setup with a sectioned hole sample in place is shown in Figure 7.4.

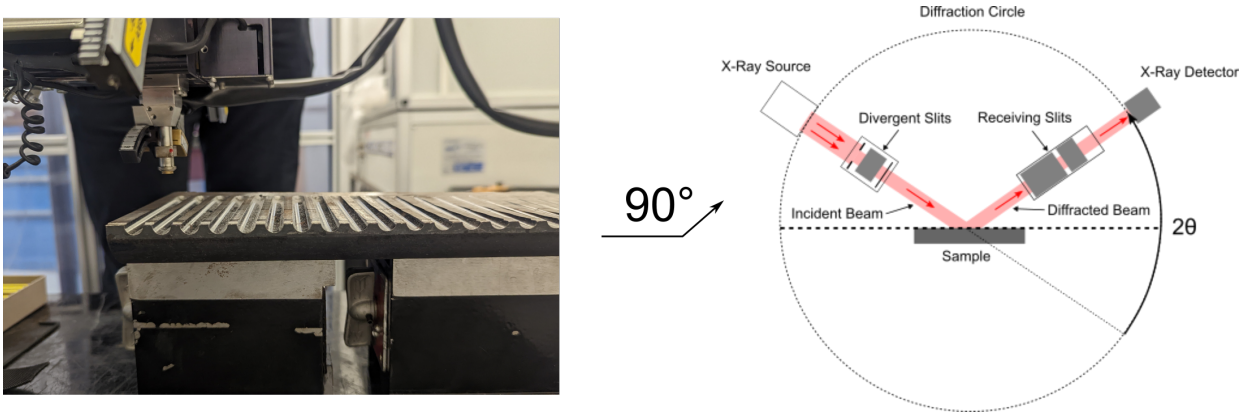

Figure 7.4: Proto iXRD portable diffractometer with a hole sample in place beneath the transmitter alongside a schematic of the beam travel

All samples were mounted in this way, with the hole axis parallel with the diffractometer bed. This was done to ensure a repeatable incident angle between the transmitted X-rays and the hole wall surface. For all samples, the body-centered cubic (211) diffraction peak was captured using a 1 mm diameter X-ray aperture with a 2 second X-ray exposure and 10 exposures per measurement. Following background correction, a Pseudo-Voigt distribution was then fitted to the (211) diffraction peak and the full width at half maximum (FWHM)

peak breadth, peak position and intensity were then extracted. These parameters were chosen since past results with similar applications suggested that these were the most sensitive to microstructural changes. The estimated penetration depth for 90% attenuation of X-rays was 11.80 µm. Measurements were only completed at a single tilt angle, which prevented the calculation of residual stresses. However, the essential sectioning procedure had altered the residual surface stress of all samples and would have invalidated the results regardless. Measurements were repeated at each location for a total of three results.

7.1.2 Barkhausen Noise Analysis

The Stresstech Rollscan 350 Barkhausen Noise Analyser was used alongside the SX-14 handheld gear sensor for all samples. Despite the fact it was designed for measuring gear teeth, it was able to make full contact with the hole wall. The Barkhausen Noise analysis equipment setup is shown in Figure 7.5. Magnetising current and voltage sweeps were initially

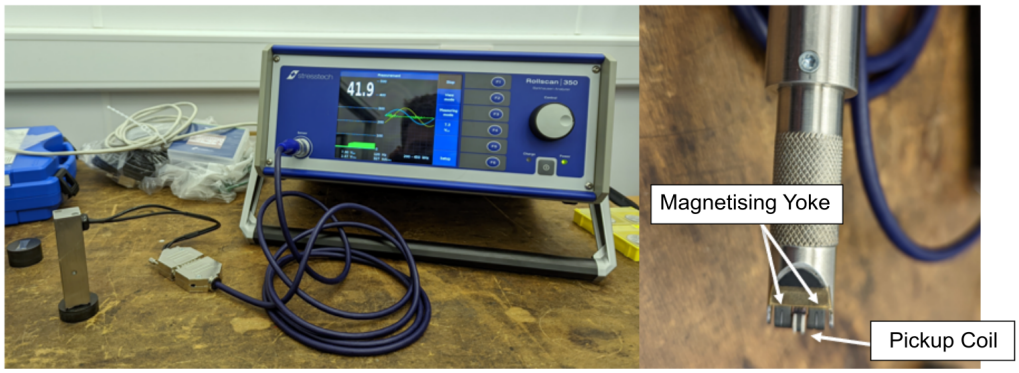

Figure 7.5: Rollscan 350 Barkhausen Noise Analyser and SX-14 handheld gear sensor

conducted to determine the optimal parameters to maximise the barkhausen noise signal without exceeding the sensor cutoff limits. The test parameters were selected as follows: sinusoidal magnetising current waveform, 8V magnetising voltage, 100Hz excitation frequency and 200KHz frequency filter. The penetration depth of the BN measurement is dependent on the properties of the material being measured and the selected excitation frequency. Estimated penetration depth, ∂, can be calculated using Equation 7.1.

$$\partial = \frac{1}{\sqrt{\pi \mu \sigma f}} \tag{7.1}$$

In this equation μ denotes permeability, σ represents electrical conductivity and f denotes the frequency of the alternating magnetic field. Frequency, f is the only variable that can be modulated, and this can only be done within a limited range. At the test parameters chosen here, the estimated penetration depth of the barkhausen noise signal was limited to around 2mm. This damping effect occurs due to the opposing eddy currents generated by the magnetic field. Fortunately, the analysis depth is different to the penetration depth and

can be reduced by increasing the analysing frequency filter. At the selected frequency filter of 200KHz, the measured barkhausen noise response was limited to approximately 75 μm.

7.1.3 Electron Back Scatter Diffraction

EBSD analysis was conducted using a JEOL-JSM 7900F microscope, coupled to an Oxford Instruments Aztec HKL Advanced Symmetry Measurement System (Figure 7.6). Each sample was imaged at two resolutions. Several analyses were then completed on the captured EBSD microsections, including band contrast, polar analysis, grain average misorientation, and phase identification. The results of these analyses were compared to the XRD and BN inspection results, to aid in understanding the response of these technologies to changes in the microstructure of the material.

Figure 7.6: JEOL-JSM 7900F microscope used for EBSD analysis

7.1.4 Experimental Test Plan

Initial tests were performed on two segmented halves of a crankshaft oil hole that had been extracted from an induction-hardened crankshaft journal bearing. The bearing was sectioned from a manufactured crankshaft using wire EDM. The bearing had undergone induction hardening to a depth of 4mm, which resulted in a smooth transition from martensitic to ferritic-pearlitic microstructure, which was anticipated to show significant variation in XRD and BN responses. Macro-etching of the sectioned sample confirmed the presence of a 4mm induction hardened layer of refined martensite in contrast to the predominantly ferric microstructure of the bulk material. This initial test assessed whether the techniques were capable of detecting large-scale microstructural changes in sectioned hole specimens with known heat treatment. This journal-bearing specimen was extracted from a crankshaft that had been removed from service and sectioned to reveal the inner hole wall. The specimens are shown in Figure 7.7. XRD measurements were taken in discrete 1mm intervals, ranging from 1-10mm from the hole exit, with three single-point readings at each interval. Barkhausen

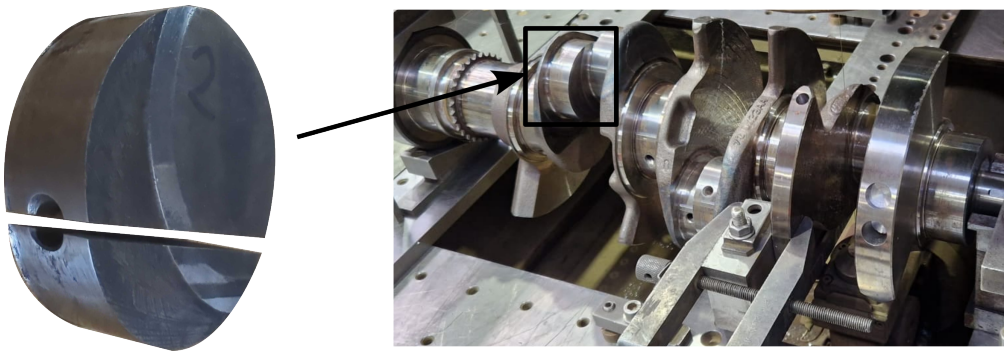

Figure 7.7: Sectioned crankshaft journal bearing specimen and extraction location

Noise measurements were taken at 2mm and 8mm from the surface due to the size of the excitation probe, which limited the resolution. The number of repeats at each measurement location was also increased from three to five due to difficulties in ensuring consistent contact with the workpiece. EBSD analysis was not necessary for the crankshaft specimens since they had undergone a controlled industrial heat treatment that had been validated during manufacture and confirmed with macro-etching after sectioning.

After successfully locating the induction hardened layer in the crankshaft oil hole, the study then progressed to burnished and drilled hole specimens. This decision was based on the substantial deformation the burnishing process introduces to the surface without any expected phase changes. The burnished region was expected to exhibit a larger XRD peak breadth and reduced BN peak height concurrent with larger quantities of lattice strain. Whilst drilling also causes disruption of the lattice in the near-surface, the magnitude of deformation is lower and less concentrated than in burnishing. This is useful for validating the effectiveness of XRD and BN in identifying near-surface microstructural changes. Furthermore, as described in the previous chapter, it was difficult to assess these near-surface changes with optical microscopy alone, and the small attenuation depth of the X-rays focuses the analysis on the deformed region. Drilled and burnished holes from the previous work were selected as appropriate test specimens due to the known near-surface deformation that had occurred. The generation of these holes is described in the previous chapter. 20 holes of 96mm depth were selected. 10 were in the as-drilled condition, and 10 had been burnished to a depth of 48mm. Holes were examined at depths of 40mm and 60mm since these are in close proximity but capture the burnished and as-drilled portions of the burnished holes. The proximity of the locations reduces any changes in tool and workpiece temperature during machining as a result of the tool being deeper in the hole at the point of measurement. After inspection was completed, a single hole burnished at the highest vertical feed rate was selected for EBSD analysis, since this condition had demonstrated high near-surface hardness followed by a reduced hardness region beneath. The hole was sectioned to separate the burnished and as-drilled portion and mounted following the procedure described in Section 4.4, to allow the two conditions to be compared.

7.2 Results

XRD and BN analysis was conducted on two halves of an induction-hardened crankshaft oil hole specimen, with measurements taken at varied distances from the hole breakout. The change in full width at half maximum (FWHM) peak breadth of the XRD response with increasing hole depth is presented in Figure 7.8. The zero datum is taken from the depth of the deepest hole chamfer. Both specimens exhibited a broad peak response at the top of

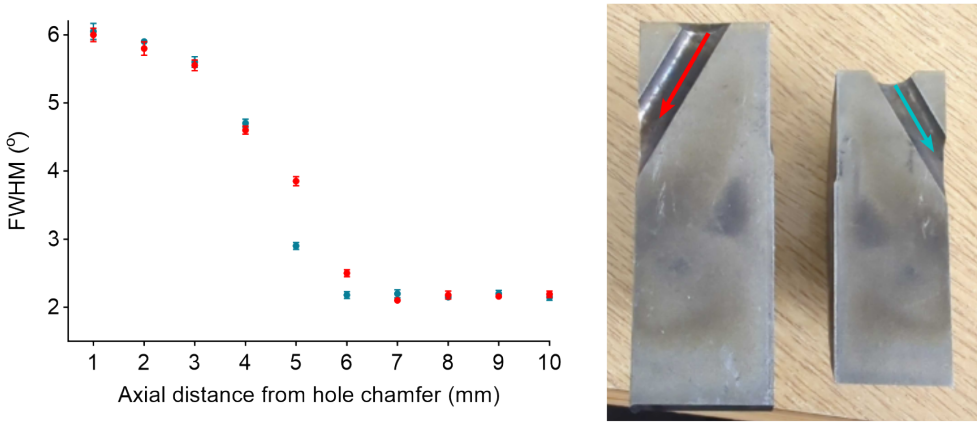

Figure 7.8: Change in Full-Width at Half Maximum peak breadth with increasing hole depth for both halves of the oil hole

the hole, close to the bearing surface, which tapered off as depth increased. BN analysis was also conducted on the smaller specimen at 2mm and 8mm (Figure 7.9). There was a clear difference in BN response amplitude between the martensite-dominant induction hardened layer and the predominantly ferritic core microstructure. The amplitude of the BN response for the martensitic microstructure is much lower, signifying greater resistance to change in magnetic flux due to increased hardness. After successful validation that the techniques were capable of detecting phase changes, burnished and drilled hole specimens were examined. The measured XRD FWHM peak breadth for all inspected holes is shown in Figure 7.10, with error bars calculated from the standard deviation of multiple repeats. The burnished measurement locations are highlighted. The left 5 holes were burnished with the smaller diameter, the right 5 were burnished with a larger tool diameter and, thus, larger axial interference.

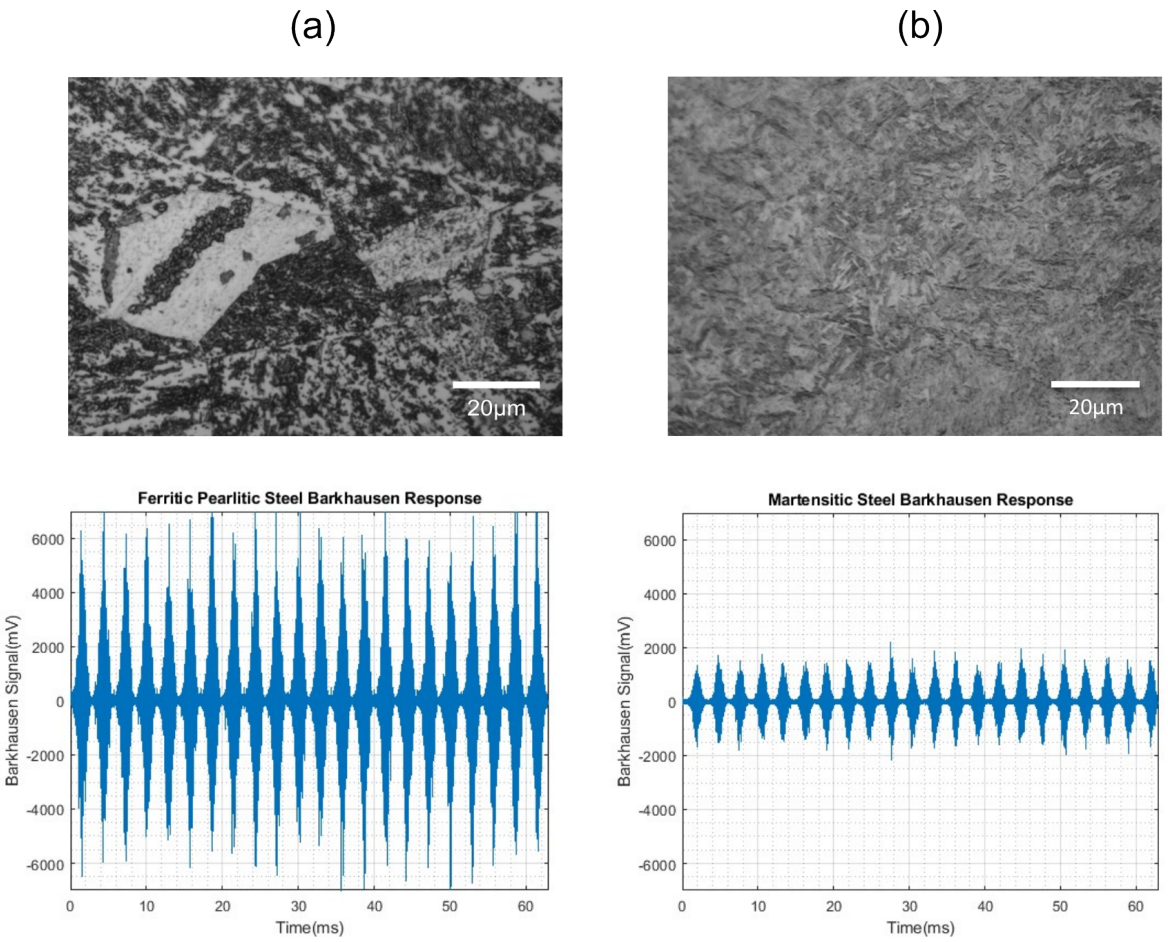

Figure 7.9: Change in barkhausen signal response for an (a) as-rolled ferritic-pearlitic microstructure and (b) induction hardened martensitic microstructure

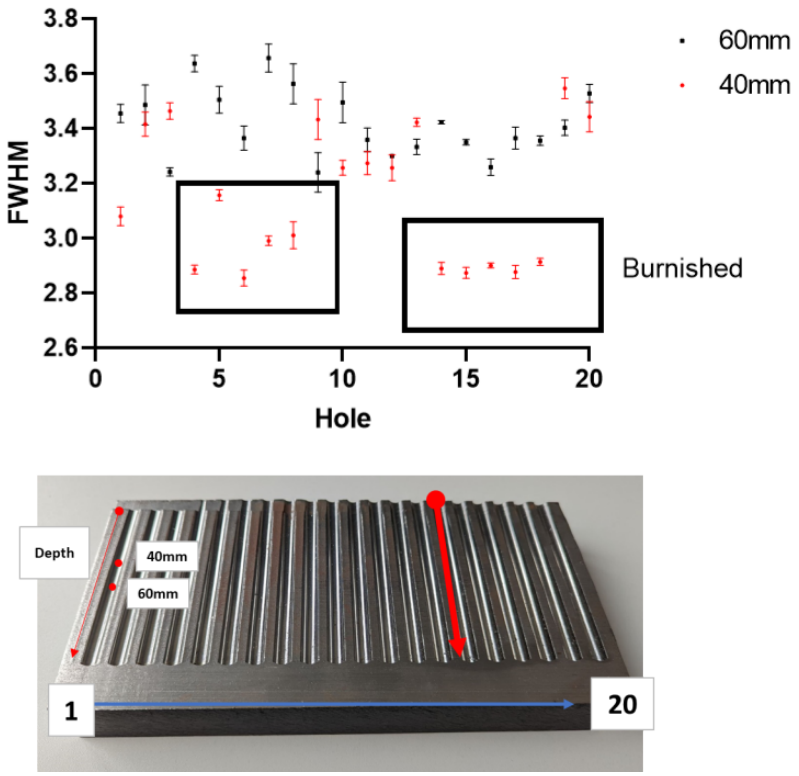

Figure 7.10: Change in FWHM peak breadth response across multiple holes and depths

The as-drilled holes without a burnishing treatment did not show a clear correlation between depth and measured peak breadth; for holes 1,10,11 and 20 peak breadth increased with depth. For holes 3,9,13 and 19 peak breadth decreased with depth and finally, for holes 2 and 12 the difference in peak breadth between the two depths was within the margin of error of the measurement. The as-drilled surface of hole 1 at 40mm hole depth exhibited a much lower FHWM than the other drilled holes, with a result close to the burnished holes. Interestingly, at 60mm depth the response was much higher/wider. This was the first hole machined with this tool. The burnished regions generated a narrower response peak on average with a lower FWHM. For the holes burnished with the small tool diameter, with less plastic deformation induced in the surface, there was a large change in FWHM with the parameter sets. The result for the burnished surface of hole 5, which was burnished at a high feed rate and low speed, had the broadest FWHM and was close to the average of the drilled surfaces. The surfaces burnished at the larger tool diameter, with greater plastic deformation induced in the surface, generated a lower FWHM that did not vary significantly with burnishing parameters. The repeatability of the results was also improved. XRD peak position was also evaluated and was consistent in most drilled samples (Figure 7.11). Furthemore, peak position did not change following burnishing. Hole 8 exhibited a particularly high peak position in both the drilled and burnished regions. Because XRD

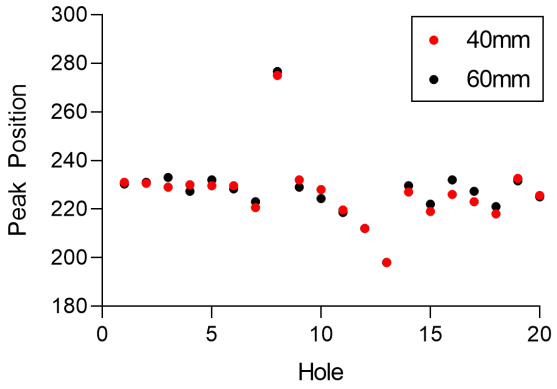

Figure 7.11: Measured peak position of the XRD response for all measured surfaces

analysis had identified a more consistent response for the five holes burnished with a larger diameter tool, only these holes were taken forward for barkhausen noise measurements. The maximum barkhausen burst peak height was calculated for the as-drilled and burnished portions of these holes (Figure 7.12). The burst peak height exhibited minor variation between the drilled and burnished conditions. The burnished surfaces returned a reduced average BN response compared to the as-drilled surfaces of the same hole. However, there was an overlap between the error bars of three of the five holes. The burnished parts of holes 14 to 17 also exhibited a greater peak height than the drilled portion of hole 18. Coercivity was also measured and was unchanged between samples, suggesting there was no residual

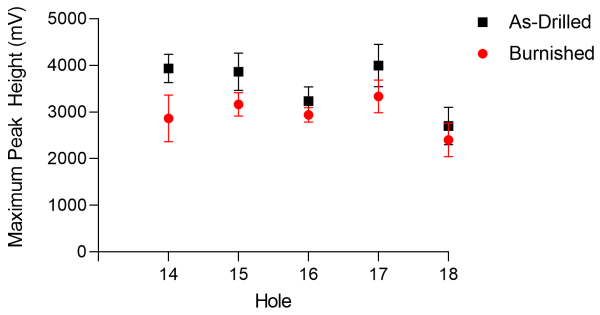

Figure 7.12: Change in maximum burst peak height following burnishing

stress differential [91]. Now that the influence of the processing of the holes on the XRD and BN response had been discovered, it was important to identify any physical microstructural changes that may have driven the behaviour. Analysis from the previous chapter discovered an unexpected hardness profile in the burnished specimens, but Light-Optical Microscopy was insufficient to characterise the microstructural changes. As EBSD is a time consuming and expensive, only one hole was selected for analysis. Hole set 2, which had been burnished at the larger tool diameter yielded a significantly more consistent XRD response than set 1. Hole 18 from set 2 was chosen as it was processed at the mid-range of the burnishing parameters and expected to be the most representative. Crystallographic analysis of the drilled and burnished portion of hole 18 was conducted using EBSD. Figure 7.13 highlights the captured kakuchi band patterns in the near-surface and subsurface regions of a drilled sample. The software was incapable of identifying kakuchi bands in regions of the near-surface of all samples, signifying a highly deformed crystal structure.

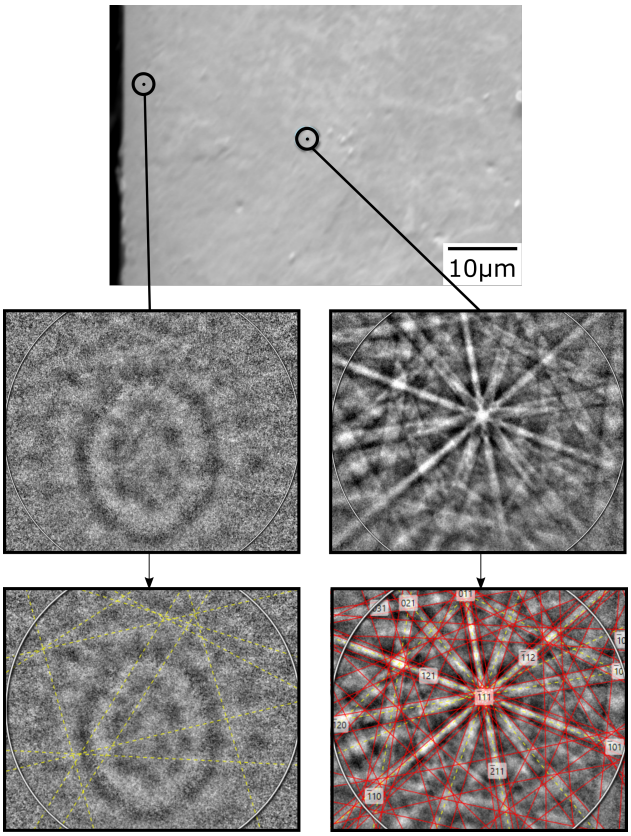

Figure 7.13: Presence of kakuchi bands in the analysed microstructure and change in indexing behaviour with distance from the hole wall surface

High levels of deformation coincide with large lattice strains, which can cause difficulties in indexing grains. The step size was reduced to 2nm to increase the likelihood of indexing. This was the minimum step size at which a scan could be completed in a reasonable time frame. Indexing across the sample improved, but despite the reduction in step size, the near-surface regions still contained un-indexed regions that can be seen in black on all of the following results. Step size was consistent across all maps, therefore the size of these regions can be compared between drilled and burnished specimens. It is important to note that surface imperfections and sample alignment can also influence indexing behavior.

A scan of the core microstructure of the material, well beyond any machining-affected layers, revealed an anisotropic BCC microstructure. An inverse pole figure (IPF) map combined with a grain boundary plot and a summary of the orientation of grain boundaries for both surface conditions is shown in Figure 7.14. In general, the IPF map is a measure of the relative crystal orientations with respect to the sample direction. The deformation in the machining direction is prominent for both the drilled and burnished specimens, with evidence of shearing along the tool path direction. For the burnished specimen a unindexed 3 µm surface layer can be found, signifying a very fine-grained microstructure. Below this is a fine-grained texture deformed in the burnishing direction up to 8µm from the surface. The

drilled microstructure contains less localised deformation. The deformed grains increase in size with increasing depth but are small compared to the burnished specimen. Small linear scratches can be seen across the sample that derive from the polishing procedure. These are not large enough to be of concern. To confirm the distribution of deformation across the

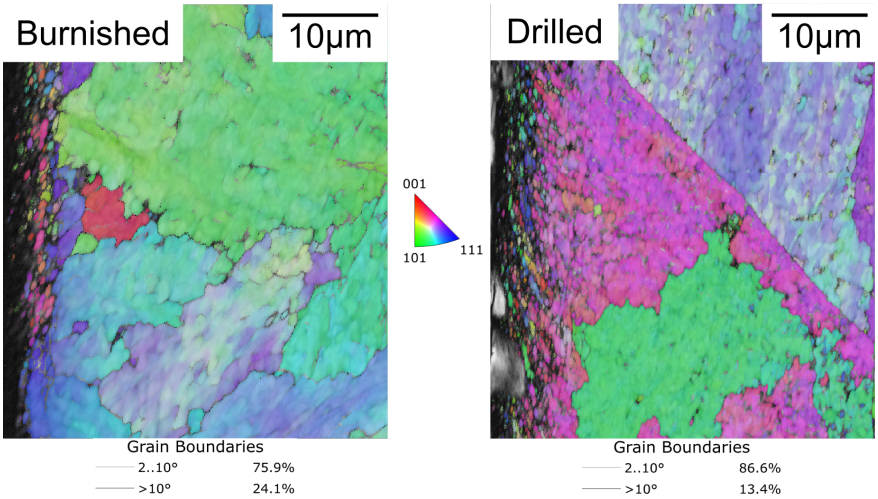

Figure 7.14: Polar orientation map of the burnished and drilled portion of a single hole alongside the distribution of grain boundary angles

sample a Kernel Average Misorientation was performed to assess the local misorientation of grains. A map of the results is shown in Figure 7.15, with green regions representing high local grain misorientation. Large quanitites of grain misorientation are present much further below the surface for the drilled sample and extend all the way across the scanned area. Grain misorientation in the burnished sample is concentrated to smaller areas, particularly toward the surface.

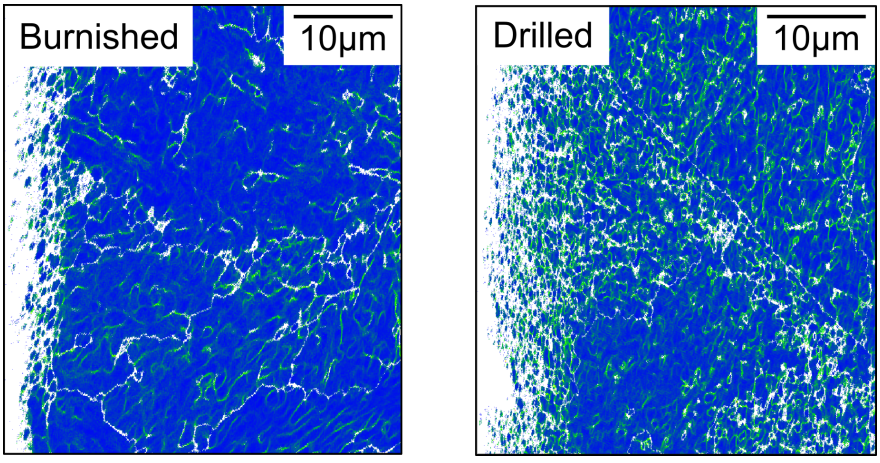

Figure 7.15: Kernel Average Misorientation map of the as-drilled and burnished portion of a single hole, with green regions representing greater disorientation

7.3 Discussion

The discussion of the results of this work will be separated into three main subsections: two subsections analysing the results of BN and XRD analysis and their ability to characterise the observed microstructure and another discussing the implications of these results for the drilling and burnishing processes.

7.3.1 Applicability of XRD for drilled surface analysis

The peak breadth of the XRD response was obtained for burnished and as-drilled holes at depths of 40mm and 60mm. Peak breadth was calculated as the width of the peak at half of the maximum peak intensity (FWHM) and may be used as an indicator of lattice strain and grain size change within the surface measurement region. Peak broadening is typically associated with a reduction in grain size and subsequent increase in hardness [92]. As the crystal lattices become orientated in similar orientations, their contribution to the diffraction increases, and the diffraction peak sharpens.

The drilled samples presented a highly variable peak breadth and the depth of measurement did not show a repeatable influence on the XRD response. This suggested that steady-state temperature had already been achieved prior to the initial measurement depth, and the proximity of the measurements successfully offset any disparities arising from chip evacuation variability. Despite the clear presence of a heavily deformed near-surface region with a diminished crystallite grain size in the burnished samples, the XRD response did not show evidence of the peak broadening behaviour frequently reported in the literature [93] . Contrary to the literature, the FWHM peak breadth was markedly reduced for all burnished surfaces. Past studies have noted difficulty correlating microstructural evolution with the XRD response due to the large influence of residual stresses and phase changes [94]. However, in the case of the machined holes, residual stresses in the hole wall are likely to have been at least partially relieved during the sectioning procedure, reducing the influence of residual stresses on the XRD response. Furthermore, optical microscopy of the samples did not reveal any clear phase transformations or white-layer formation in the near-surface. Consequently, it could reasonably be assumed that the peak narrowing seen in the results was predominantly driven by grain evolution effects. The Scherrer Equation (Equation 7.2) is frequently used to describe the relationship between grain size and the FWHM XRD response. In this equation, the peak width, B is inversely proportional to the grain size, L defined as the cube root of the grain volume.

$$B(2\theta) = \frac{K\lambda}{L\cos\theta} \tag{7.2}$$

In reality, crystals are not perfectly cubic, particularly after plastic deformation in a concentrated direction. The Scherrer relationship is also valid only for grains on the nanometre scale, which is far smaller than the expected grain sizes for burnished and drilled surfaces. Broad correlations between crystallite size and XRD response would therefore be unjustified, despite the consistent use in the literature.

Brown et al. [93] noted a reduction in peak breadth of steels following grinding that corresponded to a tempered layer. Although high levels of plastic deformation had occurred, temperatures were sufficient to encourage the diffusion of carbon out of the martensite, resulting in a tempered martensite microstructure. Tempering decreases the dislocation density and yields a reduction in strain in the crystal lattice that reduces the measured peak breadth. A rehardened region was also identified and correlated with a sharp increase. Rehardening occurs when the heat generated causes local temperatures to exceed austenisation temperature and upon rapid cooling a highly strained martensite layer is formed. It is interesting that both microstructural changes were the result of temperature effects, and yet the peak breadth varied diametrically. Martensite is capable of tempering because the strain within the transformed phase is high and can be partially relieved with the application of heat. The microstructure of the burnished surface was primarily ferritic-pearlitic. This combination of phases has a much lower base strain at formation and will not temper through the diffusion of carbon. However, it is possible for grain recovery to initiate, where deformed grains can reduce their internal energy by rearranging to annihilate crystal defects. The EBSD results were interrogated to find evidence of strain reduction within the examined XRD layer.

Band contrast maps were first interrogated to compare grain size and microstructural refinement between the two samples. Band contrast is influenced by factors other than strain, including geometric setup, material phases, and parameters used for the Hough transform. All of these variables prevent the possibility of using BC as an absolute measurement for different scans; however, in a given map, they should remain unchanged. Unfortunately, the band contrast also depends on orientation, which is not constant except for highly textured materials [95]. The crystallographic texture of both samples varied across both samples, from the machined near-surface material to the forged core material, as evidenced by the change in polar orientation. It could be argued that the crystallographic texture within the plastically deformed layer should be consistent due to the consistent direction of applied shear stress. This would allow band contrast to serve as a descriptor of the relative strain distribution within this area. However, polar orientation analysis did not identify a dominant texture, and therefore the band-contrast images could not be reliably used to analyse deformation. Subsequent Euler mapping and Kernel Average Misorientation analysis revealed an intense 3μm band of deformation at the surface of the burnished specimen that could not be indexed, followed by a thin layer of refined grains. The total depth of the plastically deformed layer was approximately 8μm.

The X-rays penetrate a small distance into the material before reducing in intensity through a phenomenon known as attenuation. Attenuation occurs because each time an X-ray photon interacts with an atom of the specimen material, it is removed from the beam. This limits the depth of XRD analysis to the near-surface. This is ideal for crankshaft drilling since the plastically deformed layer is small, as evidenced in Chapter 6. The recovered region of low plastic strain likely dominated the XRD response and negated the expected peak broadening effect caused by the heavily deformed near-surface. XRD can clearly identify that changes in crystal structure have occured in the near-surface of drilled specimens. On the basis of these results, XRD is suitable for on-line quality control of drilled holes and identification of hole specimens for further analysis. However, it cannot be used in isolation to characterise the near-surface microstructure due to an inability to distinguish between the competing effects of localised surface strain and near-surface grain evolution. It may, however, be suitable for other machining processes with deeper plastically deformed layers.

7.3.2 Applicability of BN for drilled surface analysis

BN analysis successfully distinguished the induction hardened layer of the crankshaft specimen. The transition from refined martensite at the near-surface of the bearing to as-forged ferrite in the core microstructure was mirrored by a large drop in BN peak signal amplitude. Martensite is supersaturated with carbon, which generates large quantities of internal elastic strain. This internal strain and increased inclusion density yields a greater resistance to domain wall motion than ferrite and a significantly reduced barkhausen signal amplitude.

The change in barkhausen response following burnishing was much less significant. BN has previously been successfully used to evaluate large microstructural changes in alloy steels. RMS of the BN signal was found to decrease with increased hardening depth following grinding, due to a larger proportion of the inspection region containing the highly strained martensitic phase [96]. EN91 steel specimens with varying heat treatments and compositions including tempered martensite, coarsened martensite and ferrite were also distinguished with BN analysis [97]. Both phase composition and grain refinement impacted the magnetic properties of the material but the phase change from tempered martensite to ferrite was more influential than grain refinement/coarsening of tempered martensite. This presents difficulties for drilling and burnishing research where phase change is not expected. Indeed, no phase change was observed from the band contrast analysis, but there was large magnitudes of grain refinement in the near surface. As evidenced by the EBSD analysis, the near-surface heavily deformed region is approximately 10μm thick, which is much smaller than the measurement depth of BN. The lack of a significant BN response may be attributed to the dominance of the core microstructure. Magnetising frequency was modulated to reduce the attenuation depth of the magnetising probe and limit measurement to the near-surface region. However, even at the maximum frequency of 200kHz the lowest depth that could be

achieved was estimated to be 75μm and limited changes to BN response were noted. More advanced barkhausen analysis equipment that is able to operate at higher frequencies may be more appropriate for analysis of drilled samples.

7.3.3 Implications for Burnishing and Drilling

The XRD, BN and EBSD analysis conducted in this chapter not only provides a faster method of characterising machined microstructures, but also provides insights into the generated microstructures following drilling and burnishing that were not attainable during past analyses and are worth discussing. The variation in the XRD responses among holes burnished with varying tool diameters underscores the notion that, while the initial tool setting procedure offers a baseline diameter, continuous monitoring and subsequent adjustments are essential to guarantee optimal tool contact. Despite the improvement in repeatability at the larger tool diameter, the FWHM peak breadth did not increase as expected. The XRD response displayed a notably reduced peak breadth in comparison to the as-drilled surface, signifying a reduction in lattice strain concurrent with lower quantities of deformation. The burnished holes had previously shown evidence of a near-surface region of reduced hardness following nanohardness examination in the previous chapter. Burnishing was expected to yield either an improved or identical hardness profile to the as-drilled condition and so the results were unusual. This discrepancy was explained by EBSD analysis, which revealed a microstructural profile that featured a low-strain region beneath the extensively plastically deformed near-surface region. Nanohardness testing was a costly and time consuming process that required extensive sample preparation and because of this repeats were limited. There may have been other interesting and novel microstructural features within other samples that were not discovered. It is clear that XRD analysis is at the very least capable of detecting microstructural evolution in ferritic-pearlitic steels and in future may be used to identify features of interest.

High contact temperatures in machining are heavily linked to the formation of tensile residual stresses in the literature, which are detrimental for in-service fatigue life. Residual stress has been quantified through XRD spectrum analysis in other studies and correlated to the propagation of cracks through the material under loading [98]. Due to the inherent inaccessible geometry of drilled holes, it was not possible to measure the residual stress profile of the machined surface in this study. Alternative sectioning procedures were tried without success. Unfortunately, this is a limitation that frequently presents itself in hole generation research.

7.4 Concluding Remarks

It is clear when comparing the results of this study to the research literature that electromagnetic properties are highly material and microstructure specific. Inspection techniques must be calibrated to particular materials and tailored to monitor known microstructural changes, if these techniques are to be deployed with confidence. Since BN could not reliably identify microstructural changes following burnishing due to the large ratio of inspection depth to machining affected layer, it is unlikely that it will benefit future research on drilled specimens. Hardness measurements taken in previous chapters demonstrate that grain refinement reduces significantly beyond the near-surface. BN analysis may still be useful when the microstructural condition is uniform across a large volume of the specimen, such as during materials testing.

XRD was capable of detecting large changes in the microstructure of sectioned hole samples. The XRD FWHM peak breadth response was significantly altered by the presence of martensite in the induction-hardened microstructure and also demonstrated a smooth reduction across the transition layer where ferrite and pearlite became the dominant phases. The XRD response varied significantly across several drilled microstructures, despite the identical process parameters, with no clear relationship between FWHM and hole depth. More research is needed to verify the cause of this variation, but this is beyond the scope of this project. Burnishing of the surface yielded a reduction in FWHM after deformation. Through EBSD interrogation of the crystallographic orientation across the sample, peak narrowing following burnishing was linked to a region with a recovered structure of low dislocation density adjacent to the surface plastically deformed layer. This was supported by hardness testing results from the previous chapter which identified a sub-surface region of low hardness. Despite the extensive deformation at the surface, the microstructure in this recovered region is believed to have dominated the XRD response and caused a reduction in FWHM.

EBSD provided significantly more information than was attainable with Light Optical Microscopy without significantly higher analysis time, due to the prior screening of samples with XRD. The combined use of XRD for initial sample screening and EBSD for in-depth analysis offers a useful route for industrial materials investigations.

Chapter 8

Thermomechanical analysis of deformation characteristics

This chapter highlights the importance of the temperature-dependence of material properties in machining operations and, to obtain the information of specific importance to this work, examines the behaviour of AISI 4140 steel during hot deformation through application of thermo-mechanical materials testing. The results of materials characterisation are reported, alongside the experimental methods used to obtain them. Specimens are deformed at various temperatures, strain rates and strains and analysed through microstructural analyses including optical microscopy and hardness testing. Compression tests are also conducted at temperatures above the austenite transition temperature to study the effect of prior deformation on post-quench martensitic microstructure. A discussion identifies the main changes in flow behaviour and post-deformation microstructure that are driven by material processing and explains how changes in material response due to processing parameters may be evidenced in the machining process. Based on this work, it is proposed that coolant choice may play a key role in machined surface integrity by changing the depth of the plastically deformed layer and localised deformation in the machined microstructure may provide nucleation sites for martensite transformation, which is beneficial for induction hardening.

8.1 High-Temperature Compression Testing

Surface integrity metrics such as surface roughness, diameter and circularity are regularly used to classify the quality of machined holes [99, 33, 100]. By varying machining parameters it is relatively straightforward to optimise a component for these metrics through industrial machining trials, particularly when a Design of Experiments methodology is employed to greatly decrease the number of required experimental runs. Measurement systems are readily available and often require no sectioning or workpiece preparation to use. Conversely, it is much more challenging to optimise the machined surface and sub-surface microstructure as

this level of characterisation requires extensive workpiece preparation and time-consuming analysis techniques, which industrial manufacturers would prefer to avoid. Furthermore, in many applications microstructural changes are not an important factor, since the holes are unloaded during operation. As a result, research surrounding the evolution of the machined microstructure in drilled holes is limited and common industrial practice for crankshaft design does not include considerations for the impact of the machining operation beyond the use of a surface roughness factor [101]. Yet microstructural evolution of the machined near-surface layer induced by combined thermo-mechanical loading during drilling is a key factor in surface integrity and changes to surface hardness and residual stress contribute heavily to fatigue life.

The drilling process leaves behind a plastically deformed layer that has experienced a combination of grain refinement and distortion. The depth and composition of the plastically deformed layer is governed by the rate of deformation, magnitude of deformation, and quantity of heat generated. But conventional machining trials for a given tool and application generally vary cutting speed, feed rate and lubricant. Complex interactions exist between these parameters, for instance, an increase in cutting speed increases the rate of deformation but also encourages heat generation. It is proposed that to better understand the mechanisms behind the generation of the machine-affected layer, the mechanics should be reduced to the fundamentals of deformation temperature, strain rate and strain. The behaviour of the workpiece material under these changing conditions can be characterised through controlled deformation experiments. This data may then be used to further understand the complex machining-affected layer discovered in drilling and burnishing trials. High-temperature compression testing of small samples allows deformation conditions to be precisely controlled and offers insight into how the material responds to challenging load conditions.

Simulation of the deformation behaviour of materials is regularly required by both industry and academia. Flow stress data can be used to understand the force required to shape materials and analyse phenomena such as strain rate sensitivity and strain hardening. Microstructural analysis can be used to optimise deformed microstructure for specific applications where certain material properties are required. Conducting these tests at elevated temperatures using specialised equipment allows high-temperature processes such as forging to be simulated. It is proposed that these testing methods could also be applied to enhance understanding of the effects of temperature on deformation mechanics and post-machined surface integrity of AISI 4140 steel.

The various test methods for hot deformation include: rolling mill, torsional, plane strain compression (PSC) and Axi-symmetric compression testing. Rolling mill and torsional tests are not applicable in this scenario as they are ineffective in replicating the deformation characteristics of the machining process: namely strain rate and geometry of the plane of

maximum shear stress. Axi-Symmetric testing involves the compression of a small cylindrical specimen by two flat compression platens and is commonly used to replicate the forging process. The relatively small contact area reduces the machine load required to deform the material. Due to frictional forces at the platens barreling may occur, whereby the surfaces in contact are unable to deform and deformation is concentrated in the centre. Steps can be taken to reduce barreling, but it is difficult to mitigate entirely. PSC testing utilises a geometry that confines flow in parallel to a specified plane, with strain in one coordinate assumed to be zero. PSC is commonly used to replicate the rolling process, which itself imposes plane-strain conditions [102]. Frictional effects are much lower than Axi-symmetric testing and barreling is mitigated. Plane strain conditions also simplify finite element analysis. For this reason plane-strain compression testing was originally chosen as the specimen geometry. During testing it was discovered that the force required to deform a PSC sample of this material at lower target temperatures was approaching the machine limit. Axi-Symmetric testing was subsequently used to characterize behaviour below these temperatures. An illustration of the geometries of the two specimens alongside their positions relative to the compression platens is shown in Figure 8.1.

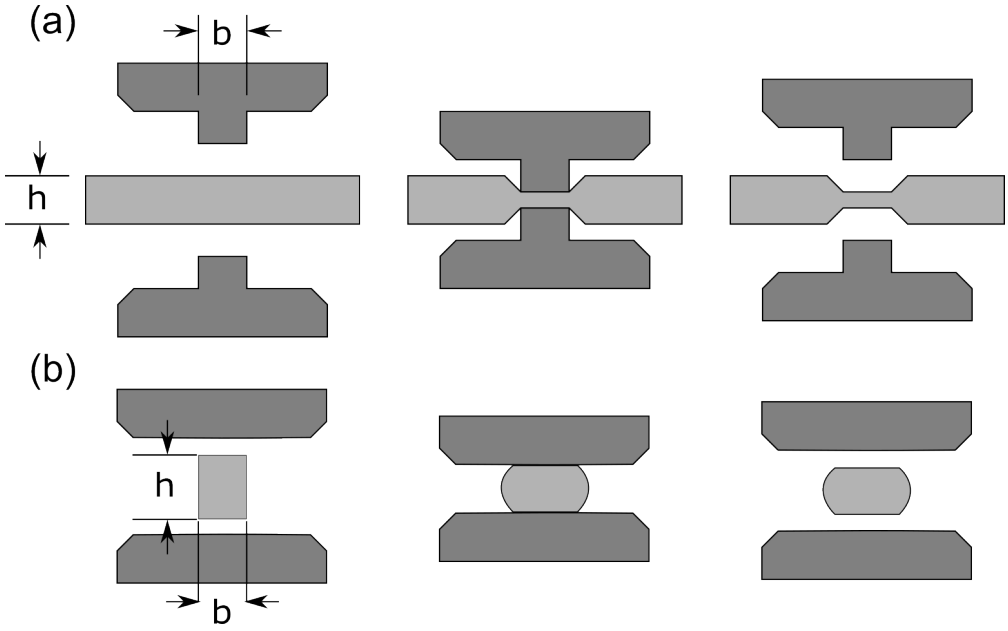

Figure 8.1: (a) PSC and (b) Axi-Symmetric specimen deformation cycle with upper and lower platens compressing the specimen in the centre before retracting to leave a deformed specimen

The undeformed areas of the sample constrain the majority of breadth spreading that would otherwise occur. Any spreading that does occur can be accounted for during post-processing of the force data by measuring the deformed specimen width as outlined in the best practice guides [103, 104].

8.2 Experimental Method

Recommended best practice guides for PSC and Axi-Symmetric Testing authored by experts in the field were followed to minimise uncertainty in the testing [104, 103]. All samples were extracted from the same billet of as-rolled 4140 steel and the machined samples were inspected to ensure the surface roughness was within tolerance prior to testing. The complete specification of the test machine and method of operation, including preliminary setup procedures is outlined in Section 4.2. A hole was drilled into the center of all samples, into which a Type N thermocouple was inserted to monitor and validate the sample temperature during heating and deformation. Strain rates between $19s^{-1}$ and $0.1s^{-1}$ were used with sample temperatures ranging from 400°C to 875°C to determine the temperature-dependent flow stress behaviour of the material.

8.2.1 TMC Test Cycle Design

The processing route used in this study was designed to emulate a single deformation pass at an elevated temperature. This is illustrated in Figure 8.2. The test begins with controlled heating at 10°C/s to the target temperature in the Fast Thermal Treatment Unit (FTTU), after which the specimen is moved into the furnace. Unless otherwise stated, the specimen is then held in the furnace for a dwell time of 120 seconds to ensure homogeneous sample temperature. Deformation takes place inside the furnace at the target true strain rate, during which the temperature sharply rises due to adiabatic heating under deformation. The sample is then retracted out of the furnace into the FTTU for cooling. Forced mist cooling was used to simulate the effect of machining coolant and was sufficient to reduce temperature at a rate greater than the critical cooling rate for this material. An assessment was made that air cooling would be insufficient to replicate the effects of machining, since in machining the deformed surface is cooled rapidly by contact with high pressure coolant. As such, forced mist cooling was selected. The cooling rate was set above the critical cooling rate for this material as derived from the TTT diagram shown in Figure 8.20.

8.2.2 Sample Analysis

For the purposes of analysis, specimens were sectioned along a diametrical plane, perpendicular to the compression direction. Deformed samples were prepared for Light-Optical Microscopy and hardness analysis using the preparation procedure outlined in 4.4. Optical micrographs were captured at various magnifications using a Nikon LV150N Bench-Top microscope. Samples were examined at the platen contact faces, in the center and at the left and right edges. Only samples deformed to the same total true strain were compared, due to the expected change in grain refinement at different strains. Hardness testing was conducted on a number of samples at the same locations as the optical micrographs using a Durascan G5 Microhardness test machine. Microhardness testing was deemed suitable because the

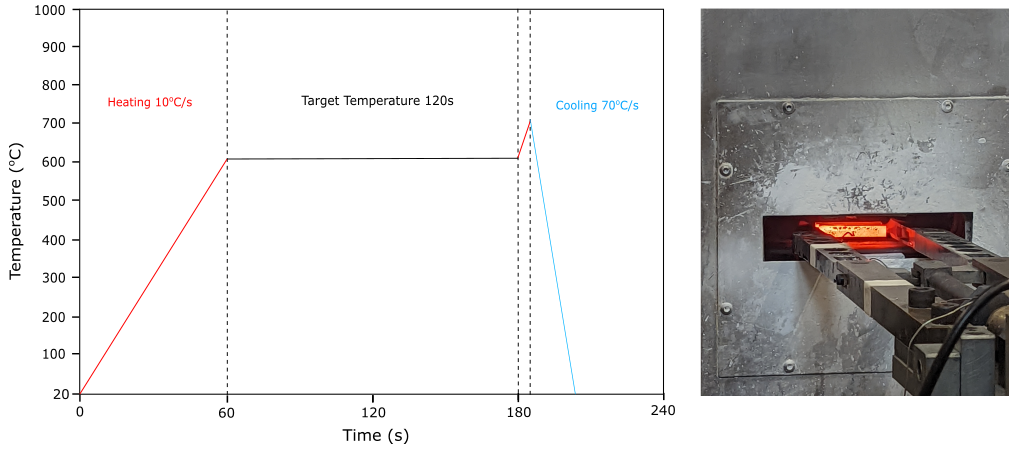

Figure 8.2: Typical TMC processing profile with exaggerated deformation time to highlight temperature rise, alongside an image of a specimen during heating

sample was expected to be approximately homogenous within the inspected regions. Samples were conducted at HV0.1 with a 1N load. Hardness was calculated using the measured indent diameter from the optical image.

8.3 Results

8.3.1 Test Specimens

All experiments were conducted on AISI 4140 steel as this is the material that machining trials were performed on. Test specimens were machined from the same batch of as-rolled steel billets that machining trials were performed on. To identify any discrepancies in results due to grain refinement during rolling, test samples were extracted in two perpendicular directions for preliminary testing, as shown in Figure 8.3.

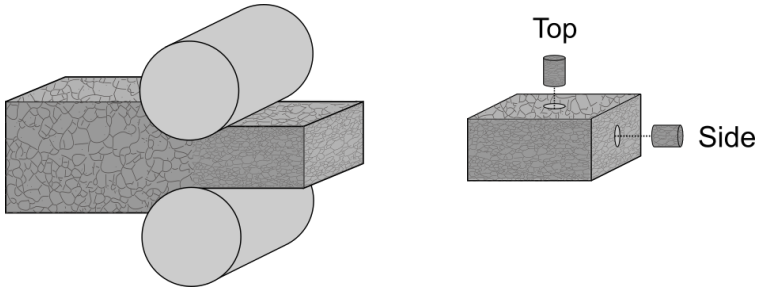

Figure 8.3: Sample extraction orientations relative to expected grain refinement directions with labelled orientations

Eight specimens in total were extracted, four in each direction. Each orientation was deformed at a temperature of 600°C and strain rates of $1s^{-1}$ and $10s^{-1}$. 600°C was chosen as it is just below the austenite transition temperature (AC1). Heating the specimen to above AC1 would change the flow behaviour as the high levels of strain in the rolled martensite crystal

structure would be relieved, leaving a softer austenite microstructure. Conversely, if temperatures were too low it was hypothesized that the unidirectional effects of grain refinement due to rolling would be less prominent, by means of reduced thermally activated dislocation motion [105] and therefore less grain boundary strengthening. Strain rates would ideally have been raised further to maximize strain rate sensitivity effects, however the machine is not capable of deforming high-strength steel at strain rates above those used in this work [106].

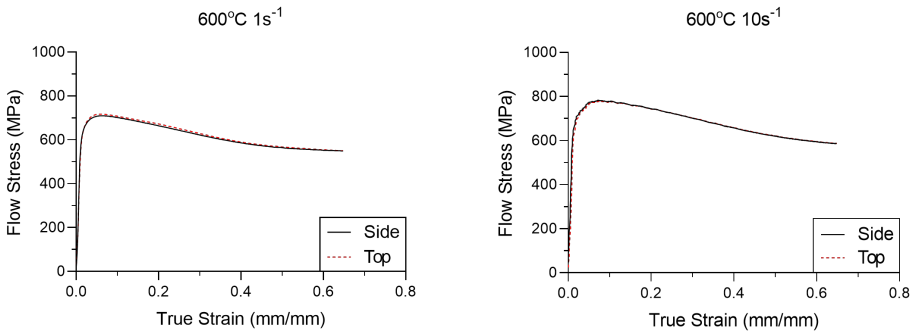

Figure 8.4: Flow stress curves for test samples at strain rates of $1s^{-1}$ and $10s^{-1}$

The resultant flow stress curves are shown in Figure 8.4. Flow behaviour was identical for both orientations tested at both strain rates in both the elastic and plastic regions. The two orientations could have exhibited similar strength with differing grain sizes if the refined grains were beyond the Hall-Petch limit. The reduction in strength of refined grains above this limit is due to the onset of grain boundary sliding. This behaviour is demonstrated in Figure 8.5, adapted from [107], where a sharp drop off in hardness is exhibited as a nanocrystalline structure is achieved. Literature suggests a grain size for this material of 21μm and this was further verified with optical microscopy as shown in Figure 8.6. This is well above the limit for Hall-Petch inversion [5] so it can be assumed that this effect has not occurred here.

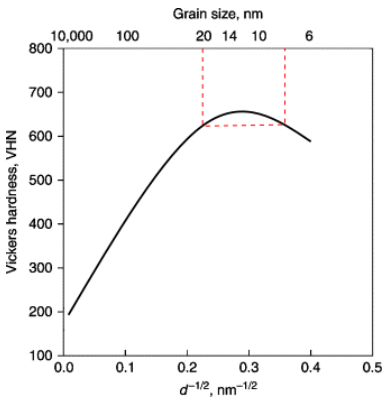

Figure 8.5: Hall-Petch relationship of nanocrystalline materials, adapted from [107] with red lines representing areas of dissimilar grain size with identical hardness properties

Figure 8.6: Optical micrograph of undeformed material for grain size measurement

Other research suggests a decreased effect of grain boundary strengthening at higher temperatures, possibly due to an increase in stacking fault energy (SFE) [108]. The test was repeated at 400°C and the results were similar. Therefore, it could be concluded from these tests that the prior material processing had produced a reasonably homogeneous microstructure with no significant directional strength. With the insignificance of sample orientation verified, testing could be initiated.

8.3.2 Plane Strain Compression

Initial investigations were conducted using Plane Strain Compression test samples since this test regime is regularly used to replicate the rolling procedure, which is comparable to the contact between the drill margin and the hole wall during drilling. The first specimen was deformed at a strain rate of $10s^{-1}$ and temperature of 650°C since this is close to but does not exceed the austenisation temperature for this material. During the test cycle, the load required for deformation was larger than expected and was approaching the limit of the equipment. A clear shear band was also visible across the deformed specimen along the angle of maximum shear stress (Figure 8.7).

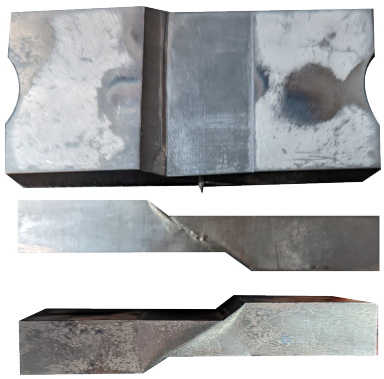

Figure 8.7: Post-deformation condition of two specimens deformed at 650C

The cause of the failure mode was unclear. The test was repeated at a lower strain rate of $1s^{-1}$. The deformed loads were still very high and the specimen again failed along the angle of maximum shear stress. A further sample was deformed at 650°C after holding the specimen at 1150°C for 5 minutes to allow full austenisation. This was performed to verify

if the failed tests were a result of the equipment setup or the material properties. This test resulted in the characteristic deformation cycle, without a shear band failure. The flow stress curves of the two samples deformed at 650°C with and without a prior austenisation step are shown in Figure 8.8. The figure also includes the result for an Axisymmetric compression test performed at the same temperature later in the experimental trial.

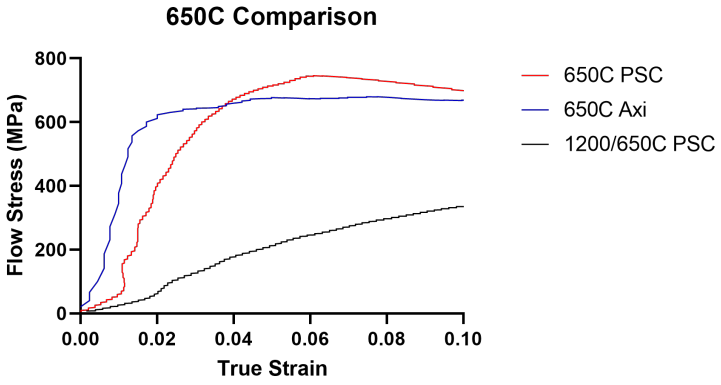

Figure 8.8: Flow stress curves for austenitised and as-rolled test samples at an initial deformation temperature of 650°C

The initial rise in flow stress at low strain levels for the ferritic-pearlitic samples is much greater than the austenitised sample. They also exhibit a characteristic flow stress curve where initial hardening is followed by a plateau. The flow stress for the austenitised sample rises steadily across the whole deformation cycle. A further test was performed at 875°C without a 5-minute austenisation treatment to assess the deformation characteristics of the material at just above the transition temperature. The sample was held at 875°C temperature for only 10 seconds and was expected to have a three-phase ferritic-pearlitic-austenitic microstructure during deformation. This test was used to replicate the influence of short-term high temperatures at the tool-workpiece contact. The resultant flow stress curves during deformation at 650°C and at 875°C are shown in Figure 8.9.

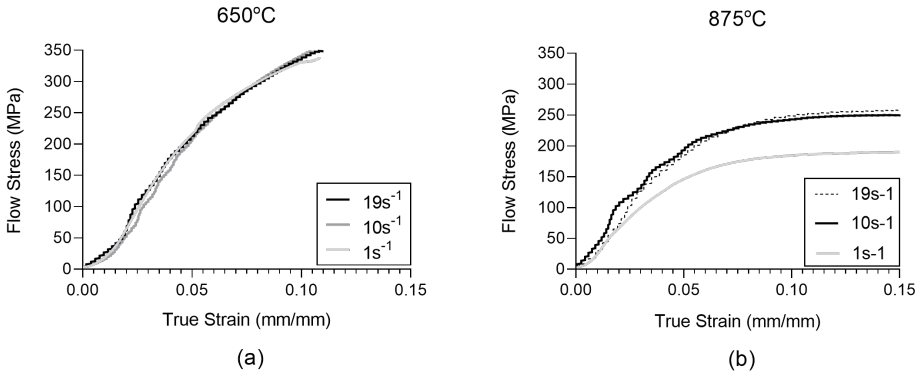

Figure 8.9: Flow stress curves for austenitised test samples at different deformation temperatures and strain rates

Despite the expected incomplete austensation, the flow stress for the 875°C sample was significantly lower. Interestingly, the 650°C fully austenitised sample did not exhibit any change in flow stress with strain rate, whereas flow stress was significantly lower at the low strain rate for the partially austenitised sample. Furthermore, at 0.1 strain the flow stress of the austenitised 650°C sample was still rising, whereas the flow stress of the partially austenitised 875°C sample had begun to level off.

Whilst austenisation reduced the deformation loads to within the limits of the machine, an austenitised microstructure is not representative of the crankshaft drilling operation, which is conducted in the as-rolled ferritic-pearlitic condition. There was no evidence of martensite formation in prior drilling trials, which suggests that under the conditions used, there was either zero or limited austenisation of the workpiece during the drilling operation. It was decided that all further testing would be conducted below AC1 on Axi-Symmetric test specimens which are much smaller and require a lower load to achieve the same level of stress within the sample.

8.3.3 Axi-Symmetric Compression

A best practice guide specific to Axi-Symmetric Compression Testing was used as a basis for this testing to minimise error [103]. Samples were deformed across strain rates of $1s^{-1}$ and $10s^{-1}$ and range of temperatures below AC1 in 50°C increments (Figure 8.10). For all

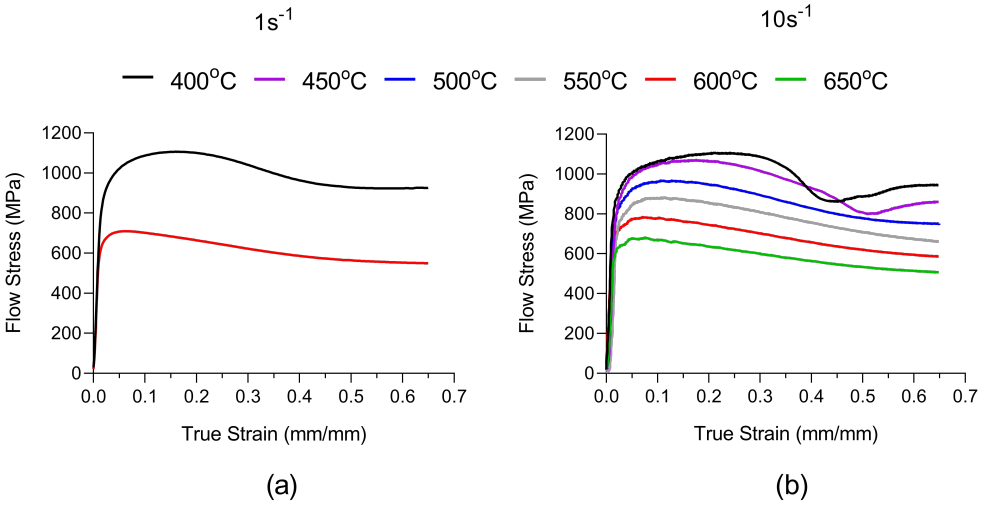

Figure 8.10: Flow stress curves for test samples deformed at (a) 1s-1 and (b) 10s-1 at various initial temperatures

temperatures and strain rates there is an initial linear region of elastic deformation where flow stress increases monotonically with true strain up until a yield point. This yield stress is similar for all temperatures. A period of strain hardening follows, where the flow stress required to continue plastic deformation increases with strain. Strain hardening then reduces

and eventually drops to zero at which point the flow stress begins decreasing up until the end of the test. Two specimens deformed at $10s^{-1}$ and temperatures of 400°C and 450°C exhibit a sudden decrease in flow stress at 0.35 and 0.45 strain respectively followed by a recovery to the initial path. The tests were repeated and the behaviour did not change. This sudden drop in stress is not present for the 400°C specimen deformed at a lower strain rate of $1s^{-1}$. The drop in flow stress initiated at a lower strain for the colder sample. Initial inspection of these two specimens identified a crack across the thermocouple hole. Figure 8.11 presents the direct effect of strain rate modulation on the flow stress curve at two temperatures. The graphs cease at 0.3 strain to exclude the period of sudden stress decrease associated with specimen cracking.

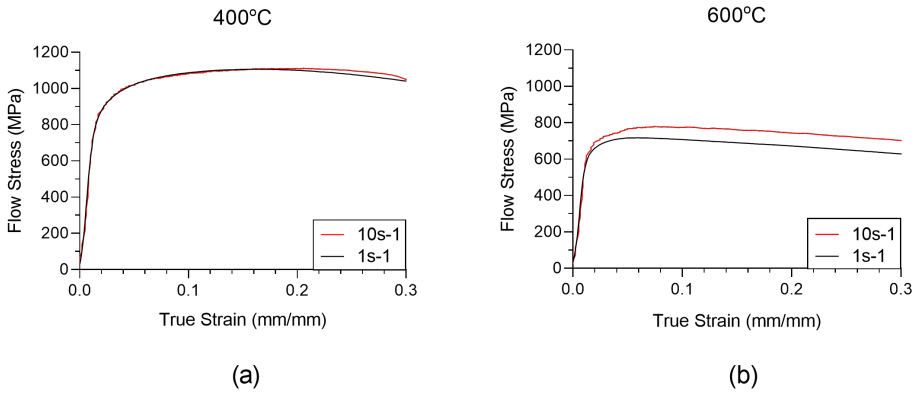

Figure 8.11: Flow stress curves for test samples at different deformation temperatures and strain rates

At 400°C the impact of strain rate on the flow stress curve is negligible up to 0.3 strain. However, at 600°C a higher rate of deformation increases the flow stress required to continue deformation. It must be noted that the 400°C and $10s^{-1}$ curve may have been influenced by microstructural effects that preempt the sudden drop in flow stress seen in Figure 8.10.

It is important to consider the generation of heat within the material during deformation. Adiabatic heating is a key characteristic of machining operations. This can be quantified by calculating the change in temperature at the thermocouple between the start and end of the compression cycle. The temperature rise during deformation is plotted against the initial temperature for each strain rate in Figure 8.12.

There is a quasi-linear decrease in temperature rise during deformation as the initial temperature rises. Temperature rise during deformation also increases with strain rate. The temperature rise curves of the three strain rates also appears to converge as the initial temperature increases. It is also important to consider how heat generation progresses with strain. Figure 8.13 tracks the change in internal temperature as strain increases for various initial temperatures and a strain rate of $10s^{-1}$.

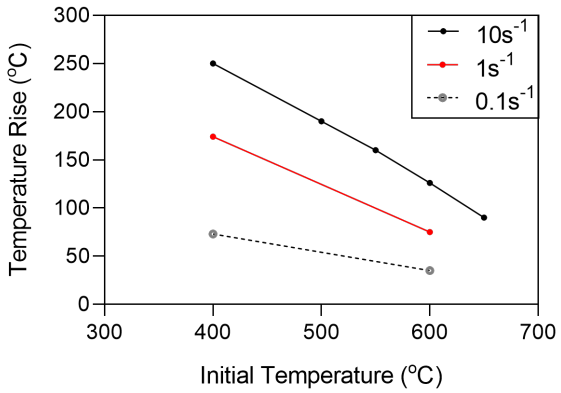

Figure 8.12: The temperature rise during deformation with varying initial temperature and strain rate

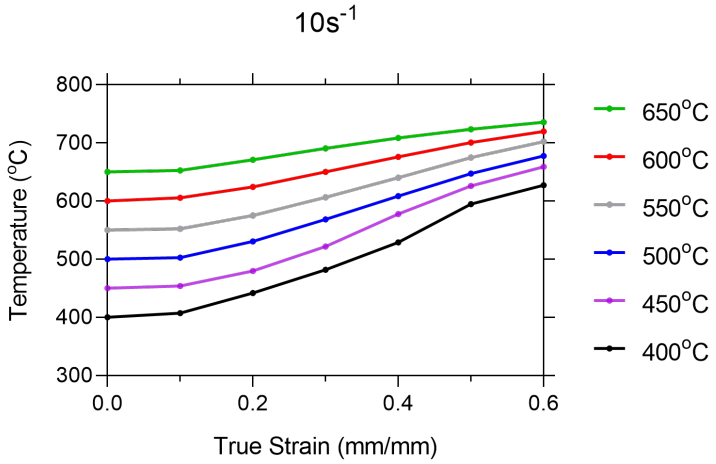

Figure 8.13: The rise in temperature measured at the centre of the specimen throughout deformation at $10s^{-1}$ across all temperatures

Temperature rise during deformation for all initial temperatures is minimal up to 0.1 strain, followed by a sharp increase until 0.5 strain where temperature begins to level off. The specimen internal temperatures begin to converge at higher strains. The influence of strain rate on sample temperature was further investigated. The evolution of temperature with strain is plotted for three strain rates in Figure 8.14.

At a strain rate $0.1s^{-1}$, the temperature profile during deformation was similar regardless of initial temperature. The total temperature rise was slightly higher for the colder specimen, with a sharper initial rise up to 0.1 strain. When strain rate was increased to $1s^{-1}$ the 400°C sample featured a much sharper rise in temperature at low strain before levelling at high strain. The final temperature delta for the $1s^{-1}$ samples was smaller than the $0.1s^{-1}$ samples. This may be a result of the convergence of temperature identified in Figure 8.13. At $10s^{-1}$ the temperature profile increased in gradient yet again, resulting in the smallest final temperature delta. Increasing strain rate increased the temperature rise during deformation

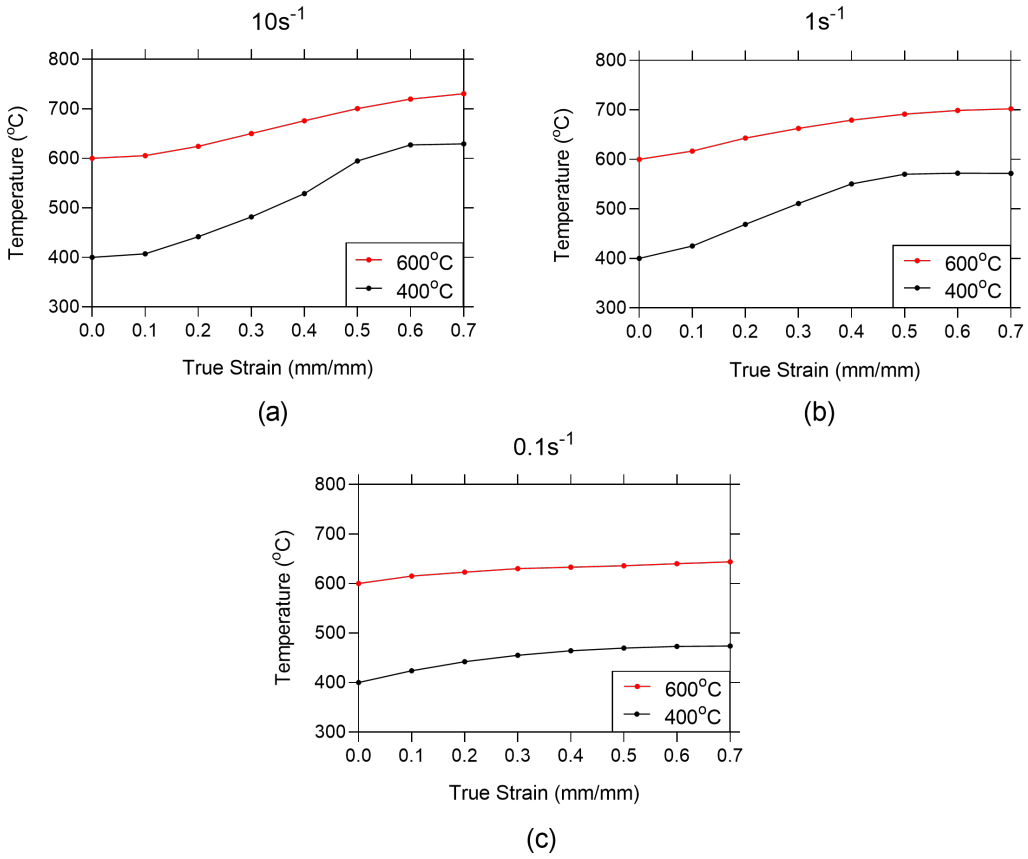

Figure 8.14: The change in temperature during deformation at $0.5s^{-1}$, $1s^{-1}$ and $10s^{-1}$, and starting temperatures of 400°C and 600°C

and the effect was most prominent for the lower temperature sample.

The influence of strain rate on specimen heating can be analysed by comparing specimens deformed at the same temperature and different strain rates. In 8.15 temperature rise is compared during high and low strain rate deformation at two different starting temperatures. For both starting temperatures, the temperature of the low strain rate sample rises faster initially before being overtaken by the high strain rate sample at approximately 0.4 strain.

8.3.4 Microstructural Analysis

Optical micrographs of the deformed microstructure were captured for most test specimens. In this section, samples that exhibited notable microstructural features are reported.

A white region with a central horizontal crack was identified at the center of sample 1. Sample 1 was deformed at 650°C and a strain rate of $10s^{-1}$. The band of white microstructure is approximately 1.5mm across and 60μm thick. The crack is located to the left side of the white region and is approximately 200μm long with visible asperities. The white region is surrounded by a band of dark microstructure that is approximately 600μm thick and

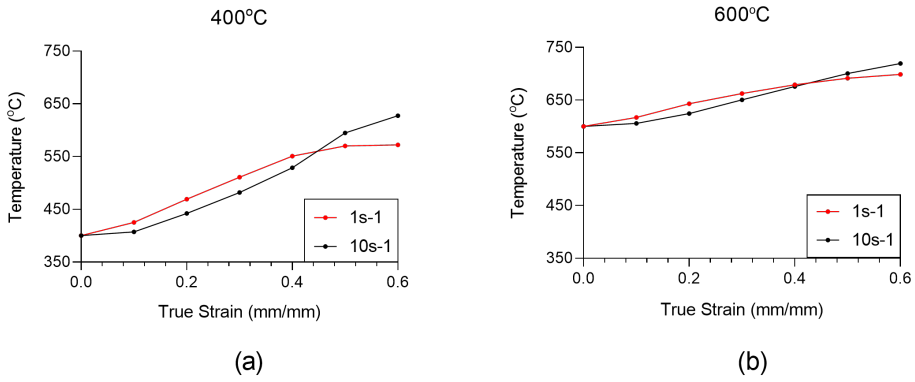

Figure 8.15: The rise in temperature measured at the centre of the specimen throughout deformation at two starting temperatures and high and low strain rates

resembled strained pearlite. No further abnormal microstructural features were identified elsewhere. No anomalies were identified in the flow stress data for this sample. A similar feature that was smaller in size was seen in sample 2, which was deformed at 600°C. In the sample deformed at 550°C no white or dark region was identified. During the compression

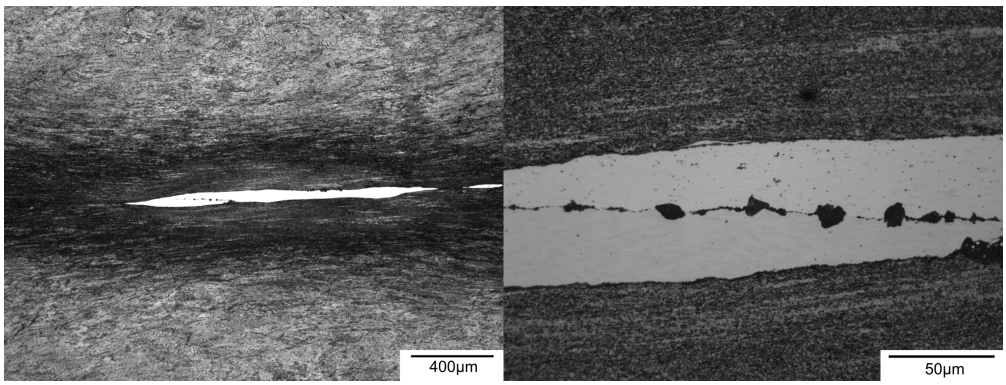

Figure 8.16: Post-deformation micrographs of Specimen 1 at two magnifications showing a white region of microstructure in the center with a visible crack

test at 400°C, there was a sudden drop in flow stress followed by recovery, as seen in Figure 8.10. Initial visual inspection of the sample identified sliding deformation across the 45-degree line of maximum shear stress. A micrograph of the deformed specimen is shown in Figure 8.17. The center exhibited a wide band of unresolved white microstructure approximately 160μm thick bordered by dark bands of swept pearlite. Toward the edge of the sample the white region disappears and the swept microstructure becomes more prominent. Across the whole sample the dark bands of deformed pearlite transition smoothly into the global deformed ferritic-pearlitic microstructure.

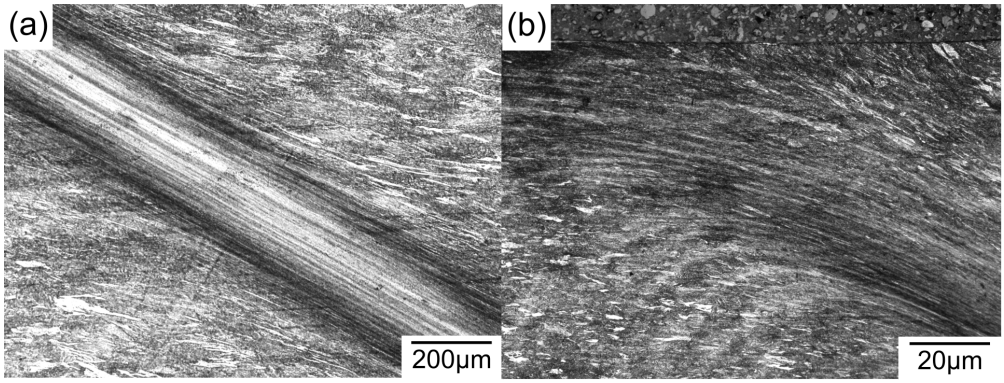

Figure 8.17: Post-deformation micrograph of the (a) center and (b) edge of a test sample that was compressed at 400C and exhibited a sharp drop in flow stress at moderate strain

8.3.5 Hardness

The hardness of samples deformed at $10s^{-1}$ was measured at locations in the center and four edges. The average sample hardness decreased with increasing deformation temperature across all measurement positions (Figure 8.18(a)). Maximum hardness was measured at the center of all samples, with a slight reduction toward the edge which is the cause of the measurement variation. Particularly large variation was noted in samples that exhibited concentrated shear bands across the specimen following deformation (Figure 8.18(b)). A slight increase in visible grain refinement was noted in samples that exhibited greater hardness.

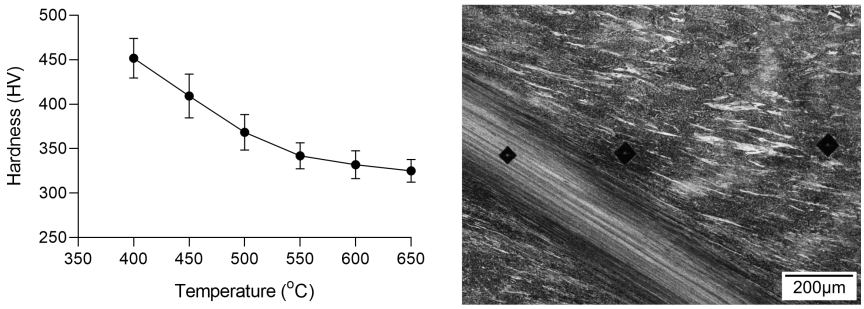

Figure 8.18: (a) Change in hardness with increasing deformation temperature, measured at various positions around the sample (b) Micrograph of the center of a test specimen following hardness testing

8.4 Discussion

8.4.1 Plane-Strain Compression Testing

A limited number of trials were performed with the PSC sample type due to the high deformation loads required to deform the large contact area. This testing method is commonly

used to replicate forging and rolling at high temperatures, with subsequently lower required deformation loads. The high required loads were approaching the limits of the machine. As a result PSC testing was used to study the deformation behaviour of 4140 steel solely around the austenite transition temperature.

Austenisation of the test specimen prior to deformation drastically reduced strain hardening and mean flow stress compared to the ferritic-pearlitic condition. This can be explained by the reduced resistance of austenite to deformation compared to ferrite and pearlite [109]. Whilst the sample deformed at 875°C after a short holding time exhibited reduced flow stress compared to the 650°C fully austenitised specimen, it demonstrated increased strain rate sensitivity (SRS). The cause of this SRS was initially unknown. Studies have highlighted reduced SRS within austenitic steels compared to ferritic and martensitic alloys [110], but there is limited information surrounding the change in SRS with temperature.

Axi-Symmetric compression testing in the ferritic-pearlitic condition conducted in this project identified a similar increase in SRS with temperature (Figure 8.11). If ferrite and pearlite regions remained in the sample prior to deformation they could encourage the SRS behaviour, but it is unlikely that sufficient levels of ferrite and pearlite microstructure were remaining at 875°C to achieve the notable SRS. Full austenisation has been seen after 3 seconds at 875°C in an alloy of similar composition [44]. Furthermore, following a controlled heat treatment at 900°C for 120 seconds, austenite grain size of 4140 Steel was sufficiently large to suggest that almost complete austenisation had taken place [5]. Even with only partial austenitisation, deformation would likely preferentially occur in austenite, limiting the contribution of ferrite and pearlite. During deformation of a two-phase microstructure consisting of ferrite and austenite, plastic strain concentrated in the austenitic regions due to its lower hardness and increased ductility [111].

It was unknown whether deformation-induced martensite transformation may also have contributed to strain rate sensitivity. Whilst the transformation of austenite to martensite most commonly occurs under rapid cooling, it can also be encouraged by deformation through a transformation-induced plasticity (TRIP) effect, giving rise to enhanced strain hardening. However, research suggested that the formation of deformation-induced martensite was restricted at higher strain rates, due to adiabatic heating and an associated higher energy barrier to deformation [112]. When subjected to elevated strain rates, the combined effects of local adiabatic heating and the latent heat released during phase transition elevate the local temperature. This temperature rise can impede the phase transformation process [113]. Globally, this restricts the phase transformation rate at higher strain rates, leading to a notable decrease in strain hardening. Strain-induced martensite formation could not have caused the SRS behaviour, as it is clearly restricted by increased strain rates. Austenitic steels, which consist of metastable austenite at lower temperatures, have been shown to

exhibit SRS at room temperature [114], so it is unlikely that the lack of SRS in the 650°C was due to insufficient thermal energy. It was most likely driven by an increased austenite grain size due to the 5 minute holding time. A coarser microstructure contains fewer grain boundaries to restrict dislocation motion and thus strain hardening and SRS effects are reduced.

No retained austenite was visible in the micrographs of the austenitised samples. Austenite is stable above the critical eutectoid temperature. The addition of certain alloying elements can improve the stability of austenite at lower temperatures and even lead to the existence of retained austenite at room temperature. The application of compressive stress has been found to reduce the stability of austenite in high-carbon steels [115]. With increasing compressive stress, the volume of retained austenite is reduced and replaced with martensite, which explains the absence of any retained austenite.

Studies have suggested that deformation of austenite generates an increased number of nucleation sites for martensite formation. The post-deformed microstructures of all of the austenitised 650°C and 875°C samples shared similar martensite grain sizes, regardless of the final true strain. This may be due to the relatively low maximum strains used in the study. It was also thought that the martensite volume fraction would be enhanced by increasing austenite grain size. Austenite grain size increases with time and temperature, so the heat treatment of 5 minutes at 1200°C will have generated a larger austenite grain size than 10 seconds at 875°C [5]. A larger austenite grain size restricts the diffusion of carbides, by forcing the carbon to travel further to reach a reduced number of nucleation sites at the grain boundary. This would typically increase the propensity for martensite formation under cooling, however no appreciable increase in martensite refinement was seen.

8.4.2 Axi-Symmetric Compression Testing

The flow stress curve is governed by the competing effects of strain hardening and dynamic softening, driven respectively by dislocation nucleation and annihilation. The flow stress required for deformation rises with strain hardening and reduces with dynamic softening. During the initial stages of deformation, there is a significant accumulation of dislocation density, leading to strain hardening. However, with continued deformation and the resultant increase in temperature, this is increasingly counteracted by the annihilation of dislocations, resulting in a discernible peak in the stress-strain curve. From this point forward dynamic softening outcompetes strain hardening, resulting in a steady decrease in flow stress.

The flow stress curves reduced almost linearly in magnitude across all strain levels with increasing deformation temperature. The elastic behaviour and initial strain hardening rate during early-stage plastic deformation are comparable across all temperatures and strain rates. 4140 steel is a high stacking fault energy (SFE) material. In crystalline materials,

stacking faults are defects which occur when the regular stacking sequence of atomic planes is disrupted. This influences the material's ability to plastically deform. In high SFE steels, hardening is enhanced by the difficulty in activating deformation twins in refined grains due to the increased critical twinning stress [116]. At higher temperatures the hardening ceases sooner, resulting in a lower flow stress for the remainder of the test. The rate of decrease in flow stress after the peak is also comparable across all specimens, as evidenced by the parallel decrease at the latter stages of all flow stress curves. This means that despite changing temperatures, the competition between strain hardening and dynamic softening remains similar. Dislocations are increasingly mobile at higher temperatures and can more readily move past obstacles such as solute atoms, other dislocations, or precipitates, which facilitates plastic deformation. Dislocation annihilation due to dislocation climb and cross-slip is also accelerated at high temperature [117]. This explains the reduction in cutting forces at high temperatures seen in the literature [35].

A sudden drop and then recovery in flow stress at moderate strain was noted in samples deformed at 400°C and 450°C with a strain rate of $10s^{-1}$. The drop in stress occurs at a higher strain for the hotter sample and is no longer present at 500°C. This behaviour is also not present when deforming at $1s^{-1}$. Interestingly the recovery in flow stress is sharp and returns the flow stress curve to its approximate original trajectory. Both samples exhibited a shear band along the 45-degree line of maximum shear stress. It is believed that the thermocouple hole acted as a stress concentration in the same manner as the failure in the Plane Strain Compression samples. As a consequence of the cylindrical sample geometry, the sample appears to have reformed following fracture to allowed continued homogenous deformation. Since only the center portion of the PSC samples was deformed, they were unable to recover in the same way.

Thermal hardening behaviour has been identified at low temperatures (less than 400°C) in other materials, whereby microstructural evolution at elevated temperatures has increased the flow stress required for deformation [118]. Tests could not be completed at such low temperatures for this material due to the discovered fracture failure mechanism. But, localised workpiece temperatures in the near surface during drilling are expected to be higher than the minimum test temperature, so this was not seen as a limitation [35].

8.4.3 Friction

A frequently reported limitation of Axi-Symmetric compression testing is the barreling of test specimens. Barreling occurs when friction limits lateral strain at the platen-specimen contact and strain is accommodated by the center of the specimen, resulting in a larger diameter center [119]. Friction may cause overestimation of flow stress due to the requirement for the system to overcome the sticking friction at the contact as well as deform the material.

But, this may be counteracted by a reduction in flow stress due to heat generation. Although boron-nitride lubricant spray was used, high temperatures and contact loads increased the likelihood of sticking friction. Therefore, it was important to consider and identify occurrences of high friction during the test runs. Barreling phenomena can be used to assess the difference in friction between test runs. This was achieved by calculating a friction factor for each specimen using Equations 8.1 and 8.2 [120]:

$$m = \frac{3\sqrt{3}}{2}\frac{\bar{R}}{H_1}\frac{b}{6-b} \tag{8.1}$$

$$b = 4\frac{\Delta R}{\Sigma R}\left(2\frac{H_1}{\Delta H} - 1\right) \tag{8.2}$$

where m is the friction factor, $\bar{R}$ is the average radius, H_1 is the deformed cylinder height, ΔR is the difference between maximum and minimum radius, ΣR is the sum of the maximum and minimum radius and ΔH is the change in height. The calculated friction factors for each test temperature are illustrated in Figure 8.19, where a higher friction factor indicates greater barreling. Barreling was comparable across all successful tests but increased slightly with temperature and strain rate. The friction co-efficient, μ is known to increase with

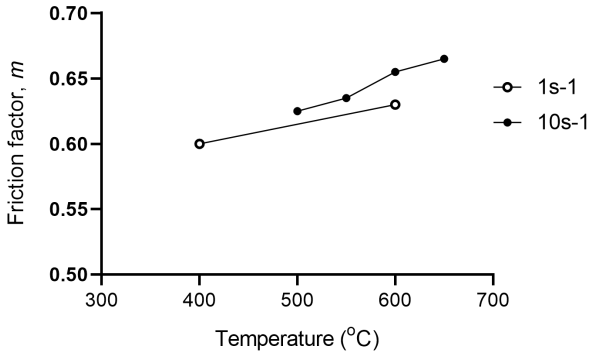

Figure 8.19: The evolution of friction factor with deformation temperature at high and low strain rates

temperature due to increased contact adhesion [85]. This explains the slight rise in barreling with increasing initial deformation temperature. Whilst variation in material properties across the sample height may also cause barreling, this is unlikely as the material was pre-tested for directionality, the samples were prepared at slow machining rates and they were held at the target temperature for 120s to allow temperature to equalise. Elastic springback and thermal contraction of the material may have introduced minor error in the sample height and radius measurements, since they were taken on cold specimens after removal from the furnace. This was deemed acceptable as comparison of friction was still possible

and full characterisation of friction was beyond the scope of this study. Furthermore, in-situ imaging/measurement was not possible due to the inaccessibility of the furnace.

The frictional heat is generated at a distance of half the sample height from the center and must first conduct through the sample before being registered at the thermocouple. As true strain increases, sample height and therefore conduction height decreases and any heat due to friction is more likely to increase the captured temperature. Because of this, the temperature gradient would be expected to increase with strain. It would also be expected that tests with high friction, characterized by greater barreling, would exhibit an increasing temperature gradient with strain. The absence of an increasing temperature gradient would then signify limited frictional heating. This was the case for the samples tested and the temperature rise in specimens must have therefore been dominated by adiabatic heating.

8.4.4 The influence of strain rate

Samples were tested at strain rates ranging from quasi-static ($0.1s^{-1}$) to dynamic ($10s^{-1}$) to understand the strain rate sensitivity of the material. Strain rate sensitivity was almost negligible at 400°C, but at 600°C flow stress increased with strain rate. During deformation certain modes of dislocation movement such as cross-slip are thermally activated. At higher strain rates the time for thermal activation is greatly reduced, which restricts dislocation motion. It is possible the 400°C sample did not have sufficient thermal activation energy for strain rate to have a significant effect. This would explain why strain hardening was only enhanced by strain rate for the 600°C sample. Interestingly the gradient of the flow stress curve following the peak was similar at high and low strain rates. For this to happen, a softening mechanism must have been encouraged to counteract the enhanced strain hardening. This softening behaviour could have been driven by greater sample temperatures.

The temperature rise during deformation was found to increase with strain rate for all tests and strain rate appeared to have a greater effect on temperature rise of the colder specimen. At $0.1s^{-1}$ (quasi-static) the temperature profile was almost identical for high and low temperature tests, whereas at $10s^{-1}$ there was a much greater temperature rise in the cold specimen. Furthermore, regardless of initial temperature, the $10s^{-1}$ sample experienced a slower temperature rise at the thermocouple at low strains, but then overtook the $1s^{-1}$ sample at higher strains. Because of the limited magnitude of barreling identified in the test specimens, as described in Section 8.4.3, it can be assumed that adiabatic heating is the dominant source of heat generation in the samples, with a limited contribution of platen friction. The results therefore indicate that increased strain rates generate greater adiabatic heating in the sample, that follows a negative skew with strain and exerts a greater influence at colder initial temperatures.

8.4.5 Adiabatic Heating

Adiabatic heating occurs when the energy used to deform a material turns into heat which cannot escape to the surroundings and therefore raises the temperature of the material. The compression test is conducted in a furnace that is held at the initial deformation temperature, which makes it an ideal scenario to investigate adiabatic heating, since heat is unlikely to transfer away from the sample at an appreciable rate. Samples were heated to and deformed at incremental temperatures up to but not exceeding the austenite transition temperature. The sample temperature was monitored during deformation via an embedded thermocouple and increased for all samples under deformation. The strain rate during deformation had a clear effect on the temperature rise, which increased as strain rate was increased from to $1s^{-1}$ to $10s^{-1}$ at a 650°C deformation temperature. This behaviour has also been noted in advanced high-strength steel alloys [121]. Studies also noted minimal changes as strain rate increased further toward machining rates and it is therefore reasonable to presume that the adiabatic heating generated in this study is representative of machining-induced deformation.

The slow initial rise in temperature during deformation may be due to poor heat transfer between the material and thermocouple wire, which improves after initial deformation. The temperature rise at medium strains is expected as deformation causes adiabatic heating of the material and frictional heat at the platens begins to transfer to the thermocouple. The temperature of convergence roughly coincides with the AC1 temperature of this material at 730°C. Differential Scanning Calorimetry analysis of Martensite-Austenite and Ferrite-Austenite transformations has identified clear endothermic peaks during austenisation, signifying that heat is absorbed during transformation [122]. Once deformation was sufficient to raise the temperature to AC1, heat flux at the thermocouple may have been reduced by austenisation of the nearby ferrite and pearlite, causing the temperature convergence seen here. Austenisation should be accompanied by a reduction in flow stress, due to the decreased strength of this phase, but no appreciable drop off in flow stress beyond that of recrystallisation is evidenced in the flow stress curves in Figure 8.10. But austenitisation may have been localised around the thermocouple hole and insufficient to yield a reduction in global flow stress. The cooling rate after deformation exceeded the critical cooling rate for complete martensite transformation and if austenisation had occured, martensite would have been evident in the post-deformation micrographs. LOM analysis of the 650°C sample revealed a white region of unresolvable microstructure in the center with a visible crack across it. This was also surrounded by a darker etched region. The white region in the 600°C sample was smaller and no such feature was identified in any of the colder tests. The white region is similar in appearance to the nanocrystalline martensite seen in white etching layer (WEL). WEL is commonly characterised as a region of ultra-fine grained brittle microstructure at the surface of machined materials [123]. WEL is also frequently seen adjacent to a darker layer [60]. Stress concentration at the thermocouple hole edges may

have concentrated deformation in the region and caused rapid plastic strain around the hole. This may then have caused localised adiabatic heating and subsequent phase transformation to austenite. Under rapid cooling, carbon would be unable to diffuse from the austenite, leaving a nanocrystalline martensitic structure as seen in the micrographs. This suggests that even at initial deformation temperatures below AC1, conditions can be such that without the application of external heat, localised adiabatic heating can cause local austenisation and subsequent martensite formation. This temperature convergence was not identified in samples deformed at $0.1s^{-1}$, which suggests that at slower deformation speeds adiabatic heat is able to distribute through the sample and prevent localised heating. It was not possible to remove the thermocouple hole as this was required to control the sample heating rate.

Phase transformations are an important factor in steel manufacture, since the properties of the material can vary significantly depending upon the dominant phase. The phase transformation behaviour of a steel alloy is primarily determined by the readiness of the alloy to permit the diffusion of carbon from the austenite phase. This can be visualised in a Time-Temperature-Transformation (TTT) diagram. The TTT diagram for 4140 steel is shown in Figure 8.20.

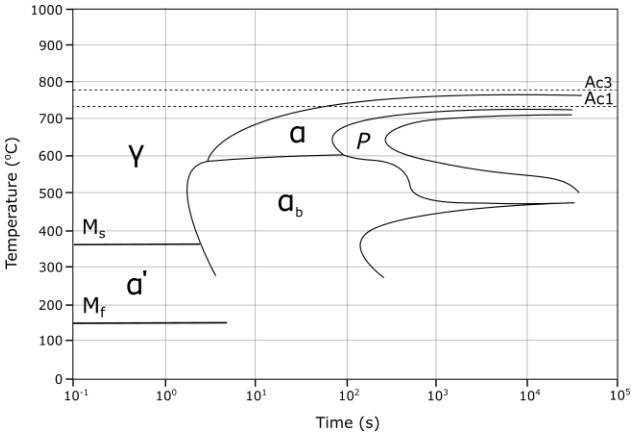

Figure 8.20: TTT Diagram for AISI 4140 Steel

4140 Steel is regularly selected as a crankshaft material for its high hardenability, or the ease of which a martensitic microstructure can be formed under cooling. Whilst this property is beneficial for generating a hard, wear resistance surface after induction hardening, it may make the material more prone to the formation of a white etching layer (WEL) during machining. The presence of a localised unresolvable white region in the microstructure of samples deformed at 600°C and 650°C gives an indication of the propensity for localised austenisation and subsequent transformation to martensite, provided cooling rates exceed the critical cooling rate for the material.

8.4.6 Oxidation Effects

Oxidation is a concern when conducting compression testing at elevated temperatures since oxidation typically alters the surface topography and decreases surface hardness. 4140 Steel has a high chromium content and chromium oxidises more readily than iron. Oxidation occurs more readily at higher temperatures and thicker oxide layers are formed on the material surface. Hao [124] verified this behaviour by measuring the mass gain of chromium steel over time at elevated temperatures and confirmed a strong temperature-dependence of oxidation. Whilst oxidation is a concern, Obadas [85] suggests that the effect of oxidation would be negligible at the temperatures and times used in this research. This is in agreement with the minimal change in macroscopic texture seen between the samples raised to 650°C and 875°C in Figure 8.21.

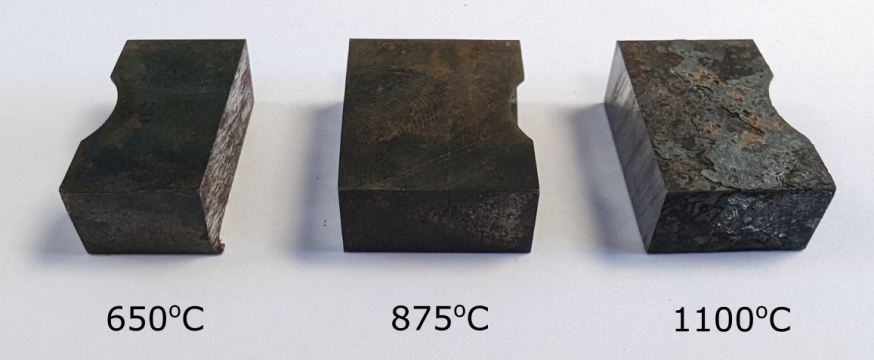

Figure 8.21: Undeformed sections of PSC samples that have been raised to various temperatures with high levels of oxidation visible at 1100°C. Samples are approximately 20mm in width

8.4.7 Implications for machining

If temperatures exceed the austenite transition temperature, AC1 and the heated area cools at a sufficient rate, then microstructural changes may occur. Evidence of transformation was not noted in the crankshaft samples assessed previously in this thesis, but these were machined with through-tool emulsion coolant, which is expected to limit temperature build-up in the workpiece. The use of alternative strategies such as Minimum Quantity Lubrication drilling may yield much higher temperatures. Zhu [35] utilized a prototype foil thermocouple system to evaluate temperature distribution across the cutting edge under drilling of Aluminium alloy using dry, air and MQL lubrication and varied cutting parameters [35]. Temperature across the cutting edge and cutting forces were both more sensitive to feed rate than cutting speed, which suggests that there was significant heat generation due to deformation. The thermal conductivity of aluminium is much greater than steel, so a greater proportion of the heat generated will conduct into the workpiece and chip and away from the tool. This, coupled with the increased energy required for deformation means that higher

temperatures would be expected in the tool when machining steels. Heat is also unlikely to conduct to the bulk material quickly and temperatures in the workpiece near-surface may even exceed the AC1 transition temperature. If this were to occur, the near-surface could be strengthened or weakened depending on the cooling rate that followed. If cooling is slow the refined ferrite and pearlite that was present after forging may be replaced by recrystallised ferrite and pearlite, in effect normalising and therefore weakening the microstructure. Conversely, if cooling is sufficiently fast, martensite may be formed. This would harden the near surface and be beneficial, provided tensile residual stresses were not generated. But, the regions that undergo martensite phase change may influence the neighbouring ferritic microstructure.

Altreya et al.[125] identified transformation induced deformation of ferrite in the production of Dual-Phase (DP) steels. A DP microstructure was generated by partial austenisation within the intercritical region at 750°C, 775°C and 800°C followed by quenching to generate hard martensite within a soft ferrite matrix. In the study, the volume expansion associated with austenite-martensite phase change was shown to induce short and long range deformation of nearby ferrite grains that decreased in magnitude with temperature. Kernel Average Misorientation of individual grains was calculated through EBSD mapping and used to quantify grain deformation. At an intercritical (IC) temperature of 750°C deformation frequently extended to the interior of ferrite grains, whereas at 775°C deformation was more isolated to the ferrite-martensite grain boundary. At an IC of 800°C deformation in the small quantity of remaining ferrite is almost entirely absent. These results suggest ferrite deformation isn't linked to martensite volume fraction.

This behaviour could be exhibited in 4140 Steel as it is capable of being heat treated to produce a Dual-Phase microstructure and is in fact often used in this condition if a balance of toughness and strength is required. The partial austenisation and quenching of a near-surface machined layer could feasibly generate a dual-phase microstructure with a strained ferrite matrix, depending on temperature. This would provide an associated decrease in strength and experience weakening. Since a high martensite volume fraction isn't necessary for this to occur, the depth of the transformed layer does not have to be large.

8.5 Concluding Remarks

The aim of this chapter was to investigate how material loading conditions including temperature and strain rate influence the deformation behaviour and post-deformation microstructure of 4140 steel. This study was specifically targeted at identifying the change in adiabatic heating and localised deformation during high speed compression, in order to better understand the conditions at the margin-wall contact during drilling.

The findings of this chapter revealed that the deformation behaviour of 4140 steel is highly sensitive to changes in temperature under high-speed compression conditions. Adiabatic heating during deformation was significant, and samples deformed at high temperatures demonstrated localised concentration of plastic strain and heat that was sufficient to induce phase change and the formation of heavily refined martensite. The deformation of the samples above AC1 also revealed that even under very short-term exposure to high temperatures, austenisation can be achieved. These findings are important for manufacturers because they indicate that under high-temperature conditions such as near-dry machining, localised heat generation may induce phase changes that are detrimental to fatigue life. It was previously thought that the surface would need to be held at elevated temperatures for this to occur, but results revealed that strain-induced adiabatic heating can be sufficient to induce this transformation, even at moderate strains.

This chapter also faced some limitations and challenges that need to be acknowledged. The material had a high propensity for brittle fracture at lower sample temperatures, so it was not possible to evaluate the behaviour below 400°C for Axi-Symmetric samples and 650°C for PSC samples. Although tests at 650°C indicated similar behaviour between the two sample types, it would have been useful to test the PSC specimens at lower temperatures to remove any barreling effects. Furthermore, studies on other materials have demonstrated flow stress inversion at 2-400°C, so testing below this temperature would have been beneficial, to identify if the same trend in flow stress is observed at low temperatures. The test is also designed to produce homogeneous strain throughout the sample, which is not entirely representative of the machining contact, where deformation is concentrated in small severely deformed layers. Future research is needed to address these limitations and challenges, as well as explore new avenues for further investigation. It may be beneficial to design a new sample geometry that introduces variable strain across the height to simulate the strain differential at the hole wall. It may also be useful to deform specimens at lower temperatures prior to austenisation and rapid cooling, to simulate the impact of drilling on the post-hardened microstructure at the oil hole surfaces.

Regardless of the limitations, this chapter has demonstrated that loading conditions, in particular temperature, have a significant impact on the deformation characteristics of 4140 Steel and may induce unwanted changes to the machined surface. In light of these conclusions, particular consideration must be given to the impact of adopting changes to the machining strategy that may generate increased workpiece temperatures.

Chapter 9

MQL Drilling

A well-implemented emulsion metalworking fluid strategy often provides manufacturers with multiple operational benefits including extended tool life, improved surface quality, and superior chip evacuation. Despite these positive benefits, with Net Zero looming, manufacturers are seeking alternative machining methodologies to meet their requirement of reducing embodied carbon. One such solution is the use of a Minimum Quantity Lubrication (MQL) strategy. MQL offers a reduction in coolant usage and its associated environmental impact.

During conventional emulsion drilling, large quantities of emulsion coolant in the region of 5-15% oil concentration are transported from an oil sump, through a filtration system and supplied at high pressure to the tool-tip. The used oil is then transported back to the sump to be reused, with some remaining on the machining swarf and inside the machine tool. The pumping system is energy-intensive, and large volumes of fluid are used in the process. Conversely, during MQL drilling, much smaller quantities of neat oil (20ml/hr) are mixed with air under high pressure and exit the tool tip in an atomised oil-air aerosol. The oil can be atomised in an external pump or internally above the spindle, depending on the system used. An external system is cheaper to implement and maintain, but there is an increased risk of fluid separation due to the distance between mixing and application. An internal system offers improved performance due to reduced separation, but requires significant investment and machine compatibility. Bio-derived oils such as soybean oil are frequently used as the lubricant medium and oil usage is significantly reduced compared to an emulsion coolant strategy. The associated energy expenditure of the pumping and filtration system is also greatly reduced. Furthermore, the oil often vaporises during cutting, reducing the need for disposal.

Significant amounts of research are available investigating the tool wear characteristics of MQL, but there are fewer studies surrounding surface integrity. While tool wear is extremely important, repeatable surface integrity and part quality are essential for safety-critical components such as the crankshaft. The research literature surrounding MQL machining of

high-strength, hard-to-machine materials was found to be particularly limited. This may be because MQL is compared most frequently to dry machining in the research literature, since it can offer an improvement in tool life without a significant increase in environmental cost, and these materials are almost never machined dry. Past research has consistently proven the superiority of MQL over dry machining and since operating without lubricant is not an option for deep hole drilling of automotive steels, it was not considered here. Instead, for industrial automotive research, MQL must be compared to emulsion metalworking fluid because emulsion is the current dominant lubricant strategy for crankshaft drilling and MQL is a potential step to reduce the environmental impact of machining and reduce the full life cycle environmental cost of the component. Drilling of high-strength materials generates significant heat energy and adequate surface wetting, cooling, and heat evacuation is important for surface integrity. Therefore, it was important to investigate the influence of lubricant strategy on drilled crankshaft oil holes. With that in mind, an experimental trial was performed to evaluate the potential impacts of switching to a sustainable lubricant strategy. The techniques established in previous chapters were used to evaluate the surface integrity of holes drilled with both MQL and emulsion metalworking fluid across a range of machining parameters.

9.1 Experimental Method

This section highlights the machine tool setup and experimental procedure that was used to evaluate the effectiveness of MQL for deep-hole drilling.

9.1.1 Setup

For both the MQL and emulsion drillings, the workpieces constituted as-rolled AISI 4140 steel with dimensions of 250x115x80mm that were rigidly attached to a Kistler 9255C force-dynamometer to capture cutting forces during drilling. The setup of the machine tool used for emulsion drilling is identical to the machining conducted in the previous chapters. A schematic of the setup on the machine used for MQL machining in this chapter is shown in figure 9.1. Drilling trials were performed on a Mazak Smart 430a 3-axis CNC machining centre.

For MQL drilling, neat Soybean oil was mixed with air at 8 bar immediately before the spindle to produce an aerosol mixture using a customised system (Figure 9.2). This reduced the likelihood of oil-air separation and is an improvement over a conventional single-channel system that mixes the air externally before pumping it through long tubes to the spindle. In that instance, there is more time for the oil and air to separate, reducing oil flow to the target cutting region. Emulsion drilling was performed with Blaser Vasco 7000 coolant that was supplied to the tool-tip at 8% concentration.

Figure 9.1: Machine tool and MQL pump system

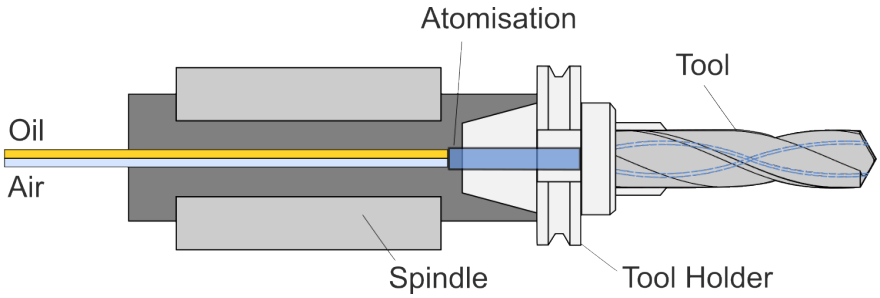

Figure 9.2: Schematic of the dual channel MQL system, with atomisation immediately prior to the tool holder

Sandvik Corodrill 865 8mm diameter drills were used for all drilling operations since they are optimised for use with both emulsion and MQL metalworking fluid strategies. A single tool was used for each lubricant strategy to mitigate the influence of variable tool diameter, condition, or tool wear. The cutting edges were imaged in discrete ten-hole intervals, and these images were post-processed to calculate flank wear. The number of holes drilled in these trials was not sufficient to induce large changes in tool wear between the two lubricant strategies. This is a positive result as tool wear characterisation was intentionally omitted from the objectives of this investigation.

9.1.2 Experimental Procedure

The target oil flow rate, Q is controlled by the intermittent release of oil from the external pumping system. The actual flow rate was measured by attaching a bucket under the tool and measuring the increase in weight of the bucket after a fixed time frame. A 5% discrepancy was deemed acceptable, as small amounts of oil could be lost into the atmosphere or pooled inside the system without a significant impact on performance. When the target flow rate was changed, a purge cycle was run for 10 minutes to flush the delivery system and ensure a stable flow rate. After this purge cycle, a flow rate test was performed. During crankshaft

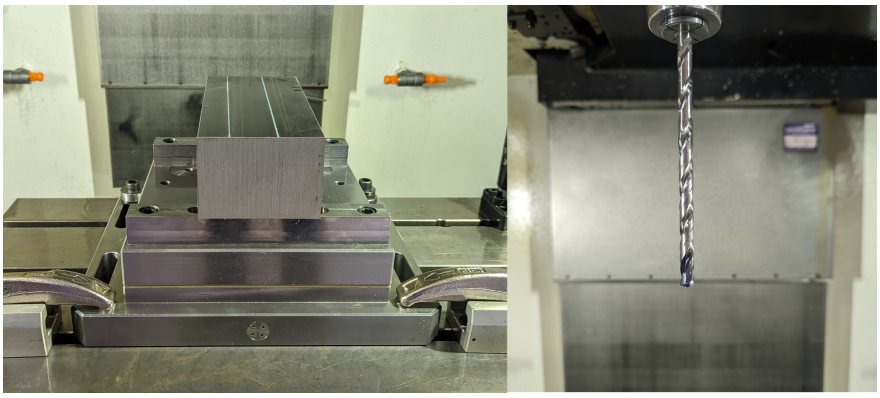

Figure 9.3: Workpiece setup and tooling with low-visibility coolant flow

machining, the manufacturer would likely select a flow rate that yields the lowest cutting forces, to minimise tool wear and reduce the component cost. Therefore, it was important to consider this motivation and first assess cutting forces at low and high oil flow rates. 10ml/hr and 50ml/hr were selected for testing based on the prior industrial experience of Sandvik Coromant and the limitations of the machine tool. Each flow rate was used to machine 3 holes with a low and high feed rate and cutting speed. The cutting forces were then analysed to select an appropriate flow rate for further experimentation.

With a suitable flow rate established, a range of feed rates (0.17-0.224 mm/rev) and cutting speeds (65-80m/min) were exploited to achieve cutting conditions with varied thermal and mechanical effects, while remaining within the recommended limits set by the tooling manufacturer. The experiments were designed on the basis of a three-factor, three-level factorial design model. This was chosen to minimise the number of experiments required to develop a statistically significant model. Three holes were drilled at each set of machining parameters. A Coordinate-Measurement Machine (CMM) was used to measure the diameter and circularity of the drilled holes. The system is situated within a 20°C temperature-controlled room. Stable room temperature ensures that the volume of the workpiece remains consistent throughout the measurement. During operation, a contact probe is lowered into the hole and rotated to measure the exact location of discrete points around the circumference. These are then stitched together to calculate the average diameter at the chosen measurement depths and the hole circularity. Circularity describes the deviation of the cross section from a perfect circle. The machine was programmed to take measurements around the circumference at depths of 10mm, 30mm, 50mm, and 70mm. The 10mm measurement point lies within the pilot hole region and was used as a control point, since the pilot holes should be unaffected by the drilling operation unless there is significant rubbing of the drill margin on the pilot hole wall.

After the hole geometry had been characterised, the workpiece was sectioned to expose the surfaces of the hole wall for surface roughness analysis. 3D surface topography scans were

taken using a Bruker Alicona InfiniteFocus SL optical measurement system. The hole form was removed using a Gaussian Planar model and the estimated radius was compared to the measured CMM radius to validate accurate form estimation. 2D profiles were then taken along the vertical hole axis at a profile width of 10μm as per the recommendations of Section 5.4.1. R_a, R_z and R_q were calculated for these profiles. Following surface analysis, X-Ray Diffractometry was used to assess the amount of deformation in the near surface and select appropriate specimens for further analysis. Cross-sectional samples were extracted from the machined workpiece and prepared for optical microscopy according to the procedure described in Section 4.4. Optical micrographs were captured at magnifications ranging from 5x to 100x using a Nikon LV150N benchtop microscope. Optical microscopy was not sufficient to identify microstructural changes following MQL, so EBSD analysis was conducted to further characterise deformation in the machining-affected layer. Due to the large cost and time requirements of EBSD analysis, a single specimen was selected with each lubricant strategy for analysis. Large differences in the post-drilled microstructure were observed with the two lubricant strategies.

9.2 Results

9.2.1 Cutting Forces

Cutting forces were monitored by a dynamometer mounted beneath the workpiece during both MQL and emulsion drilling. Since a fixture system was used, the position of the holes with respect to the dynamometer piezos was known and, therefore, both torque and thrust force could be calculated. It was important to first assess the influence of flow rate on cutting forces, since efficient supply of lubricant to the contact zones during machining is key to the performance of the cutting process. The effect of flow rate on thrust force and torque during drilling at two speed and feed conditions is illustrated in figure 9.4. For the purposes of analysis, only two parameters are varied in each case, and the third is kept constant.

Although at first glance the flow rate appears to have a notable effect on cutting forces, it is important to note that it is difficult to derive a significant relationship from the results due to the frequent overlap in error bars. At low feed rate, both flow rates performed almost identically and with similar repeatability in both thrust force and torque. On the contrary, with a higher feed rate, a higher flow rate generated marginally higher thrust force and torque. Since the lower oil flow rate of 10 ml/hr yielded lower cutting forces, it was used for all further experiments. A large combination of machining parameters was used to induce changes in the machining conditions. Since automotive manufacturing is high-volume and relies on high productivity, it is logical to consider manufacturing throughput, measured by the vertical feed rate of the machining centre. This is governed by the multiplied magnitude of the rotational speed of the drill and the feed rate per revolution. All results are presented

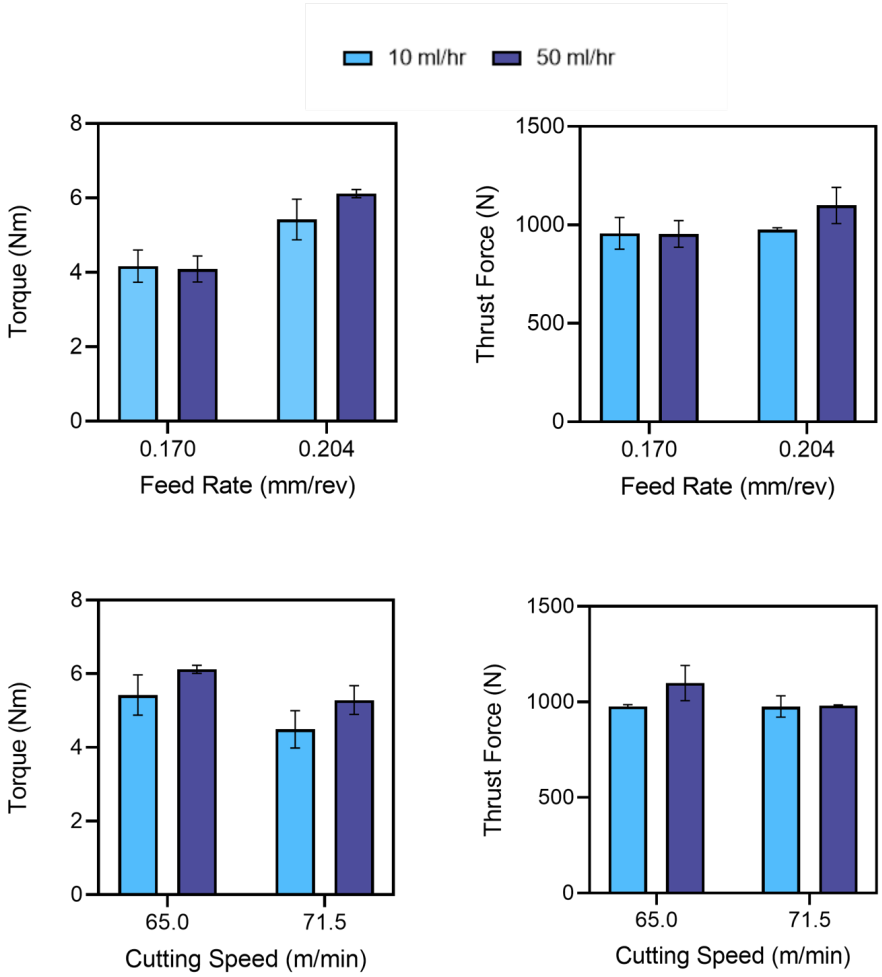

Figure 9.4: Average torque and thrust force during drilling with varied parameters and a high and low MQL oil flow rate, with error bars calculated from the standard deviation of three repeats

in terms of vertical feed rate. The change in thrust force and torque with increased machining productivity is shown in Figure 9.5.

There was no consistent trend in thrust or torque with vertical feed rate for either lubricant strategy, but thrust force was higher for MQL across all parameters. The emulsion drilling torque exhibited much more variation with machining parameters than MQL drilling. At lower feed rates the torque required to drill with MQL was higher, but at higher feed rates the reverse was true. The holes machined at 525mm/min required the highest thrust force and torque for both lubricant strategies. This was a combination of high feed rate (0.204 mm/rev) and low cutting speed (65m/min). Conversely, thrust forces were minimised when the material was machined at a low feed rate (0.17 mm/rev) and high cutting speed (71.5 m/min).

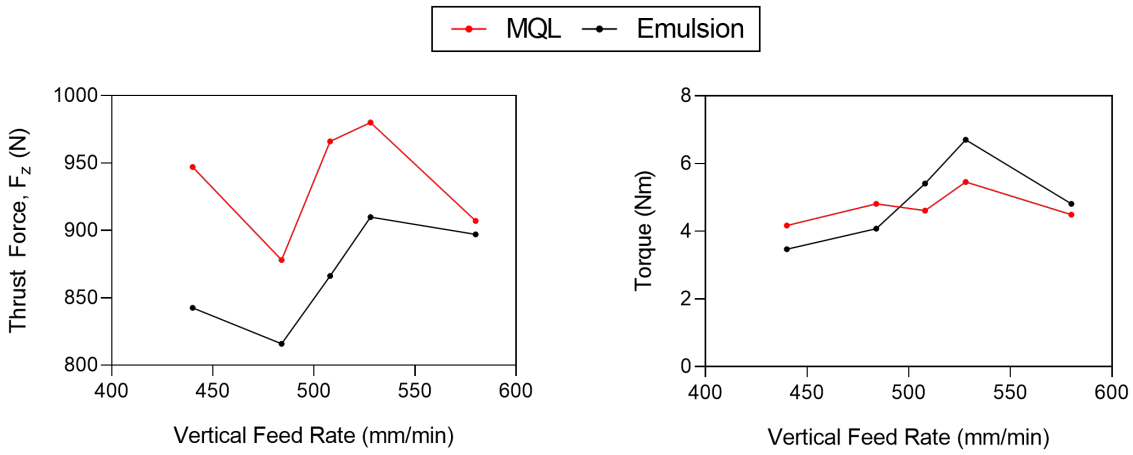

Figure 9.5: The change in cutting forces with increasing vertical feed rate for both MQL and emulsion lubricant strategies

9.2.2 Hole Quality

It was noted that MQL machining produced chips that were discoloured in brown and blue hues, in contrast to silver chips generated during emulsion machining. The colours indicated that the chips had reached high temperatures in the order of 4-500°C. Due to this colour change, the chips were collected between cuts and inspected under an optical microscope. On first inspection, the MQL chips exhibited more prominent shear bands, and the secondary shear zone of the MQL chips was slightly smaller. There is no evidence of phase transformation in the MQL chips, indicating that either temperatures were not sufficient to induce austenite transformation or cooling rates were too slow to retain carbon within the crystal structure and cause martensite formation. Despite the minor differences, all captured chips would pass visual checks with no evidence to suggest poor process performance.

The diameter, circularity, and cylindricity of the machined holes were measured at various depths, with results presented in Figure 9.6. Measurements were taken in 20mm depth increments from 10mm to 70mm and averaged to account for any change in tool dynamics, temperature and chip handling with increasing tool engagement. The reference diameter of the tool before machining is also plotted as a dashed line. The reference tool diameter could be used as a comparison because the same tool was used for all operations with a single lubricant strategy. The diameter of the tool did not change significantly during the trial due to the small number of holes drilled with each set of parameters.

The diameter of the hole was significantly greater following MQL drilling. Except for the slowest parameter set, MQL drilling generated a hole that was approximately 15μm larger than the diameter of the tool and invariant with machining parameters. Emulsion drilling yielded a hole diameter that was only marginally larger than the reference diameter of the tool and did not change notably with machining parameters. Circularity represents the variation

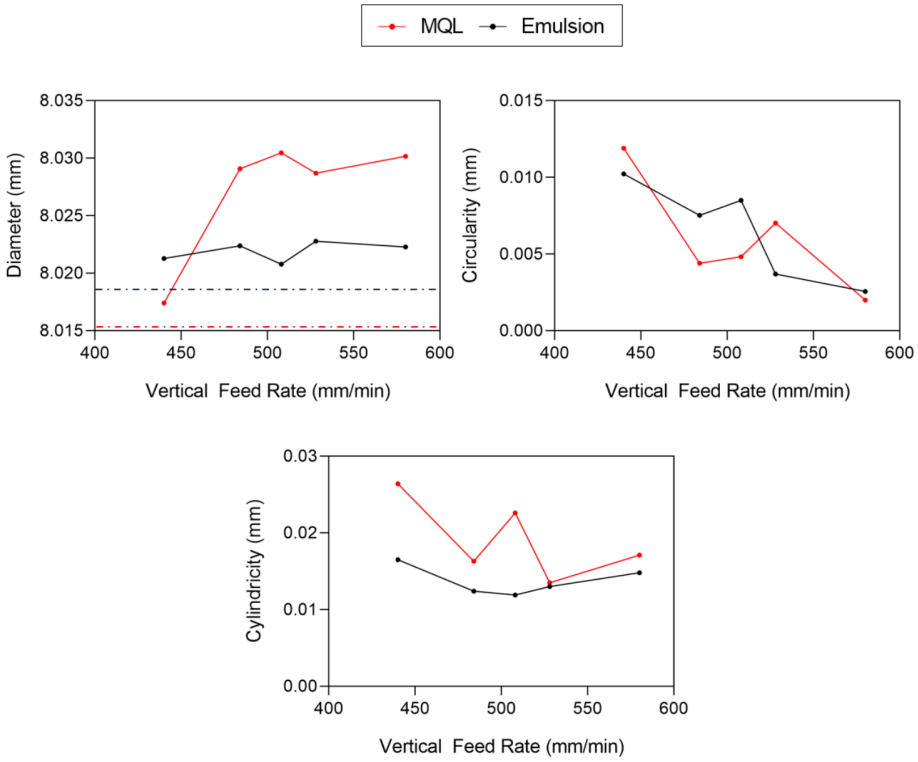

Figure 9.6: Evolution of hole diameter, circularity, and cylindricity with vertical feed rate for both lubricant strategies. The dashed lines represent the diameter of the tool prior to machining

in circumference with reference to a perfect circle. Circularity decreased from the slowest to the fastest parameter set with variation in the mid-range for both lubricant strategies. Circularity also consistently decreased when feed rate was kept constant and cutting speed was increased. Cylindricity describes the variation in the form of the hole compared to a perfect cylinder across the entire depth. For emulsion drilling, the cylindricity was fairly consistent, with a small improvement in the mid-range. The lowest cylindricity was achieved at a feed rate of 68.25 mm/rev and a cutting speed of 68.25 m/min. The cylindricity of the MQL holes decreased between the slowest and the fastest speed with a spike in the mid-range. Diameter and circularity were compared against the machining forces to identify any correlation (Figures 9.7 and 9.8). There was no clear relationship between the captured machining forces and the measured hole quality properties for either lubricant strategy.

Following geometric analysis, the workpieces were sectioned to expose the holes' surfaces for inspection. Previous drilling trials had only identified minor changes in surface quality with machining parameters, which was attributed to the high quality of modern drilling tooling. Therefore, only holes machined at the most and least aggressive parameter sets were inspected. The effect of lubricant strategy on surface quality was assessed using mean arithmetic roughness, R_a, maximum valley depth R_v and ten-point peak to valley height,

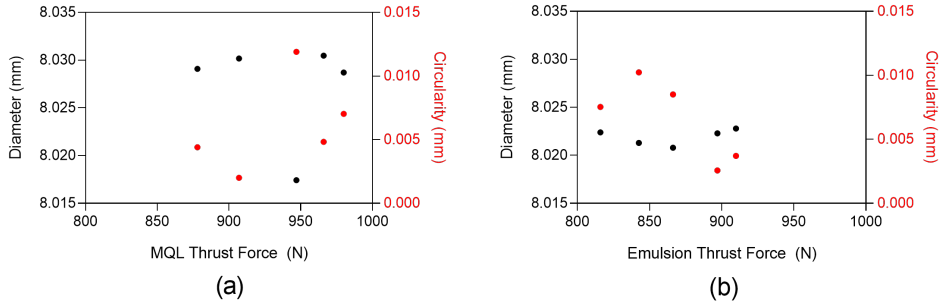

Figure 9.7: The change in hole diameter and circularity with measured thrust force for (a) MQL and (b) Emulsion

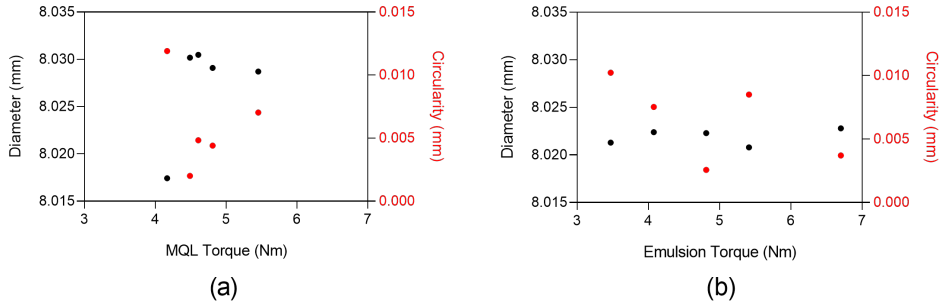

Figure 9.8: The change in hole diameter and circularity with measured torque for (a) MQL and (b) Emulsion

R_z (Figure 9.9). The error bars represent the standard deviation of measurements taken in three separate holes. For both lubricant strategies, all three surface integrity metrics were worsened by a faster drilling cycle. At low speeds, MQL drilling provided the smallest mean roughness and valley depth, but at high speeds this reversed. The peak-to-valley height was slightly higher for the MQL drillings across both sets of parameters. Repeatability was notably worse for MQL with a large variation between the measured holes.

XRD analysis was conducted to identify large variations in the near-surface microstructure and select samples for further analysis. The change in full width at half maximum (FWHM) peak breadth of the XRD response with machining parameters and lubricant strategy is presented in Figure 9.10. As with surface roughness, only the holes machined at the lowest and highest speeds were examined. 18 repeats were taken across three holes and two depths for each combination of machining speed and lubricant. MQL and emulsion provided a comparable peak breadth at low speeds, but at high speeds the MQL peak broadened significantly compared to the emulsion peak, which did not change signficantly. Measurements were more variable at high speeds for both types of lubricants. For the emulsion drillings there was no significant trend in FWHM peak breadth with machining parameters. This suggests that the lubricant was responsible for large changes in the near-surface microstructure after high-speed drilling.

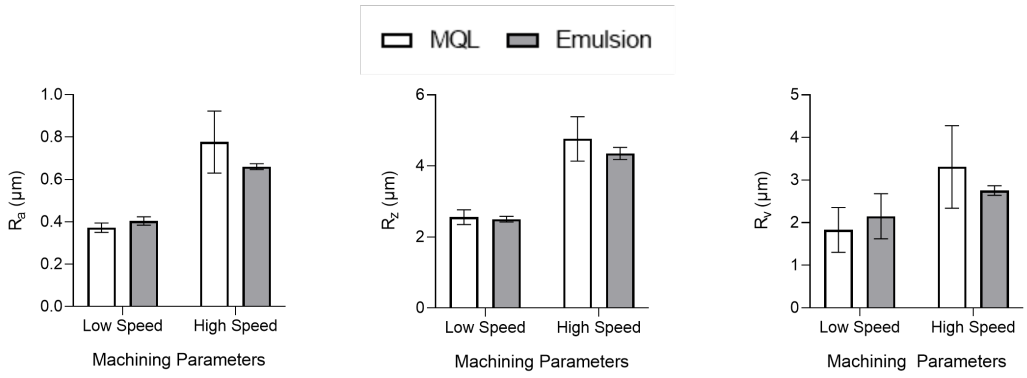

Figure 9.9: Change in measured drilled hole wall roughness with lubricant strategy at low and high production speeds

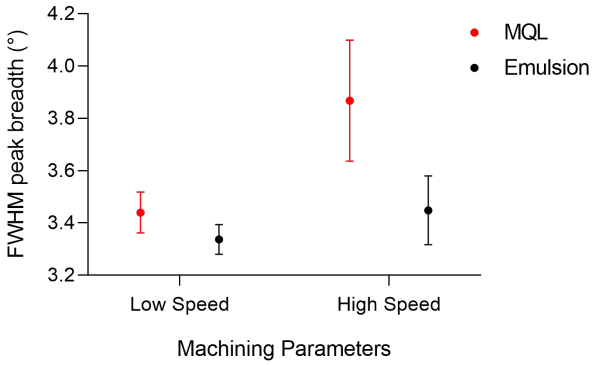

Figure 9.10: Change in Full-Width Half Maximum peak breadth between MQL and emulsion lubricant strategies at high and low machining rates

Light-Optical Microscopy analysis was conducted on cross-sectional hole samples that had been polished and etched with Nital reagent to reveal the sub-surface microstructure. The micrographs showed no evidence of white layer formation with either lubricant strategy. A slight darkening at the near-surface due to an increased density of grain boundaries, in particular pearlite colonies, was more prominent in the MQL drillings. However, it was not extensive enough to suggest that it was definitely an effect of the lubricant. To provide further information surrounding sub-surface microstructural evolution, EBSD was used to analyse the machine-affected region. The inverse pole figure (IPF) map calculated from an EBSD scan of a specimen machined with each lubricant strategy is shown in Figure 9.11. The IPF map shows which crystallographic direction is parralel to the sample direction. It must be noted that while the calculated IPF is consistent within a single scan, the relative crystal direction cannot be compared between specimens as it is influenced by the specimen geometry and position. However, the distribution of crystal orientations can be reliably compared between specimens.

Both samples present an unindexable heavily strained region at the surface that is slightly

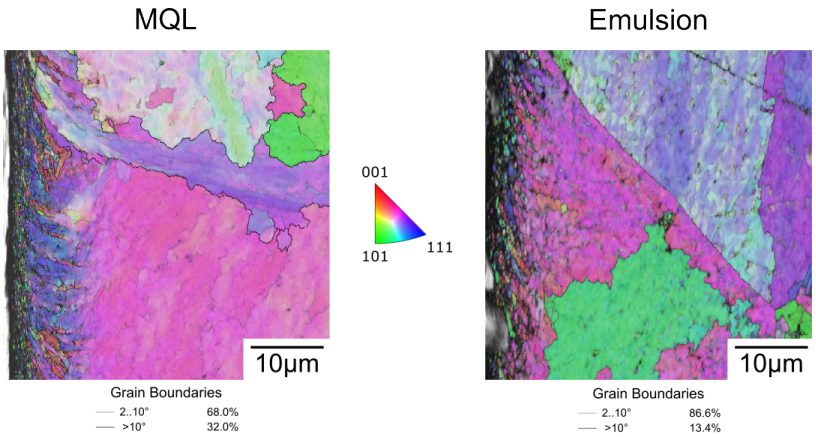

Figure 9.11: Combined IPF and Band Contrast map with the distribution of grain boundary angles

smaller in the MQL specimen. In the MQL drillings, this is followed by a region of heavily refined grains of sub-micrometre thickness with striations that progress deeper into the material. For emulsion drillings, the near-surface grains are coarser and there is no prominent striation pattern, but unindexed grains are present at a deeper level. The general grain structure of the sub-surface beyond 15μm is broadly similar for both specimens, however, there appears to be evidence of sub-grain deformation in the emulsion specimens, compared to a more uniform crystal structure after MQL drilling. The MQL grain boundary orientation was also much more heavily skewed to higher grain angles. This was further investigated by overlaying the calculated Kernel Average Misorientation (KAM) onto the Band Contrast map (Figure 9.12). KAM represents the magnitude of relative disorientation between the grains. Regions of greater disorientation are shaded in green.

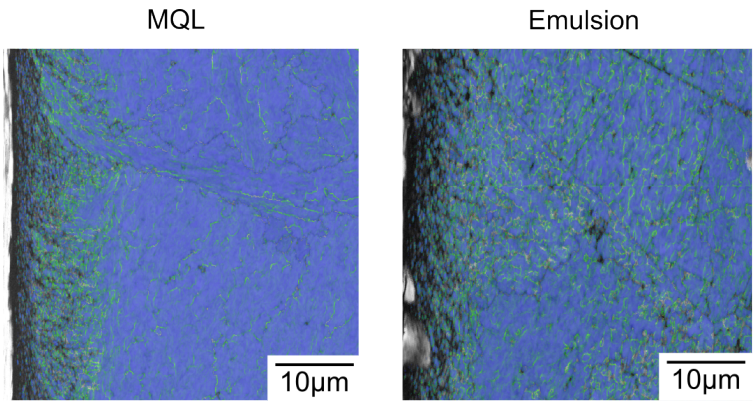

Figure 9.12: Distribution of Kernel Average Misorientation across the plastically deformed layer

The MQL specimen presents a heavily disorientated near-surface region that is approximately 12 μm thick, followed by a distinctly uniform sub-surface region of low grain disorientation. Conversely, for the emulsion specimen, the entire micrograph exhibits grain disorientation,

with relatively fewer high-angle boundaries at the near-surface. The local and global misorientation of the grains was quantified by calculating the relative frequency of the distribution of the grain angles for the plastically deformed layer and the sub-surface material (Figure 9.13).

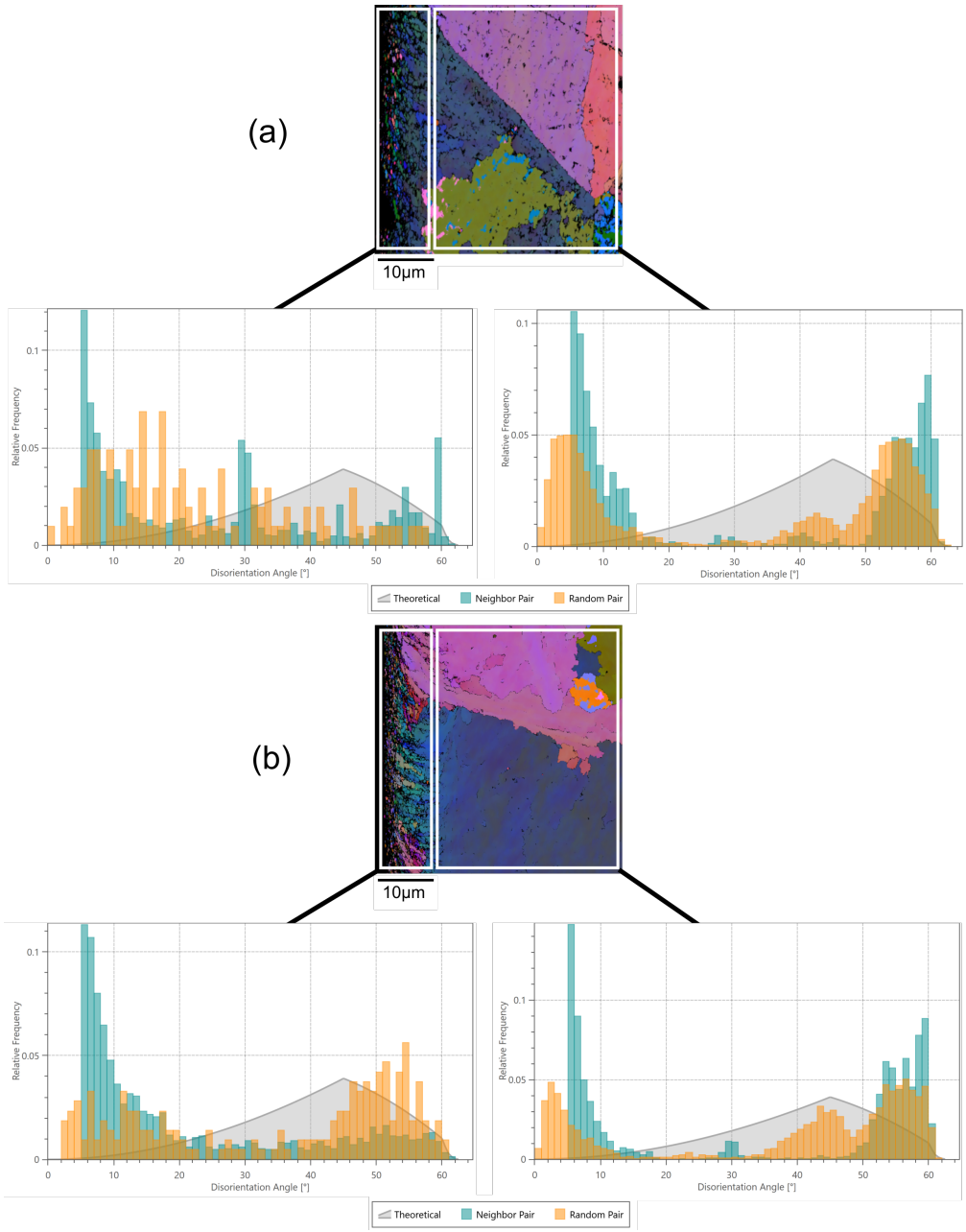

Figure 9.13: Kernel Average Misorientation maps of the surface and near-surface of holes drilled with (a) Emulsion and (b) MQL

The sample drilled with emulsion exhibited a more random distribution of grain disorientation angles in the heavily deformed near-surface, with a skew toward the low and mid-range. Conversely, disorientation in the heavily deformed layer of the MQL sample was heavily skewed toward high angles. The sub-surface was much more similar, with a decrease in low-angle boundaries for the MQL sample.

9.3 Discussion

Despite the clear sustainability benefits of MQL strategies, for MQL to be adopted in an industrial machining process it must be able to produce adequate operating speeds, hole quality, and power requirements to emulsion machining, or at least a significant benefit in an area that is beneficial to the business.

9.3.1 Oil Flow Rate

The increase in cutting forces with oil flow rate was unusual, as a higher oil flow was expected to yield better lubricity at the sliding contact. As oil flow rate increases, the average flow velocity decreases due to the larger mass of the fluid. Furthermore, the average droplet diameter increases, causing a reduction in the amount of droplet penetration at the cutting edge. One study has proposed that increasing the flow rate improves lubricity and aids efficient cutting up to a point where larger quantities of viscous oil flood the cutting zone and hinder chip evacuation [126]. The relationship was more prominent for straight flute drills, which are more sensitive to chip evacuation issues. With twist drills the relationship was more complex and variation in tool wear increased variability. For the results in this chapter, the difference in force between the two flow rates increased with feed rate. Increasing feed rate generates thicker chips that are more difficult to evacuate. This supports the hypothesis that at higher flow rates chip evacuation was inhibited. However, the change in oil volumes was minimal and likely insufficient to hinder the evacuation of high-speed chips that are much larger in mass. If the oil droplets are too large to be swiftly carried away from the cutting zone and out of the hole, the oil may pool in the hole and the efficiency of heat transfer away from the cutting zone could reduce, yielding a rise in cutting temperatures. More work is needed to characterise the change in cutting efficiency with flow rate, but 10ml/hr was deemed sufficient for these trials and was in agreement with previous industrial experience.

9.3.2 The impact of MQL on hole quality

It was important to assess both lubricant strategies across a range of machining parameters, to identify the relative strengths and weaknesses. The strategies possess different cooling, chip evacuation and lubrication capabilities and so it was unknown how each would respond to varied machining conditions. On average MQL drilling resulted in a higher thrust force, hole diameter and cylindricity than emulsion. Thrust force is typically dominated by the cutting action at the chisel edge and was higher on average for MQL than emulsion drilling [127]. The chisel edge is designed with a negative rake angle to increase strength and because of this the chisel edge ploughs and extrudes material rather than cutting it. This is accepted because its primary function is to centre the drill bit, but it leads to large axial thrust forces and high friction. Due to the extremely high contact pressures at the chisel and

cutting edge contacts, it is unlikely that coolant will penetrate the tool-workpiece contact at the rake face and provide meaningful lubrication and a difference to the forces generated there. Emulsion force increased significantly at the most aggressive parameter set and reduced the disparity between the two lubricants. Uncut chip thickness increases linearly with feed rate, with an associated increase in the volume of deformed material and load on the outer corner of the drill. The blue hue of the MQL chips suggests that the chips were much hotter. More prominent shear bands were also evident in the chips following machining with an MQL strategy. Shear bands are a region of highly concentrated plastic flow which are characterised by collective dislocation in narrow deformed zones surrounded by adjacent regions of comparatively low and homogeneous plastic flow. Shear band formation is promoted when homogeneous dislocation slip is inhibited, or an insufficient number of slip systems are available. Shear banding can act as an alternative deformation mode, which is accompanied by a sudden drop in localised flow stress. As such it acts as a flow softening mechanism. The subsequently lower stress required for plastic strain of hotter material may have reduced the differential between the two strategies [128]. This may have been exacerbated by the higher strain rates, which encourage adiabatic heating through internal friction and frictional heat generation at the rake face. Although studies have shown that toward machining strain rates the changes are negligible [121].

While chip formation constitutes the bulk of machining forces, increased friction may also have contributed to the force differential. The contact pressures at the margin-wall interface are much lower than at the cutting edge and lubricant may be more likely to penetrate this area. MQL studies of roller burnishing, which operates with similar contact conditions to drilling, have demonstrated variation in surface properties with changing lubricant type [129]. This is supported by the greater degradation in surface finish at high speeds for MQL.

The geometric properties of a drilled hole are important in ensuring tolerances are achieved in production parts. Oversized, undersized, and out-of-round holes can be detrimental to part strength and function and may inhibit fastening of assembled components. Drilling with MQL generated a greater hole diameter and cylindricity than drilling with emulsion on average and comparable circularity across all tested parameter sets. The significant increase in hole diameter with MQL is attributed to thermal expansion of the tool during drilling. Thermal expansion is particularly extensive during dry drilling, where a tapered hole geometry with a smaller diameter entry has been reported in the literature [130]. No correlation between hole depth and diameter was seen here, although the first measurement was taken at 10mm, which may be after the tool has reached a steady-state temperature. MQL is a near-dry process and so may face similar issues with thermal expansion. It is possible for BUE formation to also cause increased hole diameter. However, circularity would probably also be negatively influenced by the continue build-up and break-off of adhered

material on the tool. Diameter increased on average with vertical feed rate while circularity decreased, which suggests that BUE was not the main driving force for the diameter change.

Operating at the most aggressive machining parameters with the maximum feed rate and cutting speed yielded a diminished surface finish across both lubricant strategies. While increasing the feed rate has consistently been shown to worsen the surface finish, studies have shown conflicting results for cutting speed [131, 132]. A higher ratio of feed rate to tool corner radius promotes a poorer surface finish by encouraging ploughing rather than shearing at the drill margin and a larger step distance. There is often also a reduced surface polishing effect due to fewer passes of the margin on the wall of the hole, which is a mechanism that was noted in the burnishing research in Chapter 6. The influence of cutting speed is more complex and modulated by competition between the competing effects of increased ductility of asperities at higher temperatures and negative influence of greater adhesion at the margin-wall contact. Interestingly, MQL appeared to be more sensitive to these parameters than emulsion. MQL thrust force, torque and hole diameter also increased with cutting speed and deeper feed lines were noted, which gave the appearance of repeated low-amplitude scores on the surface. Taken together, these results signify higher tool temperatures and increased friction at the margin-wall contact. When BUE formation is encouraged, surface finish deteriorates, which would explain the reduction in performance [133]. The increase in hole diameter and degradation in surface finish at higher speeds suggests that tool expansion or built-up edge (BUE) formation has indeed taken place. In future, it would be useful to embed thermocouples along the drill path to monitor tool and workpiece temperatures and further understand the contributing factors behind surface quality.

MQL performed much better at lower machining speeds, even providing a better mean surface finish than emulsion. The ability to operate at high speeds without affecting the quality of the hole is a key requirement for crankshaft drilling operations, and MQL performed less effectively under these conditions. The variability in finish across multiple holes was also a concern. The variation in R_{v} in particular suggests that thermal expansion of the tool or inefficient chip removal may leave sporadic grooves in the drilled surface. Industrial processes are regularly assessed on the repeatability of quality metrics and this may be deemed unacceptable. Despite this, even at the most aggressive machining parameters, the surface roughness for both lubricant strategies was lower than the limit at which surface roughness would be expected to influence fatigue failure [42]. Based on the results seen here, a worsened surface finish should not cause rejection of MQL lubrication, provided repeatability can be improved.

While LOM analysis of the drilled samples revealed little distinction between the microstructure generated by with the two lubricant strategies, EBSD was much more informative. MQL

drilling appears to have encouraged the generation of a thin band of severe plastic deformation followed by a thicker layer of grains that have also been refined but to a lesser extent. As it is a near-dry machining strategy, MQL offers significantly reduced cooling capability compared to emulsion as a result of the reduced thermal conductivity and volume of the cooling media [6]. With inefficient cooling, plastic deformation on the surface of the hole wall can lead to localised heat build-up and higher workpiece temperatures. As shown in Chapter 8, the capacity for strain hardening increases with temperature for 4140 steel, however so does the rate of dynamic softening.

Caudill et al. [129] noted a reduction in surface hardness when burnishing Ti-64 with MQL compared to emulsion. The depth of the machining-affected layer was also found to decrease. This was hypothesised to be driven by a rapid concentration of localised heat energy at the surface which encouraged dynamic recrystallisation during deformation. In this study, no softening of the near surface was identified, but a region of reduced hardness has been identified in the near-surface following MQL drilling of Ti-64 [134]. The softening was attributed to heat generated during the cutting process which was verified via a thermocouple embedded in the hole. Ti-64 has a very low thermal conductivity, which would limit the transfer of machining heat deeper into the sub-surface. This explains why the softening was isolated to the near-surface. 4140 steel is much more thermally conductive, and so heat generated under deformation may more easily transmit to the near-surface. During MQL drilling, the surface contains large strain energy and thermal energy, which is conducive to concentrated deformation, hence the thin band of severe plastic deformation. The sub-surface still contains thermal energy but with less plastic strain. This promotes the onset of grain evolution mechanisms such as recovery and recrystallisation, which serve to annihilate dislocations and reduce stored internal energy. This may explain why the immediate near-surface is less heavily refined for the MQL specimen. The appearance of striations in the near-surface of the MQL specimen may be due to increased friction between the margin and hole wall. While the oil content of MQL may provide lubrication to the contact, adhesive friction increases with temperature [85]. Enhanced friction may cause intermittent adhesion under asperity contact, similar to stick slip phenomena [135]. Repeated increase and decrease in friction as the margin passes the hole wall could shear the near surface in the cutting direction, leading to the appearance of the striations within the sub-surface.

MQL provides an undisputed improvement to the sustainability of machining operations and provides a logical next step to manufacturers on their journey to net zero. However, as this research has shown, there are a number of negative side effects to its reduced cooling capacity. It should be noted that soybean oil was chosen due to its availability and regular use within the industry rather than any expected performance characteristics. MQL systems are often operated vegetable oils as lubricants due to sustainability benefits. Research revealed that the thermal and dynamic properties of oils can vary significantly with temperature (9.14).

This relationship is not identical between lubricants and some oils exhibit better stability at higher temperatures. It will be of interest in future to consider the change in thermal properties of vegetable oils with temperature and assess the influence of these properties on the performance of the MQL drilling cycle. The use of a single lubricant was a limitation of this research.

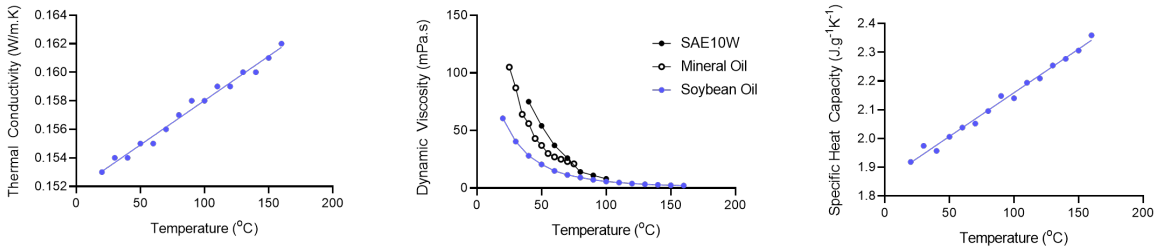

Figure 9.14: Variation in the thermal properties of soybean oil with increasing fluid temperature

9.4 Concluding Remarks

Moving toward more sustainable lubricant strategies is a reasonable way to achieve a reduction in the embodied carbon of manufactured parts. However, consideration must be given to the long-term implications of such changes, not just for the predicted life of tooling but also the integrity of machined surfaces. This study aimed to evaluate the impact of MQL on hole quality metrics that are key to crankshaft oil hole production. At higher production speeds, MQL exhibited large variability in surface finish, which was attributed to poor chip evacuation and high cutting temperatures. Although the surface finish was within specification for both lubricant strategies, the variability of the MQL drillings would be of concern for manufacturers. High machining temperatures also impacted the machined surface microstructure, with evidence of a smaller band of severe plastic deformation in the near-surface and greater distribution of strain to lower depths. Unfortunately, hardness testing was not conducted on the specimens, so it was unknown whether the near-surface grain refinement in the MQL specimens was greater in magnitude or solely more localised.

Although MQL drilling has numerous environmental advantages, extensive implementation will require a more thorough understanding of the impacts of MQL on the near-surface material microstructure. Although white etching layer (WEL) was not explicitly identified in the micrographs, MQL drilling clearly provides the prerequisite conditions of high temperatures and severe plastic deformation that may facilitate WEL formation. The propensity for WEL formation should be further investigated before widespread implementation of MQL methodologies, particularly in crankshaft drilling where the machined surface is not

visible. Decades of research and investment have been targeted toward optimising emulsion-lubricated machining processes. The same level of technical understanding will be required to ensure continuous improvement of MQL machining processes and ensure the same high performance standards can be achieved.

Chapter 10

Conclusions

In this research project, key aspects of the hole drilling process have been investigated to improve understanding of the influence of the drilling procedure on surface integrity. The impact of potential future changes to the drilling process was investigated to help protect against unexpected reductions in quality of the crankshaft oil hole. Methodologies for sample analysis were also established, which will support the continuation of this research. The key findings are summarised below.

- Following drilling of AISI 4140 Steel, plastic deformation and subsequent grain evolution was found to be concentrated at the near-surface. Microhardness testing, which is regularly used for industrial testing, was shown to be incapable of resolving this small plastically deformed layer.
- A sub-surface grain recovery phenomenon was identified following internal roller burnishing that, to the author's knowledge, had not previously been described in the literature. The reduction in dislocation density and measured hardness below the initial plastically deformed layer was hypothesised to have been driven by the conduction of heat from the contact zone. It is recommended that full component fatigue testing is conducted with burnished holes prior to addition of burnishing to the manufacturing process.
- Light optical microscopy analysis of the surfaces of drilled holes was found to be highly subjective, as it required the researcher to judge grain morpohology changes within a region of heavy plastic deformation. This was made more difficult by the amorphous nature of the ferritic-pearlitic microstructure. While EBSD analysis, in particular Kernel Average Misorientation, was better able to identify grain evolution in the near surface, it required significant time and cost investment. In light of this, an inspection method for detecting microstructural changes prior to more extensive analyses

was developed, using the novel application of a portable X-Ray diffractometer on sectioned drilled surfaces. X-Ray Diffraction was capable of detecting the presence of microstructural changes and aided selection of specimens for more extensive analysis. It also removed the subjectivity of manual interpretation.

- X-Ray Diffraction was also able to accurately map the transition of the crankshaft microstructure from the hardened martensitic surface to the deeper forged ferritic-pearlitic microstructure. This presented XRD as a viable method of analysing the transition between microstructures in induction hardened specimens, without the need for extensive preparation.

- AISI 4140 Steel demonstrated significant adiabatic heating and a propensity for martensite formation during high-speed compression testing. Deformation at high temperatures encouraged localised concentration of plastic strain and results indicated that under high-temperature conditions such as near-dry machining, localised heat generation could induce phase changes that are detrimental to fatigue life.

- High-speed drilling with near-dry Minimum Quantity Lubrication yielded a large increase in hole diameter and variability in surface finish compared to conventional emulsion machining. The high cutting temperatures were also found to increase friction at the margin-wall contact and affect the sub-surface microstructure. Further materials testing is required to validate the effect of these changes on fatigue strength. The adoption of alternative lubrication strategies is becoming increasingly common in industrial manufacture, but these results suggests that caution is required when generating holes in loaded regions with an MQL strategy.

It is important to note that although residual stress is a key contributor to fatigue strength, it was not measured or estimated at any point during this thesis. Holes had to be sectioned open for analysis, which was assumed to have relieved most of the residual elastic stress. However, residual stress may have impacted the various surface integrity measurements. Similarly, while improvement of fatigue strength was the key driver of this researcher, no fatigue testing was completed within this project. This was due to the lack of a universally recognised standard for fatigue testing of drilled holes samples and high cost of full-size component testing. Fatigue testing represents a key next step for the validation of this research, but the research conducted in this thesis represents a starting point from which further crankshaft oil hole analysis can be developed.

Chapter 11

Future Work

In this chapter, avenues of future work are outlined which expand on the work conducted in this thesis. These topics of investigation may have been completed within the project had it not been restricted by the impacts of the COVID-19 pandemic.

Although internal burnishing with externally supplied coolant did not yield sufficiently improved material properties to justify implementation, development of a new tooling design with internal through-tool coolant may provide mechanical improvement without the associated negative thermal effects. Crankshaft machining centres operate with multiple spindles, so it may also be possible to perform the burnishing operation whilst the drill is retracting from the hole. The drill would subsequently supply coolant at high-pressure directly to the burnishing contact zone. As an initial verification, it would be possible to create a fixture to supply coolant through the underside of the hole, directly to the burnishing rollers. This could potentially limit heat generation and prevent a reduction in hardness in the sub-surface. If this is successful, the multi-spindle processing route could be explored.

During the MQL-drilling research within this thesis, only a single lubricant and a small number of flow rates were utilised. It would be beneficial to trial a wider range of flow rates and several lubricants with varied lubricity and thermal properties. It may be possible to achieve an improved surface integrity with an optimised selection of lubricant and flow rate.

Crankshaft oil holes undergo an induction hardening procedure following machining and it is possible to emulate this procedure within the TMC test machine. It would be of interest to perform this heat treatment on samples that have been deformed under various conditions to identify whether the machined microstructure influences the post-hardened martensitic microstructure. The density of grain boundaries increases after deformation, and pearlite grain boundaries may provide nucleation sites for austenite and, in turn, martensite formation.

It would be beneficial to validate the findings of this thesis by employing a fatigue test protocol on drilled specimens. Unfortunately, there is no standardised fatigue test targeting drilled holes. An optimised chamfer would be required to mitigate failure at the stress concentration at the hole breakout. For the purposes of internal combustion engine research it would require a complex load profile that combined an irregular torsional load with a cyclic bending moment. An optimised fatigue test protocol could be applied to holes drilled using varied coolant methodologies, to establish whether the changes to surface microstructure following drilling have a noticeable impact on fatigue strength. This work may also be beneficial to aerospace manufacturers, if they are required to machine fastener holes in heavily loaded locations.

It remains extremely difficult to assess the residual stress state of the surface of a drilled hole with XRD due to the requirement for multiple tilt angles during analysis. While the emitter can be targeted at the hole surface by tilting the specimen, the geometry of the hole prevents the refracted X-Rays from being captured by the emitter. An alternative method of residual stress analysis termed the Contour method was discovered, which is regularly applied to steel materials. The contour method involves sectioning a workpiece with wire EDM, measuring the relaxation of the workpiece as the internal stresses are relieved using CMM equipment and then calculating the pre-sectioned residual stress profile using Bueckner's Superposition Principle and Finite Element methods [136]. It was hypothesised that the geometry of a drilled hole could be captured before and after sectioning with wire EDM using a CMM. The measured elastic deformation upon relaxation could then be used to calculate the residual stress state of the drilled hole. Initial investigations were conducted to examine the possibility of using the contour method to evaluate the residual stress profile of drilled holes, but this research was unable to be completed within the timeframe of this thesis. Initial results were promising and this presents a logical next step in evaluating the impact of the machining cycle that includes critical residual stress effects.

References

[1] Daniel Scott and Stefan Gössling. Destination net-zero: what does the international energy agency roadmap mean for tourism? *Journal of Sustainable Tourism*, 30(1):14–31, 1 2021.

[2] Joshua Hill and TheDriven. Electric vehicles take 16.9 pct share of new car market in UK, Model Y leads.

[3] Timothy W Spence and Makhlouf M Makhlouf. Materials Science & Engineering A The effect of machining-induced residual stresses on the creep characteristics of aluminum alloys. *Materials Science & Engineering A*, 630:125–130, 2015.

[4] XFlex. "Turnkey Manufacturing Line Solution" https://www.etxetar.com/en/products/xflex (accessed 03/08/23), 2023.

[5] Lin Wang, Dongsheng Qian, Jun Guo, and Yan Pan. Austenite grain growth behavior of AISI 4140 alloy steel. *Advances in Mechanical Engineering*, 2013, 2013.

[6] Alexander Stoll, Amando Jose Sebastian, Robert Klosinski, and Richard Furness. Lean and Environmentally Friendly Manufacturing – Minimum Quantity Lubrication (MQL) is a Key Technology for Driving the Paradigm Shift in Machining Operations. In *SAE Technical Papers*, 4 2008.

[7] Shigenobu Ogata, Ju Li, and Sidney Yip. Energy landscape of deformation twinning in bcc and fcc metals. *Physical Review B*, 71(22):224102, 6 2005.

[8] P Marshall. *Austenitic stainless steels : microstructure and mechanical properties*. Elsevier Applied Science, London, 1984.

[9] Xiang Wang, Jiangwei Wang, Yang He, Chongmin Wang, Li Zhong, and Scott X. Mao. Unstable twin in body-centered cubic tungsten nanocrystals. *Nature Communications*, 11(1):2497, 5 2020.

[10] Xiyao Li, Qingkun Zhao, Yanzhong Tian, Qiannan Wang, Jitang Fan, Kexing Song, Haofei Zhou, and Jiangwei Wang. Phase transformation induced transitional twin

boundary in body-centered cubic metals. *Acta Materialia*, 249(December 2022):118815, 5 2023.

[11] Junliang Liu. Deformation Induced Martensitic Transformation In 304 Stainless Steels. pages 1–79, 2016.

[12] Iyasu Tafese Jiregna, Goftila Gudeta Sirata, and Fitsum Tadesse Soramo. Fatigue Failure Analysis of Crankshafts-A Review. *IJISET-International Journal of Innovative Science, Engineering & Technology*, 7(5):93–106, 2020.

[13] Yang Zhao, Mengguo Lü, Quanhui Jiang, Liqing Chen, and Xianghua Liu. Fracture failure analysis of a vehicle engine crankshaft heat treated by quenching and high temperature tempering. *Jinshu Rechuli/Heat Treatment of Metals*, 38(4), 2013.

[14] Xiao Lei Xu and Zhi Wei Yu. Failure analysis of a truck diesel engine crankshaft made from spheroidal cast iron. *Journal of Failure Analysis and Prevention*, 11(4):332–336, 2011.

[15] M. Fonte, V. Infante, M. Freitas, and L. Reis. Failure mode analysis of two diesel engine crankshafts. In *Procedia Structural Integrity*, volume 1, pages 313–318. Elsevier B.V., 2016.

[16] M Fonte, Bin Li, L Reis, and M Freitas. Crankshaft failure analysis of a motor vehicle. *Engineering Failure Analysis*, 35:147–152, 2013.

[17] M. A. Alfares, A. H. Falah, and A. H. Elkholy. Failure analysis of a vehicle engine crankshaft. *Journal of Failure Analysis and Prevention*, 7(1):12–17, 2007.

[18] Zhiwei Yu and Xiaolei Xu. Failure analysis of a diesel engine crankshaft. *Engineering Failure Analysis*, 12(3):487–495, 6 2005.

[19] Gül Çevik and Riza Gürbüz. Effect of Fillet Rolling Load on the Fatigue Performance of a Micro-Alloy Steel Diesel Engine Crankshaft. In *Journal of Physics: Conference Series*, volume 843. Institute of Physics Publishing, 5 2017.

[20] T. E. Putra, Husaini, N. Ali, H. Husin, and Zulfikar. Failure analysis of the fracture surface of the crankshaft of a vehicle. In *IOP Conference Series: Materials Science and Engineering*, volume 523. Institute of Physics Publishing, 7 2019.

[21] J. W. Barton and H. L. Cox. Fatigue Tests on a Diesel Engine Crankshaft. *Proceedings of the Institution of Mechanical Engineers*, 184(1):241–252, 6 1969.

[22] Thomas Childerhouse, Rachid M'Saoubi, Luiz Franca, Nick Weston, Pete Crawforth, and Martin Jackson. The influence of machining induced surface integrity and residual

stress on the fatigue performance of Ti-6Al-4V following polycrystalline diamond and coated cemented carbide milling. *International Journal of Fatigue*, 163, 10 2022.

[23] Ataollah Javidi, Ulfried Rieger, and Wilfried Eichlseder. The effect of machining on the surface integrity and fatigue life. *International Journal of Fatigue*, 30(10-11):2050–2055, 10 2008.

[24] A. Pramanik, A. R. Dixit, S. Chattopadhyaya, M. S. Uddin, Yu Dong, A. K. Basak, and G. Littlefair. Fatigue life of machined components. *Advances in Manufacturing*, 5(1):59–76, 2017.

[25] Hiroyuki Sasahara. The effect on fatigue life of residual stress and surface hardness resulting from different cutting conditions of 0.45%C steel. *International Journal of Machine Tools and Manufacture*, 45(2):131–136, 2 2005.

[26] Xun Li, Peng Zhao, Yongsong Niu, and Chunming Guan. Influence of finish milling parameters on machined surface integrity and fatigue behavior of Ti1023 workpiece. *International Journal of Advanced Manufacturing Technology*, 91(1-4):1297–1307, 7 2017.

[27] D AROLA and C WILLIAMS. Estimating the fatigue stress concentration factor of machined surfaces. *International Journal of Fatigue*, 24(9):923–930, 9 2002.

[28] Xiaochun Zhu, Zhurong Dong, Yachen Zhang, and Zhengkun Cheng. Fatigue life prediction of machined specimens with the consideration of surface roughness. *Materials*, 14(18), 2021.

[29] Yu kui Gao, Xiang bin Li, Qing xiang Yang, and Mei Yao. Influence of surface integrity on fatigue strength of 40CrNi2Si2MoVA steel. *Materials Letters*, 61(2):466–469, 1 2007.

[30] Yukitaka Murakami. Effect of Surface Roughness on Fatigue Strength. In *Metal Fatigue*, pages 305–320. Elsevier, 2002.

[31] D. Novovic, R. C. Dewes, D. K. Aspinwall, W. Voice, and P. Bowen. The effect of machined topography and integrity on fatigue life. *International Journal of Machine Tools and Manufacture*, 44(2-3):125–134, 2004.

[32] M Balaji, K Venkata Rao, N Mohan Rao, and B S N Murthy. Optimization of drilling parameters for drilling of TI-6Al-4V based on surface roughness , fl ank wear and drill vibration. *Measurement*, 114(August 2017):332–339, 2018.

[33] A Z Sultan, Safian Sharif, and Denni Kurniawan. Effect of Machining Parameters on Tool Wear and Hole Quality of AISI 316L Stainless Steel in Conventional Drilling. *Procedia Manufacturing*, 2(February):202–207, 2015.

[34] E. Kuram, B. Ozcelik, E. Demirbas, and E. Şik. Effects of the cutting fluid types and cutting parameters on surface roughness and thrust force. *WCE 2010 - World Congress on Engineering 2010*, 2(November):1312–1315, 2010.

[35] Zhaoju Zhu, Bingwei He, and Jianxiong Chen. Evaluation of tool temperature distribution in MQL drilling of aluminum 2024-T351. *Journal of Manufacturing Processes*, 56(June):757–765, 2020.

[36] M. Mlikota, K. Dogahe, S. Schmauder, and Božić. Influence of the grain size on the fatigue initiation life curve. *International Journal of Fatigue*, 158, 5 2022.

[37] T. Kanemaru, Norio Kawagoishi, Eiji Kondo, Qing Yuan Wang, and Y. Ohzono. Influence of Grain Size on Notch Sensitivities in Fatigue of Carbon Steel. *Key Engineering Materials*, 385-387:197–200, 7 2008.

[38] H Sharifi, M Salehi, and M R Saeri. The Effect of Ferrite Grain Size on the Fatigue Behavior of Ferrite-martensite Dual-phase Steels. *International Journal of Iron & Steel Society of Iran*, 11(2):11–16, 2014.

[39] C. L. Kuo, S. L. Soo, D. K. Aspinwall, W. Thomas, S. Bradley, D. Pearson, R. M'Saoubi, and W. Leahy. The effect of cutting speed and feed rate on hole surface integrity in single-shot drilling of metallic-composite stacks. In *Procedia CIRP*, volume 13, pages 405–410. Elsevier B.V., 2014.

[40] J. Yi, M. Gharghouri, P. Bocher, and M. Medraj. Distortion and residual stress measurements of induction hardened AISI 4340 discs. *Materials Chemistry and Physics*, 142(1):248–258, 2013.

[41] Sangil Han, Shreyes N. Melkote, Michael S. Haluska, and Thomas R. Watkins. White layer formation due to phase transformation in orthogonal machining of AISI 1045 annealed steel. *Materials Science and Engineering: A*, 488(1-2), 2008.

[42] Guoliang Liu, Chuanzhen Huang, Bin Zhao, Wei Wang, and Shufeng Sun. Effect of Machined Surface Integrity on Fatigue Performance of Metal Workpiece: A Review, 12 2021.

[43] ASM International. Introduction to Steel Heat Treatment. In *Steel Heat Treating Fundamentals and Processes*, pages 3–25. ASM International, 8 2013.

[44] D.V. Shtansky, K. Nakai, and Y. Ohmori. Pearlite to austenite transformation in an Fe–2.6Cr–1C alloy. *Acta Materialia*, 47(9):2619–2632, 7 1999.

[45] Jerome Meiser and Herbert M. Urbassek. Ferrite-to-austenite and austenite-to-martensite phase transformations in the vicinity of a cementite particle: A molecular dynamics approach. *Metals*, 8(10), 10 2018.

[46] Keiro Tokaji, Takeshi Ogawa, and Shuji Osako. THE GROWTH OF MICROSTRUCTURALLY SMALL FATIGUE CRACKS IN A FERRITIC-PEARLITIC STEEL. *Fatigue & Fracture of Engineering Materials & Structures*, 11(5):331–342, 1988.

[47] Akhmad A. Korda, Y. Miyashita, Y. Mutoh, and T. Sadasue. Fatigue crack growth behavior in ferritic-pearlitic steels with networked and distributed pearlite structures. *International Journal of Fatigue*, 29(6):1140–1148, 6 2007.

[48] Y. Mutoh, Akhmad A. Korda, Y. Miyashita, and T. Sadasue. Stress shielding and fatigue crack growth resistance in ferritic-pearlitic steel. *Materials Science and Engineering: A*, 468-470(SPEC. ISS.):114–119, 11 2007.

[49] Kurt Jacobus, R. E. DeVor, and S. G. Kapoor. Machining-Induced Residual Stress: Experimentation and Modeling. *Journal of Manufacturing Science and Engineering*, 122(1):20–31, 2 2000.

[50] Nilesh Varote and Suhas S Joshi. Microstructural Analysis of Machined Surface Integrity in Drilling a Titanium Alloy. *Journal of Materials Engineering and Performance*, 26(9):4391–4401, 2017.

[51] B. M. Gurumurthy, M. C. Gowrishankar, Sathyashankara Sharma, Achutha Kini, Manjunath Shettar, and Pavan Hiremath. Microstructure authentication on mechanical property of medium carbon Low alloy duplex steels. *Journal of Materials Research and Technology*, 9(3):S105–S111, 2020.

[52] George F. Vander Voort. *Metallography, Principles and Practice*, volume 136. 2007.

[53] Ricardo plc. Crankshaft Oil Hole Study. Technical report, 2002.

[54] Bilel Bellakhdhar, Abdelwaheb Dogui, and Jean-louis Ligier. Comptes Rendus Mecanique A simplified coupled crankshaft – engine block model. *Comptes Rendus Mecanique*, 341(11-12):743–754, 2013.

[55] M. Nouari and A. Molinari. Experimental verification of a diffusion tool wear model using a 42CrMo4 steel with an uncoated cemented tungsten carbide at various cutting speeds. *Wear*, 259(7-12):1151–1159, 7 2005.

[56] F.W Taylor. *On the art of cutting metals*. New York, American Society of Mechanical Engineers. The American society of mechanical engineers, New York, 1907.

[57] Mahdi Eynian, Kallol Das, and Anders Wretland. Effect of tool wear on quality in drilling of titanium alloy Ti6Al4V, Part I: Cutting Forces, Burr Formation, Surface Quality and Defects. *High Speed Machining*, 3(1):1–10, 2017.

[58] Peng Li and Zhiyong Chang. Numerical Modeling of the Effect of Cutting-Edge Radius on Cutting Force and Stress Concentration during Machining. *Micromachines*, 13(2), 2 2022.

[59] ASM-International. Chapter 14: Fatigue. *Elements of Metallurgy and Engineering Alloys*, pages 243–264, 2008.

[60] M. Brown, R. M'Saoubi, P. Crawforth, A. Mantle, J. McGourlay, and H. Ghadbeigi. On deformation characterisation of machined surfaces and machining-induced white layers in a milled titanium alloy. *Journal of Materials Processing Technology*, 299(April 2021):117378, 2022.

[61] J M Zhou, V Bushlya, R L Peng, S Johansson, P Avdovic, and J-e Stahl. Effects of Tool Wear on Subsurface Deformation of Nickel- based Superalloy. *Procedia Engineering*, 19:407–413, 2011.

[62] Rengen Ding, Craig Knaggs, Hangyue Li, Yue Gang, and Paul Bowen. Materials Science & Engineering A Characterization of plastic deformation induced by machining in a Ni-based superalloy. *Materials Science & Engineering A*, 778(February):139104, 2020.

[63] ASTM International. Standard Test Method for Microindentation Hardness of Materials. *American Society for Testing and Materials Handbook*, pages 281–293, 2017.

[64] Igor Altenberger, Ravi K. Nalla, Yuji Sano, Lothar Wagner, and Robert O. Ritchie. On the effect of deep-rolling and laser-peening on the stress-controlled low- and high-cycle fatigue behavior of Ti-6Al-4V at elevated temperatures up to 550 °c. *International Journal of Fatigue*, 44:292–302, 11 2012.

[65] Simon Ho, Yung-li Lee, Hong-tae Kang, and Cheng J Wang. Optimization of a crankshaft rolling process for durability. *International Journal of Fatigue*, 31(5):799–808, 2009.

[66] D Biermann, M Heilmann, and M Kirschner. Procedia Engineering Analysis of the Influence of Tool Geometry on Surface Integrity in Single-lip Deep Hole Drilling with Small Diameters. *Procedia Engineering*, 19:16–21, 2012.

[67] A. Fischer, B. Scholtes, and T. Niendorf. Influence of Deep Rolling and Induction Hardening on Microstructure Evolution of Crankshaft Sections made from 38MnSiVS5 and 42CrMo4. *HTM Journal of Heat Treatment and Materials*, 76(3):175–194, 6 2021.

[68] S. R. Thorat and A. G. Thakur. Optimization of Burnishing Parameters by Taguchi Based GRA Method of AA 6061 Aluminum Alloy. *Materials Today: Proceedings*, 5(2):7394–7403, 2018.

[69] A. M. Hassan. An investigation into the surface characteristics of burnished cast Al-Cu alloys. *International Journal of Machine Tools and Manufacture*, 37(6):813–821, 1997.

[70] S Hemanth, A Harish, R Nithin Bharadwaj, and Abhishek B Bhat. ScienceDirect Design of Roller Burnishing Tool and Its Effect on the Surface Integrity of Al 6061. *Materials Today: Proceedings*, 5(5):12848–12854, 2018.

[71] DIN. *EN 10247:2007-07 Micrographic Examination of The Non-Metallic Inclusion Content*. 2007.

[72] K. Kamdani, A. A. Hamsah, N. H. Rafai, M. Z. Rahim, C. K. Wong, and Y. L. Chong. Study of cutting force and surface roughness on drilling stainless steel 316l under various coolant condition. *Key Engineering Materials*, 791(January 2019):116–122, 2018.

[73] Malleswara J Rao N, Chenna A Kesava Reddy, and Rama P Rao V. The effect of roller burnishing on surface hardness and surface roughness on mild steel specimens. *INTERNATIONAL JOURNAL OF APPLIED ENGINEERING RESEARCH, DINDIGUL*, 1(4), 2011.

[74] Trung-Thanh Nguyen. Multi-response performance optimization of burnishing operation for improving hole quality. *Journal of the Brazilian Society of Mechanical Sciences and Engineering*, 43(12):560, 12 2021.

[75] G. Gomez-Gras, J. A. Travieso-Rodriguez, and R. Jerez-Mesa. Experimental Characterization of the Influence of Lateral Pass Width on Results of a Ball Burnishing Operation. In *Procedia Engineering*, volume 132, pages 686–692. Elsevier Ltd, 2015.

[76] J. M. Titchmarsh. Microscopy Techniques for Materials Scientists. *Journal of Microscopy*, 212(2), 2003.

[77] A R Clarke and C N Eberhardt. *Microscopy techniques for materials science*. Woodhead Publishing, 2002.

[78] Mostafa El Laithy, Ling Wang, Terry J. Harvey, Alexander Schwedt, Bernd Vierneusel, and Joachim Mayer. Mechanistic study of dark etching regions in bearing steels due to rolling contact fatigue. *Acta Materialia*, 246:118698, 3 2023.

[79] M. Pradeep Kumar and L. Shakeel Ahmed. Drilling of AISI 304 Stainless Steel under Liquid Nitrogen Cooling: A Comparison with Flood Cooling. *Materials Today: Proceedings*, 4(2):1518–1524, 2017.

[80] M. Kowalik, T. Mazur, and T. Trzepiecinski. Assessment of the Depth of the Deformed Layer in the Roller Burnishing Process. *Strength of Materials*, 50(3):493–503, 5 2018.

[81] Edlira Duka, Heinrich Oettel, and Teuta Dilo. Connection between micro and macro hardness pearlitic-ferritic steel. In *AIP Conference Proceedings*, volume 1476, pages 47–51, 2012.

[82] H. Li, S. Gao, Y. Tian, D. Terada, A. Shibata, and N. Tsuji. Influence of Tempering on Mechanical Properties of Ferrite and Martensite Dual Phase Steel. In *Materials Today: Proceedings*, volume 2, pages S667–S671. Elsevier Ltd, 2015.

[83] Motoki Terano, Fan Zhang, and Masahiko Yoshino. Influence of burnishing condition on static recrystallization of an iron sheet. In *Procedia Engineering*, volume 207, pages 1850–1855. Elsevier Ltd, 2017.

[84] E. N. Borodin, A. A. Gruzdkov, A. E. Mayer, and N. S. Selyutina. Physical nature of strain rate sensitivity of metals and alloys at high strain rates. In *Journal of Physics: Conference Series*, volume 991. Institute of Physics Publishing, 4 2018.

[85] D. Odabas. The Influence of the Temperature on Dry Friction of AISI 3315 Steel Sliding Against AISI 3150 Steel. *IOP Conference Series: Materials Science and Engineering*, 295(1), 2018.

[86] B. D. Cullity and C. D. Graham. *Introduction to Magnetic Materials*. Wiley, 11 2008.

[87] Aphrodite Ktena, Evangelos Hristoforou, Gunther J.L. Gerhardt, Frank P. Missell, Fernando J.G. Landgraf, Daniel L. Rodrigues, and M. Alberteris-Campos. Barkhausen noise as a microstructure characterization tool. *Physica B: Condensed Matter*, 435:109–112, 2 2014.

[88] R. Street and J. C. Woolley. A study of magnetic viscosity. *Proceedings of the Physical Society. Section A*, 62(9), 1949.

[89] Stresstech. "Stresstech Bulletin 2: The properities of Barkhausen noise" https://www.stresstech.com/stresstech-bulletin-2-the-properities-of-barkhausen-noise/ (accessed 15/08/23).

[90] S. Zaefferer, N.-N. Elhami, and P. Konijnenberg. Electron backscatter diffraction (EBSD) techniques for studying phase transformations in steels. In *Phase Transformations in Steels*, pages 557–587. Elsevier, 2012.

[91] P.J. J Withers and H.K.D.H. K D H Bhadeshia. Residual stress. Part 1– Measurement techniques. *Materials Science and Technology*, 17(4):366–375, 2001.

[92] G Farrahi and J L Lebrun. Surface hardness measurement and microstructural characterisation of steel by X-ray diffraction profile analysis. *International Journal of Engineering, Transactions B: Applications*, 8:159–167, 10 1995.

[93] Matthew Brown, David Curtis, Gary McKee, and Pete Crawforth. An evaluation of non-destructive methods for detection of thermally-induced metallurgical machining defects. *Procedia CIRP*, 108(C):7–12, 2022.

[94] M. Vashista and S. Paul. Correlation between full width at half maximum (FWHM) of XRD peak with residual stress on ground surfaces. *Philosophical Magazine*, 92(33), 2012.

[95] S R Claves and A Deal. Orientation Dependence of EBSD Pattern Quality. *Microscopy and Microanalysis*, 11(S02), 8 2005.

[96] Unai Alonso, Naiara Ortega, Jose Antonio Sanchez, Iñigo Pombo, Soraya Plaza, and Borja Izquierdo. In-process prediction of the hardened layer in cylindrical traverse grind-hardening. *International Journal of Advanced Manufacturing Technology*, 71(1-4):101–108, 3 2014.

[97] Jun Liu, John Wilson, Martin Strangwood, Claire L. Davis, Anthony Peyton, and Jonathan Parker. Electromagnetic evaluation of the microstructure of Grade 91 tubes/pipes. *International Journal of Pressure Vessels and Piping*, 132-133:65–71, 8 2015.

[98] Amir Ben Rhouma, N. Sidhom, K. Makhlouf, H. Sidhom, C. Braham, and G. Gonzalez. Effect of machining processes on the residual stress distribution heterogeneities and their consequences on the stress corrosion cracking resistance of AISI 316L SS in chloride medium. *International Journal of Advanced Manufacturing Technology*, 105(1-4):1699–1711, 11 2019.

[99] Sunil Ankalagi, V N Gaitonde, and Praveenkumar Petkar. ScienceDirect Experimental Studies on Hole Quality in Drilling of SA182 Steel. *Materials Today: Proceedings*, 4(10):11201–11209, 2017.

[100] Laurentiu Aurel. Robust Engineering of Deep Drilling Process by Surface State Optimization. *Procedia CIRP*, 8:582–587, 2013.

[101] IACS. IACS UR M53 Rev.4. Technical Report July, 2018.

[102] M. Pietrzyk, J. G. Lenard, and G. M. Dalton. A Study of the Plane Strain Compression Test*. *CIRP Annals - Manufacturing Technology*, 42(1):331–334, 1993.

[103] B Roebuck, J D Lord, M Brooks, M S Loveday, C M Sellars, and R W Evans. Measuring flow stress in hot axisymmetric compression tests. *Measurement Good Practice Guide Number 3*, (3):56, 2002.

[104] A.J. Lacey, M.S. Loveday, G.J. Mahon, B. Roebuck, C.M. Sellars, and M R van der Winden. Measuring flow stress in hot plane strain compression tests. *Measurement Good Practice Guide*, (27):85, 2002.

[105] R. Ramos, N. Ferreira, J. A.M. Ferreira, C. Capela, and A. C. Batista. Improvement in fatigue life of Al 7475-T7351 alloy specimens by applying ultrasonic and microshot peening. *International Journal of Fatigue*, 92:87–95, 2016.

[106] Roberto B. Figueiredo and Terence G. Langdon. Effect of grain size on strength and strain rate sensitivity in metals. *Journal of Materials Science*, 57(8):5210–5229, 2022.

[107] U. Erb, G. Palumbo, and J. L. McCrea. The processing of bulk nanocrystalline metals and alloys by electrodeposition. *Nanostructured Metals and Alloys: Processing, Microstructure, Mechanical Properties and Applications*, pages 118–151, 1 2011.

[108] S. J. Sun, Y. Z. Tian, H. R. Lin, X. G. Dong, Y. H. Wang, Z. J. Wang, and Z. F. Zhang. Temperature dependence of the Hall–Petch relationship in CoCrFeMnNi high-entropy alloy. *Journal of Alloys and Compounds*, 806:992–998, 2019.

[109] L. Q. Guo, M. C. Lin, L. J. Qiao, and Alex A. Volinsky. Ferrite and austenite phase identification in duplex stainless steel using SPM techniques, 2013.

[110] F. Khodabakhshi, M. H. Farshidianfar, A. P. Gerlich, M. Nosko, V. Trembošová, and A. Khajepour. Microstructure, strain-rate sensitivity, work hardening, and fracture behavior of laser additive manufactured austenitic and martensitic stainless steel structures. *Materials Science and Engineering: A*, 756:545–561, 5 2019.

[111] Jian Zhao, Yanru Shi, Sujuan Guo, and Mingliang Zhu. Micromechanical Observation and Numerical Simulation for Local Deformation Evolution of Duplex Stainless Steel. *Materials*, 15(22), 11 2022.

[112] Yong gang Yang, Wang zhong Mu, Xiao qing Li, Hai tao Jiang, Mai Wang, Zhen li Mi, and Xin ping Mao. Effects of strain rate on austenite stability and mechanical properties in a 5Mn steel. *Journal of Iron and Steel Research International*, 29(2):316–326, 2 2022.

[113] Lalit Pun, Guilherme Corrêa Soares, Matti Isakov, and Mikko Hokka. Effects of strain rate on strain-induced martensite nucleation and growth in 301LN metastable austenitic steel. *Materials Science and Engineering: A*, 831, 1 2022.

[114] Rakan Alturk, Steven Mates, Zeren Xu, and Fadi Abu-Farha. Effects of microstructure on the strain rate sensitivity of advanced steels. In *Minerals, Metals and Materials Series*, volume Part F6, pages 243–254. Springer International Publishing, 2017.

[115] R. Hossain, F. Pahlevani, M. Z. Quadir, and V. Sahajwalla. Stability of retained austenite in high carbon steel under compressive stress: an investigation from macro to nano scale. *Scientific Reports*, 6(1):34958, 10 2016.

[116] S. J. Sun, Y. Z. Tian, H. R. Lin, H. J. Yang, X. G. Dong, Y. H. Wang, and Z. F. Zhang. Transition of twinning behavior in CoCrFeMnNi high entropy alloy with grain refinement. *Materials Science and Engineering A*, 712(December 2017):603–607, 2018.

[117] Y.C. Lin, Wen-Yong Dong, Mi Zhou, Dong-Xu Wen, and Dong-Dong Chen. A unified constitutive model based on dislocation density for an Al-Zn-Mg-Cu alloy at time-variant hot deformation conditions. *Materials Science and Engineering: A*, 718:165–172, 3 2018.

[118] Joshua Priest, Hassan Ghadbeigi, Sabino Ayvar-Soberanis, Anders Liljerehn, and Matthew Way. A modified Johnson-Cook constitutive model for improved thermal softening prediction of machining simulations in C45 steel. *Procedia CIRP*, 108:106–111, 2022.

[119] E. S. Puchi-Cabrera, J. D. Guérin, J. G. La Barbera-Sosa, J. C. Álvarez-Hostos, P. Moreau, M. Dubar, and L. Dubar. Friction Correction of Austenite Flow Stress Curves Determined under Axisymmetric Compression Conditions. *Experimental Mechanics*, 60(4):445–458, 4 2020.

[120] Soheil Solhjoo. A note on "barrel Compression Test": A method for evaluation of friction. *Computational Materials Science*, 49(2):435–438, 2010.

[121] S. Klitschke, A. Trondl, F. Huberth, and M. Liewald. Adiabatic heating under various loading situations and strain rates for advanced high-strength steels. In *IOP Conference Series: Materials Science and Engineering*, volume 418. Institute of Physics Publishing, 9 2018.

[122] Qiujia Ma, Yi Shao, Yongchang Liu, Zhiming Gao, and Liming Yu. Martensite-austenite transformation kinetics of high Cr ferritic heat-resistant steel. *International Journal of Materials Research*, 104(10):935–940, 2013.

[123] Y. B. Guo and S. C. Ammula. Real-time acoustic emission monitoring for surface damage in hard machining. *International Journal of Machine Tools and Manufacture*, 45(14):1622–1627, 11 2005.

[124] Mingxin Hao, Bin Sun, and Hao Wang. High-Temperature Oxidation Behavior of Fe–1Cr–0.2Si Steel. *Materials*, 13(3):509, 1 2020.

[125] Vibhor Atreya, Cornelis Bos, and Maria J. Santofimia. Understanding ferrite deformation caused by austenite to martensite transformation in dual phase steels. *Scripta Materialia*, 202:114032, 2021.

[126] Jay K. Raval, Yi Tang Kao, and Bruce L. Tai. Characterizing mist distribution in through-tool minimum quantity lubrication drills. *Journal of Manufacturing Science and Engineering, Transactions of the ASME*, 142(3):1–8, 2020.

[127] Navid Zarif Karimi, Giangiacomo Minak, Parnian Kianfar, and Hossein Heidary. The effect of chisel edge on drilling-induced delamination. 10 2015.

[128] G. I. Kanel. Rate and temperature effects on the flow stress and tensile strength of metals. *AIP Conference Proceedings*, 1426(March):939–944, 2012.

[129] J. Caudill, J. Schoop, and I. S. Jawahir. Correlation of surface integrity with processing parameters and advanced interface cooling/lubrication in burnishing of Ti-6Al-4V alloy. *Advances in Materials and Processing Technologies*, 5(1):53–66, 1 2019.

[130] D. M. Haan, S. A. Batzer, W. W. Olson, and J. W. Sutherland. An experimental study of cutting fluid effects in drilling. *Journal of Materials Processing Technology*, 71(2):305–313, 1997.

[131] Nafiz Yaşar, Mehmet Boy, and Mustafa Günay. The effect of drilling parameters for surface roughness in drilling of AA7075 alloy. *MATEC Web of Conferences*, 112:01018, 7 2017.

[132] Santhanakumar Muthuvel, M. Naresh Babu, and N. Muthukrishnan. Copper nanofluids under minimum quantity lubrication during drilling of AISI 4140 steel. *Australian Journal of Mechanical Engineering*, 18(sup1):S151–S164, 7 2020.

[133] Z. Wang, V. Kovvuri, A. Araujo, M. Bacci, W. N.P. Hung, and S. T.S. Bukkapatnam. Built-up-edge effects on surface deterioration in micromilling processes. *Journal of Manufacturing Processes*, 24, 2016.

[134] Erween Abd Rahim and Hiroyuki Sasahara. Performance of palm oil as MQL fluid during high speed drilling of Ti-6Al-4V. In *Proceedings of the 5th International Conference on Leading Edge Manufacturing in 21st Century, LEM 2009*, 2009.

[135] Alan D. Berman, William A. Ducker, and Jacob N. Israelachvili. Origin and Characterization of Different Stick−Slip Friction Mechanisms. *Langmuir*, 12(19):4559–4563, 1 1996.

[136] P. Pagliaro, M. B. Prime, J. S. Robinson, B. Clausen, H. Swenson, M. Steinzig, and B. Zuccarello. Measuring Inaccessible Residual Stresses Using Multiple Methods and Superposition. *Experimental Mechanics*, 51(7):1123–1134, 2011.